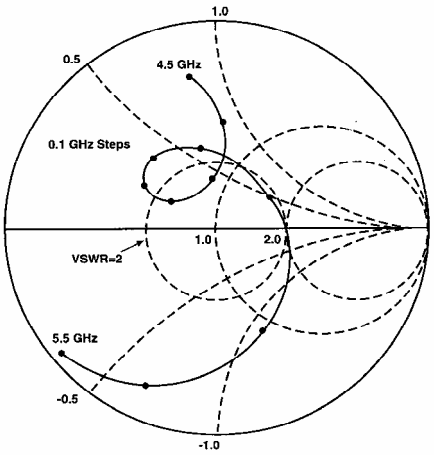

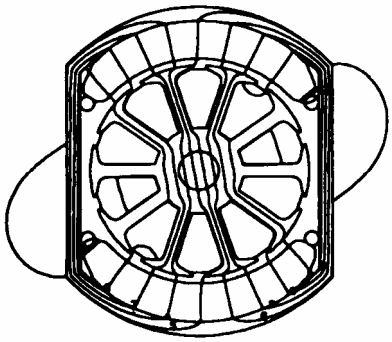

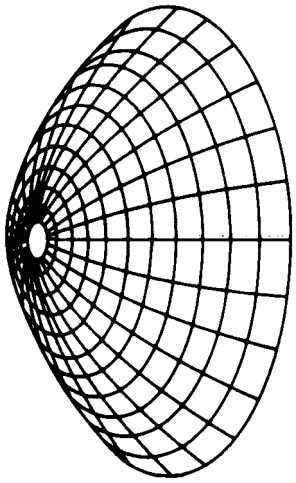

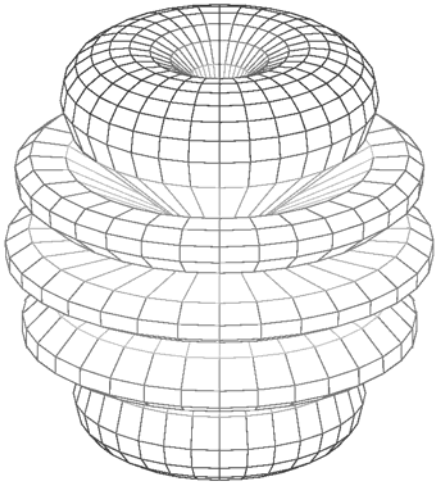

Applied Computational Electromagnetics Society Journal

Editor-in-Chief
Atef Z. Elsherbeni

February 2010
Vol. 25 No. 2
ISSN 1054-4887

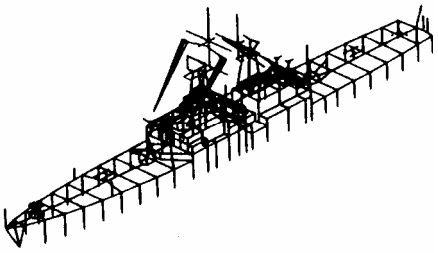

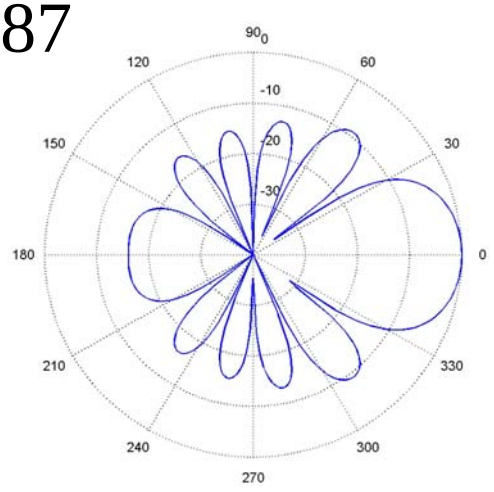

GENERAL PURPOSE AND SCOPE: The Applied Computational Electromagnetics Society ***(ACES)*** Journal hereinafter known as the ***ACES Journal*** is devoted to the exchange of information in computational electromagnetics, to the advancement of the state-of-the art, and the promotion of related technical activities. A primary objective of the information exchange is the elimination of the need to "re-invent the wheel" to solve a previously-solved computational problem in electrical engineering, physics, or related fields of study. The technical activities promoted by this publication include code validation, performance analysis, and input/output standardization; code or technique optimization and error minimization; innovations in solution technique or in data input/output; identification of new applications for electromagnetics modeling codes and techniques; integration of computational electromagnetics techniques with new computer architectures; and correlation of computational parameters with physical mechanisms.

SUBMISSIONS: The ***ACES Journal*** welcomes original, previously unpublished papers, relating to applied computational electromagnetics. Typical papers will represent the computational electromagnetics aspects of research in electrical engineering, physics, or related disciplines. However, papers which represent research in applied computational electromagnetics itself are equally acceptable.

Manuscripts are to be submitted through the upload system of ***ACES*** web site http://aces.ee.olemiss.edu See "Information for Authors" on inside of back cover and at ***ACES*** web site. For additional information contact the Editor-in-Chief:

Dr. Atef Elsherbeni
Department of Electrical Engineering
The University of Mississippi
University, MS 386377 USA
Phone: 662-915-5382 Fax: 662-915-7231
Email: atef@olemis.edu

SUBSCRIPTIONS: All members of the Applied Computational Electromagnetics Society who have paid their subscription fees are entitled to receive the ***ACES Journal*** with a minimum of three issues per calendar year and are entitled to download any published journal article available at http://aces.ee.olemiss.edu.

Back issues, when available, are $15 each. Subscriptions to ***ACES*** is through the web site. Orders for back issues of the ***ACES Journal*** and changes of addresses should be sent directly to ***ACES***:

Dr. Allen W. Glisson
302 Anderson Hall
Dept. of Electrical Engineering
Fax: 662-915-7231
Email: aglisson@olemiss.edu

Allow four week's advance notice for change of address. Claims for missing issues will not be honored because of insufficient notice or address change or loss in mail unless the Executive Officer is notified within 60 days for USA and Canadian subscribers or 90 days for subscribers in other countries, from the last day of the month of publication. For information regarding reprints of individual papers or other materials, see "Information for Authors".

LIABILITY. Neither ***ACES***, nor the ***ACES Journal*** editors, are responsible for any consequence of misinformation or claims, express or implied, in any published material in an ***ACES Journal*** issue. This also applies to advertising, for which only camera-ready copies are accepted. Authors are responsible for information contained in their papers. If any material submitted for publication includes material which has already been published elsewhere, it is the author's responsibility to obtain written permission to reproduce such material.

APPLIED COMPUTATIONAL ELECTROMAGNETICS SOCIETY JOURNAL

February 2010
Vol. 25 No. 2
ISSN 1054-4887

The ACES Journal is abstracted in INSPEC, in Engineering Index, DTIC, Science Citation Index Expanded, the Research Alert, and to Current Contents/Engineering, Computing & Technology.

The first, fourth, and sixth illustrations on the front cover have been obtained from the Department of Electrical Engineering at the University of Mississippi.

The third and fifth illustrations on the front cover have been obtained from Lawrence Livermore National Laboratory.

The second illustration on the front cover has been obtained from FLUX2D software, CEDRAT S.S. France, MAGSOFT Corporation, New York.

THE APPLIED COMPUTATIONAL ELECTROMAGNETICS SOCIETY

JOURNAL

Vol. 25 No. 2 February 2010

TABLE OF CONTENTS

Whispering Gallery Mode Laser in an Elliptical Microring

Reyhan Baktur[1], L. W. Pearson[2], and J. M. Ballato[3]
[1] Department of Electrical and Computer Engineering
Utah State University, Logan, UT 84322, USA
breyhan@engineering.usu.edu

[2]Holcombe Department of Electrical and Computer Engineering
Clemson University, Clemson, SC 29634-0915
PL@exchange.clemson.edu

[3]Center for Optical Materials Science and Engineering Technologies (COMSET)
School of Material Science and Engineering
Clemson University, Clemson, SC 29634-0971
JBALLAT@exchange.clemson.edu

***Abstract*—** Studies on whispering gallery mode (WGM) laser in microrings have been limited to circular geometry. Elliptical microring lasers, despite their potential engineering use, have not been analyzed to guide experiments. This paper introduces a computationally efficient method for determining the WGM laser resonance and the laser field distribution in an elliptical microring. An analytical method is applied to avoid computing high order Mathieu functions. Both WGM resonant frequencies and electromagnetic (EM) field distributions are computed and presented in this paper. Computed results clearly show that the WGM laser field is concentrated on the outer surface of the microring. Results also show that the eccentricity of the ellipse affects the distribution of resonant frequencies and the laser field.

***Index Terms*—** Whispering gallery mode, microring laser, elliptical microring, Mathieu functions.

I. INTRODUCTION

The demonstration of lasers in luminescent conducting polymer thin films [1, 2] has triggered scientists to study lasers achieved with cylindrical microcavities formed with this type of polymer [3-6]. It is reported that a cylindrical microlaser based on whispering gallery mode (WGM) shows the advantages of supporting low-power operation and hence yields a high-Q value [3, 4]. The phenomenon of the whispering gallery was first observed and studied by Lord Rayleigh [7], and the electromagnetic (EM) WGM in a dielectric waveguide was comprehensively analyzed by Wait [8]. Considering the advantage of the low threshold lasing characteristics of microrings as well as the flexibility of forming the conjugate polymer into various geometry [2], there is a potential engineering use of microring lasers as integrated signal sources for communications. Experimental measurements on the lasing spectrum of polymer cylindrical microlasers have been reported [4], and simplified studies for resonant modes were presented by several researchers [5, 6]. Baktur et. al. provided a more comprehensive theoretical description for WGM laser resonances in a circular microring [9].

While microring geometry has been confined to a circular cross-section so far, it is equally important to study the WGM laser in an elliptical microring because such a structure provides a controllable coupling when used as a pump source. It is the objective of this work to develop a computationally efficient method for determining the resonance and fields of a WGM laser in a microring with an elliptical cross-section. The paper is organized as follows. Section II describes the problem solving method and basic formula in an elliptical geometry. Computation, results, and

discussions of WGM resonance and fields are presented in sections III and IV. Limiting factors of the method are concluded in section V.

II. CONFIGURATION OF THE LASER

The configuration of the elliptical microring is as follows. A microring made from an optically active polymer is built on an aluminum or gold core. Both core and ring are of elliptical cross-section (see Fig. 1). The choice of the core material is consistent with the experimental studies [3, 4]. Although waveguide modes exist and can resonate in a microring, to be consistent with experiments [3, 4], we only discuss modes that are detached from the inner boundary of the microring, i.e. WGMs. The microring is modeled to have an infinite length (i.e. infinite in *z*. It should be noted that Fig. 1 is on *xy* plane, and z is vertical to the cross section in *xy* plane.) because the optical length of the microring is in the order of 100 wavelengths and allows us to model the length as infinite for the simplicity of the analysis. The microring can, of course, support propagation in the z direction, bounded by reflections on the annular faces. However, such a mode structure involves radiative loss at these interfaces, and the losses would quench lasing.

The cross-section view of the microring is shown in Fig. 1. Major and minor axes of the inner boundary of the microring are denoted as *a*, *b*. For the outer boundary, the two axes are *a′* and *b′*. The thickness of the microring is *d*, and it is obvious to see that the following relations hold,

$$\begin{aligned} a' &= a + d, \\ b' &= b + d. \end{aligned} \tag{1}$$

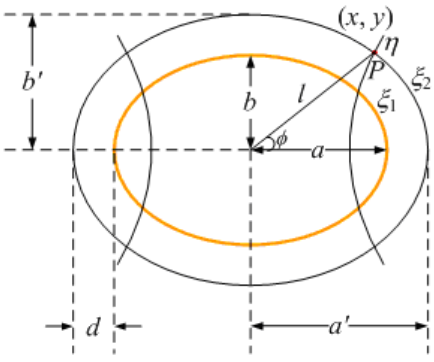

Fig. 1. Cross-section view of the elliptical microring.

In elliptical coordinates, the two-dimensional wave equation can be separated into two Mathieu's equations [11, 12], and solutions of these two equations are combinations of Mathieu's functions [13]. Since WGMs are high order modes [7, 8], it suggests that in order to study the WGM in an elliptical microring, we need to deal with modes involving Mathieu functions of large orders. Although it is possible to study the WGM resonance in an elliptical cavity by evaluating Mathieu functions [14], the mode numbers that can be correctly computed are rather limited. Summations for Mathieu functions of large orders are difficult due to their poor convergence. Additionally, the process of deriving formula for EM field components is very tedious and time consuming. Therefore, we try to provide a much simpler formulation with a smaller computational complexity.

Before computing the WGM resonance and electromagnetic fields, it is helpful to work out relations between variables used in the elliptical coordinate system. In Fig. 1, a point *p* on the outer ellipse can be located by any one pair of variables from (*x*, *y*), (*l*, ϕ) or (ξ_2, η). The relations between these three sets of variables are as follows:

$$\begin{aligned} x &= l\cos\phi, \\ y &= l\sin\phi, \end{aligned} \tag{2}$$

$$\begin{aligned} x &= a'\cos\eta, \\ y &= b'\sin\eta, \end{aligned} \tag{3}$$

$$l = \sqrt{x^2 + y^2}, \tag{4}$$

$$\cos\phi = \pm\frac{a'}{l}\sqrt{\frac{l^2 - b'^2}{a'^2 - b'^2}},$$

$$\begin{aligned} \cos\eta &= \frac{l}{a'}\cos\phi, \\ \sin\eta &= \frac{l}{b'}\sin\phi, \end{aligned} \tag{5}$$

and

$$\tanh\xi_2 = \frac{b'}{a'}. \tag{6}$$

The method proposed to study the WGM laser in an elliptical microring is to deduce the WGM field from the propagation in a local osculating circle [15]. This method has been validated with experiments for WGM in an elliptical microdisk

[15]. At a point in the microring, the laser field is approximated by the field in the circle of curvature at that point.

To begin the discussion, the outer ellipse (axes: *a'*, *b'*) is fit locally with circles of curvature as illustrated in Fig. 2. For example, at the point *P* on the ellipse (axes: *a'*, *b'*), the circle of curvature is C_1. C_1 is an osculating circle at *P*, and it has the same radius as the radius of curvature at the point *P*. The radius of curvature at a point (ξ_2, η), represented by $R(\eta)$, can be computed from the following formula [16]:

$$R(\eta) = \frac{(a'^2 \sin^2\eta + b'^2 \cos^2\eta)^{\frac{3}{2}}}{a'b'}. \qquad (7)$$

The WGM field at P_1 in the ellipse is viewed as having the same property as the WGM field at P_1 in the circle C_1. Therefore, computing the field at P_1 in C_1 approximates the field in the ellipse at P_1. Similarly, fields at P_2 and P_3 can be obtained by computing fields in the circle C_2 and C_3 at these points. When circles of curvature are fit into the ellipse at every point, the field at any point inside the ellipse (i.g. P_1 and P_3 Fig. 2) and outside the ellipse (i.g. P_2 in Fig. 2) can be accordingly computed.

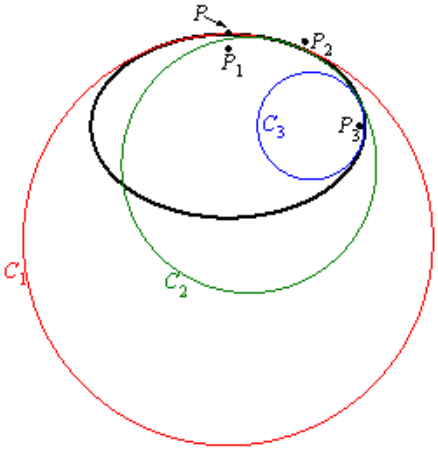

Fig. 2. Ellipse with its osculating circles at three points.

III. WHISPERING GALLERY MODE RESONANCE

A. Analysis

When computing the resonance, the EM fields are separated into transverse electric (TE) and transverse magnetic (TM) modes to *z* axis, which is along the length of the microring. The two types of modes are then treated individually. In the local circle (i.e. the circle of curvature), the circumferential propagation is contained in $e^{-jv\phi}$, where *v* is the angular wave number [9], and ϕ is the angular distance on the local circle. It is desirable to rewrite $e^{-jv\phi}$ into $e^{-jv(\eta)\phi(\eta)}$ to show local propagation. When a WGM propagates along the ellipse, for a whole period, the increase in phase along the path of the angular propagation is $\int_{\eta=0}^{\eta=2\pi} v(\eta)\phi(\eta)d\eta$. In order to achieve a WGM resonance the phase increase needs to be an integer multiple of 2π when the EM wave finishes an entire period along the ellipse. Accordingly we have equation (8), where *m* is an integer and $v(\eta)$, which is closely related to the radius of the curvature [9], is the order of the Bessel functions that describe the WGM in the local microring at η.

$$\int_{\eta=0}^{\eta=2\pi} v(\eta)\phi(\eta)d\eta = 2m\pi. \qquad (8)$$

In equation (8), $\phi(\eta)$ is the angular distance along the local circle at η and the corresponding length on the local circle is

$$l(\eta) = R(\eta)\phi(\eta). \qquad (9)$$

It should be noted that at the vicinity of (ξ, η), $l(\eta)$ can be approximated by the arc-length of the ellipse along $d\eta$ and it yields

$$l(\eta) = \sqrt{a'^2 \sin^2\eta + b'^2 \cos^2\eta}\, d\eta. \qquad (10)$$

Using (7), (9) and (10), (8) can be re-written into

$$\int_0^{2\pi} \frac{a'b'}{a'^2 \sin^2\eta + b'^2 \cos^2\eta} v(\eta)d\eta = 2m\pi. \qquad (11)$$

When the ellipse takes the limit to a circle, (11) gives $v=m$. This result is the same as discussed in [9] for a circular microring resonance. By using a zero finding routine, $v(\eta)$ can be computed from the characteristic equation of the local microring.

B. Computed Results

Resonant frequencies (wavelengths) for both TM and TE WGM modes in elliptical microrings are computed and the results are plotted in Fig. 3. The elliptical microrings have the same perimeters and have varied axial ratios. In computation, the integration in equation (11) is divided into 80 sub-intervals, and the Gaussian quadrature with the

order of 32 is used over sub-intervals. From Fig. 3, it is seen that the axial ratio of the ellipse affects the resonance by shifting the resonant wavelengths. But the shifting is not significant when the laser resonance (630 *nm*) is considered. Also, the spacing between the wavelengths does not change significantly according to the shape of the ellipse as long as the perimeter of the ellipse stays the same.

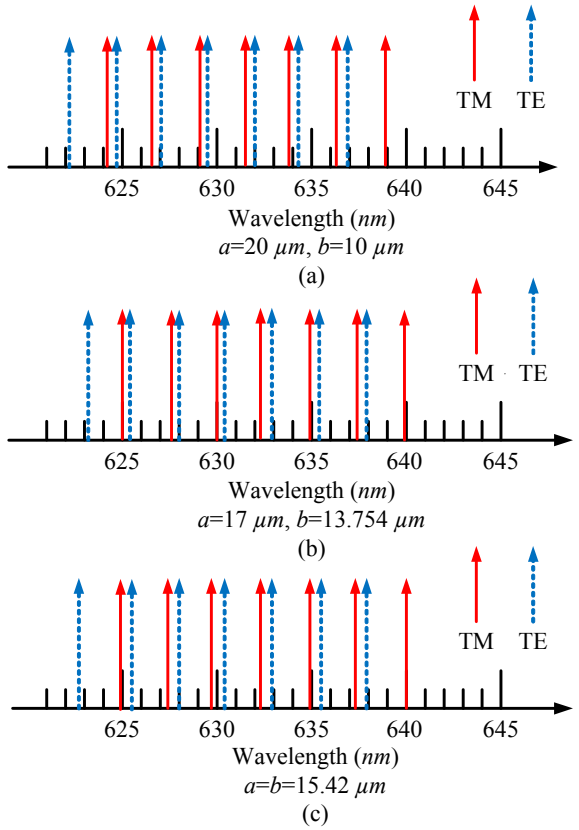

Fig. 3. WGM resonance in an elliptical microring with respect to the axial ratio.

C. Discussion

It is useful to have a simplified formula to approximately determine the resonant wavelengths to guide experiments. Suppose at λ_0 there is a WGM resonance, then equation (8) holds for λ_0, and it means the equation (12) shown below is true. The refractive index of the microring is n_r.

$$\frac{2\pi n_r}{\lambda_0}\int_0^{2\pi}\frac{\lambda_0}{2\pi n_r}\frac{ab}{a^2\sin^2\eta+b^2\cos^2\eta}\nu(\eta)d\eta = 2\pi m\,. \tag{12}$$

If we let $L = \int_0^{2\pi}\frac{\lambda_0}{2\pi n_r}\frac{ab}{a^2\sin^2\eta+b^2\cos^2\eta}\nu(\eta)d\eta$,

Since $\nu(\eta)$ is related to $R(\eta)$ [8], $\nu(\eta)$ can be rewritten as

$$\nu(\eta) = \frac{2\pi}{\lambda_0}n_r\alpha(\eta)R(\eta), \tag{13}$$

where $\alpha(\eta)$ is a coefficient. So L becomes

$$\begin{aligned} L &= \int_0^{2\pi}\alpha(\eta)\frac{ab}{a^2\sin^2\eta+b^2\cos^2\eta}R(\eta)d\eta \\ &= \int_0^{2\pi}\alpha(\eta)\sqrt{a^2\sin^2\eta+b^2\cos^2\eta}\,d\eta\,. \end{aligned} \tag{14}$$

Therefore, from (12), we have

$$L(n_r\ /\ \lambda_0) = m\,. \tag{15}$$

Suppose that a new resonance occurs at $\lambda_0+\Delta\lambda$ and results in an integer m-1 for (15). L varies slowly compared to $\Delta\lambda$, and one can assume that L does not change with respect to the wavelength. Therefore, we have

$$\frac{n_r}{\lambda_0+\Delta\lambda}L \approx m-1. \tag{16}$$

From (16), $\Delta\lambda$ can be computed as the following

$$\Delta\lambda \approx \frac{\lambda_0^{\,2}}{n_r\int_0^{2\pi}\alpha(\eta)\sqrt{a^2\sin^2\eta+b^2\cos^2\eta}\,d\eta}\,. \tag{17}$$

If we further assume $\alpha(\eta)\approx 1$, then $\Delta\lambda$ can be approximately computed from

$$\Delta\lambda \approx \frac{\lambda_0^{\,2}}{n_r\int_0^{2\pi}\sqrt{a^2\sin^2\eta+b^2\cos^2\eta}\,d\eta}\,. \tag{18}$$

Equation (18) is easy to compute and it gives a simple approximate check for experimental data, but it is an approximation because α approaches 1 only when the structure is electrically large. For example, it is found that α increased from 0.94 to 0.97 as the radius of curvature increased from 10.0 to 23.0 μm for the free space wavelength of 632.00 *nm*.

IV. COMPUTATION OF THE WGM FIELD

A. Analysis

When an excitation is placed near P_0 in the osculating circle C_0 (Fig. 4), the WGM field at P_0 can be determined from the radius of C_0 and v_0, which is the order of the WGM. The EM field at P_1, which is located next to P_0, is on the osculating

circle C_1. When P_0 and P_1 are in the vicinity of each other, both of them can be approximately viewed as in the circle C_1, and accordingly satisfy the following:

$$F(P_1) = F(P_0)e^{j\nu_1\Delta\phi}. \quad (19)$$

The exponent in (19) can be re-written to have

$$j\nu_1\Delta\phi = j\frac{\nu_1}{R_1}R_1\Delta\phi = j\frac{\nu_1}{R_1}\Delta l. \quad (20)$$

The arc-length can be computed from

$$\Delta l = \sqrt{a^2\sin^2\eta_1 + b^2\cos^2\eta_1}\,\Delta\eta, \quad (21)$$

where $\Delta\eta$ is the angular variation from P_0 to P_1 along the ellipse e, η_1 is the angular coordinate of P_1 on the ellipse e and the relation between η and ϕ is given by equation (5) .

By using (21), (20) becomes

$$j\nu_1\Delta\phi = j\frac{ab\nu_1}{a^2\sin^2\eta_1 + b^2\cos^2\eta_1}\Delta\eta. \quad (22)$$

Let $\Gamma_1 = \dfrac{ab\nu_1}{a^2\sin^2\eta_1 + b^2\cos^2\eta_1}$, and the equation (19) becomes

$$F(P_1) = F(P_0)e^{j\Gamma_1\Delta\eta}. \quad (23)$$

Similarly, fields at P_2 and P_3 can be computed from

$$F(\mathrm{P}_2) = F(P_1)e^{j\Gamma_2\Delta\eta} = F(P_0)e^{j\Gamma_1\Delta\eta}e^{j\Gamma_2\Delta\eta} = F(P_0)e^{j(\Gamma_1+\Gamma_2)\Delta\eta}, \quad (24)$$

and

$$F(P_3) = F(P_0)e^{j(\Gamma_1+\Gamma_2+\Gamma_3)\Delta\eta}. \quad (25)$$

Iterating this process gives the field at P_N to be

$$F(\eta) = F(P_0)\exp(j\sum_{i=1}^{N}\Gamma_i\Delta\eta). \quad (26)$$

When N approaches infinity, (26) becomes

$$F(\eta) = F(P_0)\exp[j\int_{\eta_0}^{\eta}\Gamma(\eta)d\eta]. \quad (27)$$

In order to have (27) valid for every η, a definition for Γ at η_0 is added to have

$$\Gamma(\eta) = \begin{cases} 0, & \eta = \eta_0 \\ \dfrac{ab\nu(\eta)}{a^2\sin^2\eta + b^2\cos^2\eta}, & \text{otherwise}. \end{cases} \quad (28)$$

So, to compute a WGM field component at a general point P_η^r, we find the projection of P_η^r on the ellipse e, and denote the projection as (ξ_0, η). The distance from P_η^r to the ellipse is d_r. Then, on the ellipse with two axes $(a+d_r, b+d_r)$, we locate a point P_0^r that can also be defined by the osculating circle C_0 and the distance d_r. For example, in Fig. 4, P_0^r is at $(R_0+d, \pi/2)$, R_0 is the radius of C_0. The electromagnetic field at P_0^r can be computed from WGM field in a circular resonator as described in [17], and the EM field at P_η^r can be determined from

$$F(\mathrm{P}_\eta^r) = F(\mathrm{P}_0^r)\exp[j\int_{\eta_0}^{\eta}\Gamma(\eta)d\eta]. \quad (29)$$

It is important to make sure the correct η is used. In (29), η is associated with the outer ellipses e, and it can be determined from (3) or (5).

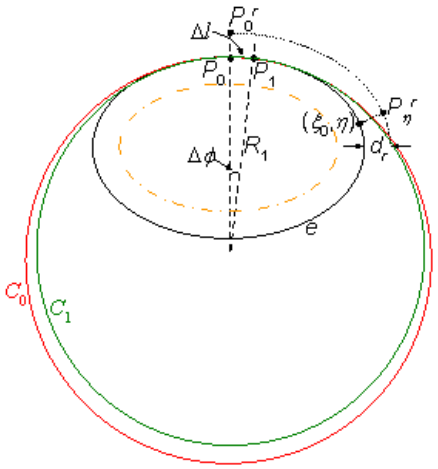

Fig. 4. Illustration of the elliptical microring with osculating circles.

B. Computational Considerations

The EM WGM field is studied by computing six field components (E_z, E_ρ, E_ϕ and H_z, H_ρ, H_ϕ). The z components are along length of the microring, and the other two components are along the radial and azimuthal axes of the elliptical cross section. To use the relation in (29) to compute EM field at the point P_η^r, the distance from this point to the outer ellipse and η is needed. It is simpler if the problem is discussed in the rectangular coordinate system. Suppose P_η^r is at (x, y), and we need to find its projection (ξ_0, η), which can be also located by (x_p, y_p). The distance between P_η^r and (ξ_0, η) satisfies

$$d_r(x_p, y_p)^2 = (x_p - x)^2 + (y_p - y)^2. \quad (30)$$

The projection of P_η^r is on the outer ellipse, so it satisfies

$$x_p^2 / a^2 + y_p^2 / b^2 = 1. \quad (31)$$

By making use of equation (31), d_r^2 can be converted to a function of only x_p or y_p. In order for (x_p, y_p) to be the projection of P_η^r, d_r^2 has to be the minimum value. So by searching for the zero around (x, y) of the $d(d_r^2)/dx_p$ or $d(d_r^2)/dy_p$, x_p and y_p can be located and η can then be found from either $\cos\eta = x_p / a$ or $\sin\eta = y_p / b$.

C. Computed Results

A WGM field excited by an infinite electric line source along the length of a microring is computed. The perimeter of the microring is fixed at 36π μm, and the axial ratio is varied from 1 to 2:1. The thickness of the microring is 4 μm. The source is located inside the microring on $\eta=\pi/2$, and it is 4.0 μm away from the outer boundary of the microring. The operation wavelength is chosen to be at λ=630.0 nm in free space. Magnitudes of the E_z component (i.e. $|E_z| = \sqrt{\mathrm{Re}(E_z)^2 + \mathrm{Im}(E_z)^2}$) in a microring with an axial ratio 1:1.5 is plotted in Fig. 5.

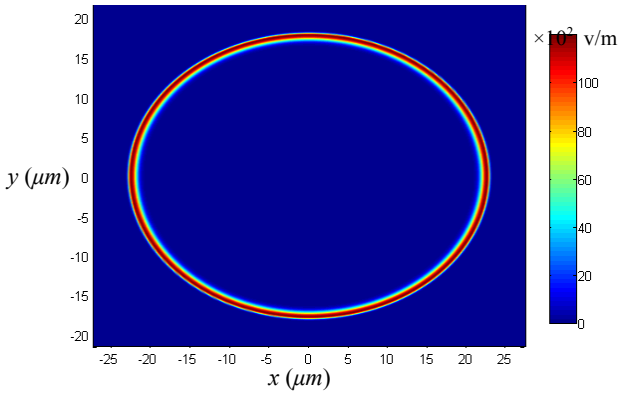

Fig. 5. Magnitude of E_z (v/m) when a:b=1.5.

It is clearly seen that the electromagnetic field concentrates at the outer boundary of the microring. From the figure the field decayed to 0 within less than 2.0 μm from the outer boundary, and the thickness of the ring is 4 μm. In order to see details of the WGM field, the real and imaginary parts of E_z are plotted along different ϕ as shown in Fig. 6- Fig. 8. Note that when $\phi=\pi/2$, it is the same ϕ plane where the source lies.

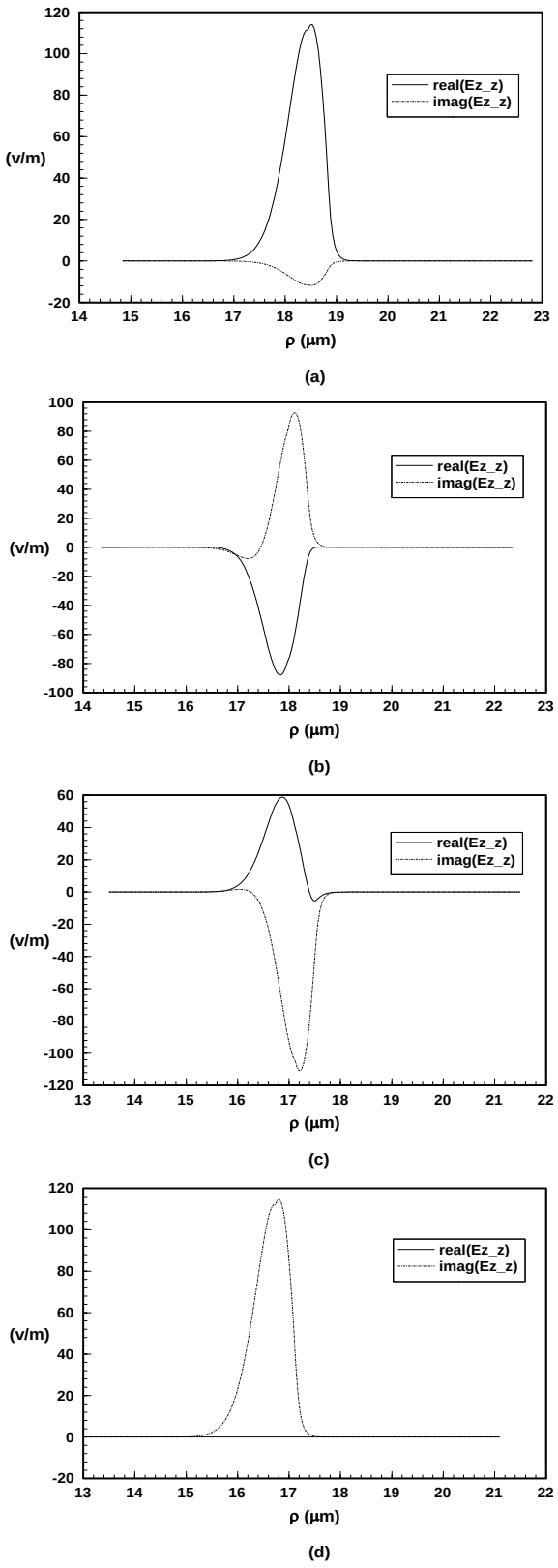

Fig. 6. Real and imaginary parts of E_z for a:b=1.1, ϕ=0, π/6, π/3 and π/2 respectively in (a) to (d).

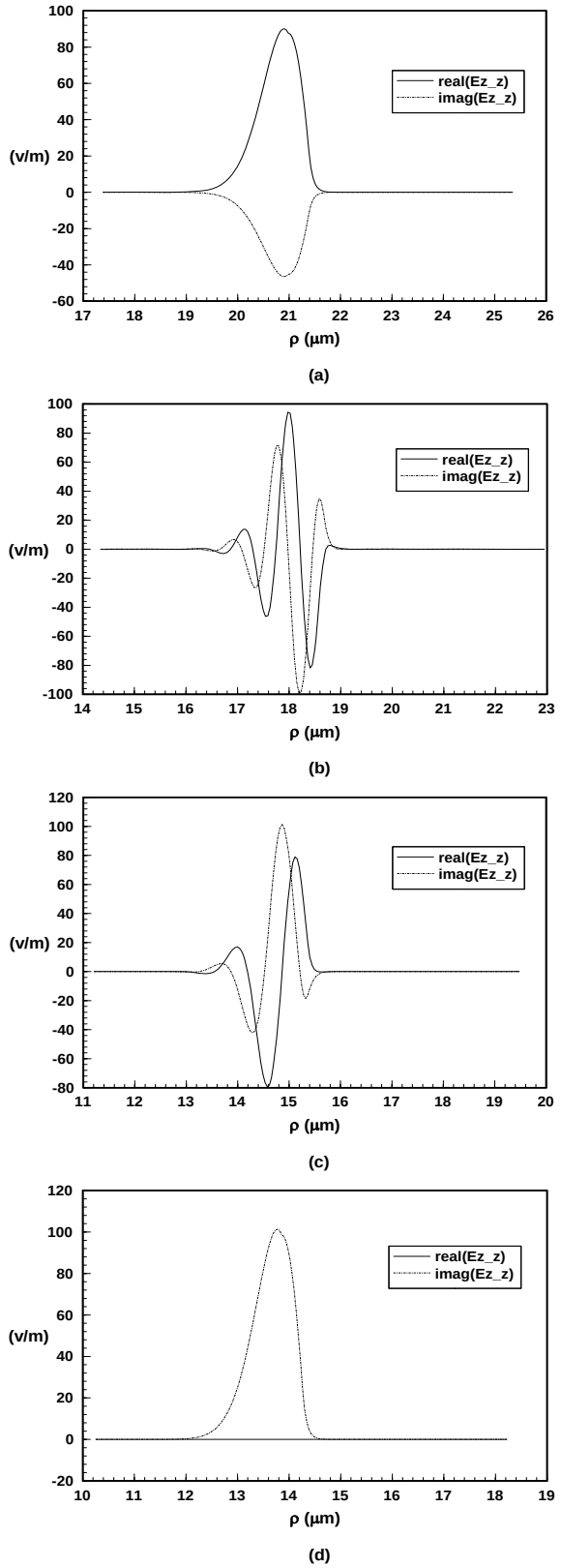

Fig. 7. Real and imaginary parts of E_z for a:b=1.5, ϕ=0, π/6, π/3 and π/2 respectively in (a) to (d).

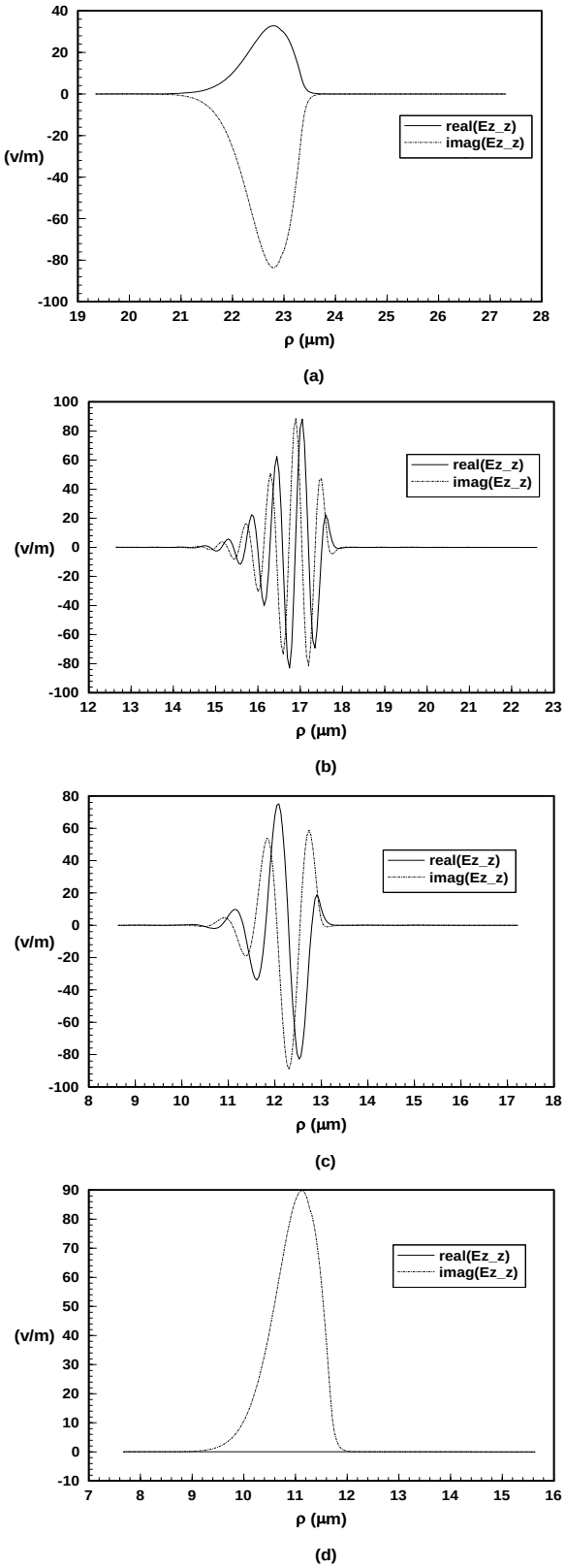

Fig. 8. Real and imaginary parts of E_z for a:b=2, ϕ=0, π/6, π/3 and π/2 respectively in (a) to (d).

D. Discussion

From section III, it is seen that the eccentricity of the ellipse affects the resonance by shifting the resonant frequency. Therefore when the axial ratio of the microring is changed, the excitation frequency needs to be shifted simultaneously to achieve a resonance. Otherwise, if the frequency is fixed to resonate for the circular microring, then as the microring becomes more eccentric, the excitation frequency is further away from the resonance, and it results in the decreased intensity of the EM field.

From Fig. 6 to Fig. 8, especially (c) and (d) of these figures, the phase of E_z changes along the constant ϕ line. This change can be understood with the illustration shown in Fig. 9, where the field at point P_1 has same phase as fields at points on l. P_s is the source point. Fields at these points are computed from WGM in the osculating circle of the outer ellipse at P_2'. The data are plotted along a constant ϕ while P_1 and P_2 are not both on the line l, and they are not computed from the same osculating circle. Therefore, P_1 and P_2 do not have the same phase unless when $\phi=k\pi$ or $\phi=k\pi+\pi/2$, where k is an integer.

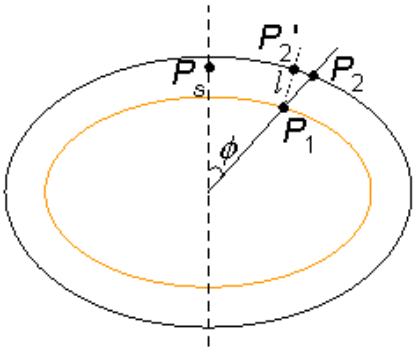

Fig. 9. Illustration of the phase plane of the WGM field in the elliptical microring.

V. CONCLUSION

For an elliptical microring, both WGM resonance and field components are computed by fitting the ellipse with circle of curvature. In computations, the assumption is made such that the WGM field at a point in the elliptical microring is the same as the WGM field in the circle of the curvature of the ellipse at that point. This assumption is valid for an electrically large elliptical microring where the electric radius of the microring is of the order of 100.

It is found that a change in the axial ratio of the elliptical microring results in a shift in the WGM resonant frequencies. Because the eccentricity shifts the resonance, when using the same excitation where a circular microring reaches its resonance, and then deforming the circular ring into an elliptical ring, it gives decreased magnitude of the laser field.

The method applied is valid for electrically large structures and therefore for the case of a highly eccentric ellipse. At the ends of the major axis, the circle of curvature may have a small radius, which may not support a WGM, and the method discussed will no longer be valid for such geometry.

One needs to pay attention to the thickness of the microring. As discussed in [9], the thickness of the ring to support the WGM is associated with the dimension of the structure. The bigger the radius of the microring, the thicker the microring must be. This means that for an elliptical microring, it has to be thick enough to support WGM at two ends of the minor axis (For example, P_0 in Fig. 4) because the osculating circle has the largest radius at this point. On the other hand, when a relatively thick circular microring is deformed into an elliptical microring, there may be a sharp edge at the major axis at the inner boundary and it may affect the computation and validity of the method presented.

REFERENCES

[1] N. Tessler, G. J. Denton and R. H. Friend, "Lasing of Conjugated Polymer Microcavities", *Nature*, vol. 382, pp. 695-697, 1996.

[2] C. Kallinger, *et. al*., "A Flexible Conjugated Polymer Laser", *Adv. Mater*., vol. 10, no.12, pp. 920-923, 1998.

[3] S. V. Frolov, A. Fujii, D. Chinn, Z. V. Vardeny, K. Yoshino, and R. V. Gregory, "Cylindrical Microlasers and Light-emitting Devices from Conducting Polymers", *Appl. Phys. Lett.*, vol. 72, no. 2, pp. 2811-2813, 1998.

[4] S. V. Frolov, M. Shkunov, A. Fujii, K. Yoshino, and Z. V. Vardeney, "Lasing and Stimulated Emission in π–Conjugated Polymers", *IEEE J. Quantum Elect*., vol. 36, no. 1, pp. 2-11, 2000.

[5] R. C. Polson, G. Levina, and Z. V. Vardeny, "Mode Characterization of Microring Polymer Laser", *Synthetic Metals*, vol. 111, pp. 363-367, 2001.
[6] N. C. Frateschi and A. F. J. Levi, "Resonant Modes and Laser Spectrum of Microdisk Lasers", *Appl. Phys. Lett*., vol. 66, no. 2, pp. 2932-2934, 1995.
[7] J. W. Strutt, "The Problem of the Whispering Gallery", *Philosophical Magazine*, vol. xx, pp. 1001-1004, 1910.
[8] J. R. Wait, "Electromagnetic Whispering Gallery Modes in a Dielectric Rod", *Radio Science*, vol. 2, no. 9, pp. 1005-1017, 1967.
[9] R. Baktur, L. W. Pearson and J. M. Ballato, "Theoretical Determination of Lasing Resonances in a Microring", *J. of Appl. Phys*., vol. 101, no. 4, pp. 043102-043102, 2007.
[10] M. Abramowitz and I. A. Stegun, *Handbook of Mathematical Functions with Formulas, Graphs, and Mathematical Tables*, John Wiley & Sons, 1972.
[11] C. Yeh, "Elliptical Dielectric Waveguides", *J. Appl. Phys*., vol. 33, no.11, pp. 3235-3243, 1962.
[12] L. A. Lyubimov, G. I. Veselov, and N. A. Bei, "Dielectric Waveguides with Elliptical Cross Section", *Radio Eng. Electron*. (USSR), vol. 6, pp. 1668-1677, 1961.
[13] N. W. McLachlan, *Theory and Application of Mathieu Functions*. Oxford, England: University Press, 1951.
[14] M. Matsubara, Y. Tomabechi, and K. Matsumura, "An Analysis for Resonance Characteristics of Whispering Gallery Modes on an Elliptic Dielectric Disk", *Proceedings of APMC, Taipei Taiwan,* pp. 473-475, 2001.
[15] Y. Kogami, Y. Tomabechi, and K. Matsumura, "Resonance Characteristics of Whispering-Gallery Modes in an Elliptic Dielectric Disk Resonator", *IEEE Tran. Microw. Theory Tech.*, vol. 44, no. 3, pp. 473-475, 1996.
[16] C. E. Pearson, *Handbook of Applied Mathematics*, Van Nostrand Reinhold Company, 1974.
[17] R. Baktur, L. W. Pearson, and J. M. Ballato, "Computation of Electromagnetic Whispering Gallery Mode Field in a Dielectric Microring Fabricated on a Metal Wire", *Electromagnetics*, vol. 29, no.1, pp. 1-12 , 2009.

Reyhan Baktur graduated from Clemson University in 2005 with a doctoral degree in electrical engineering, where she studied the whispering gallery mode laser in polymer microrings. She is currently an Assistant Professor of Electrical and Computer Engineering at Utah State University. Dr. Baktur is a member of IEEE.

L. Wilson Pearson is a Samuel R. Rhodes Professor of Electrical and Computer Engineering at Clemson University. His research interests include antennas, RF systems, and software-defined radio. Application areas include communications, spatial power combining, and low-cost phased-array antennas. Professor Pearson is an IEEE fellow and has served as Editor-in-Chief for the IEEE Transactions on Antennas and Propagation and on the Editorial Board of the IEEE Proceedings. He currently is Chair of USNC-URSI Commission D. He is a recipient of an IEEE Third Millennium Medal, the Provost's Award for Scholarly Excellence (Clemson University), and the McQueen Quattlebaum Faculty Achievement Award.

John Ballato is a Professor of Materials Science and Engineering at Clemson University where he also serves as Director of the Center for Optical Materials Science and Engineering Technologies (COMSET). He received his B.S. and Ph.D. degrees in Ceramic and Materials Science and Engineering from Rutgers. He has published over 160 archival papers with over 1500 citations, holds 25 US and foreign patents, and has given over 120 invited lectures and colloquia.

A Green's Function Approach to Calculate Scattering Width for Cylindrical Cloaks

Jeffrey S. McGuirk[1], Peter J. Collins[1], Michael J. Havrilla[1], and Aihua W. Wood[2]

[1]Department of Electrical and Computer Engineering
Air Force Institute of Technology, Wright-Patterson AFB, OH 45433-7765, USA
jeffrey.mcguirk@afit.edu, peter.collins@afit.edu, michael.havrilla@afit.edu

[2]Department of Mathematics and Statistics
Air Force Institute of Technology, Wright-Patterson AFB, OH 45433-7765, USA
aihua.wood@afit.edu

***Abstract*—**The anisotropic material properties of cylindrical cloaks can be simulated using thin, concentric layers of homogeneous, isotropic material. A Green's function for a line current in the presence of a layered PEC cylinder can be used to calculate the scattering width from a cloaked PEC cylinder with a significant improvement in computational efficiency compared to solutions obtained using the finite element method.

***Index Terms*—**Electromagnetic cloaks, Finite Element Method (FEM), COMSOL Multiphysics Package, Green's functions.

I. INTRODUCTION

In 2006, Pendry *et al.* published results demonstrating it is theoretically possible to perfectly cloak an object thereby making it invisible to incident electromagnetic radiation [1]. Since the publication of this work, there has been a significant effort to show ideal cloaks result in a region of space into which no electromagnetic energy penetrates while preventing perturbation to the incident electromagnetic field outside of the cloaking mechanism [2]–[5].

In this paper, we will focus entirely on two-dimensional cylindrical cloaks. The material parameters for a cylindrical cloak can be determined using the coordinate transformation technique in [6] and are shown in equations (1) and (2). Note *a* and *b* are the inner and outer radial boundaries of the cloak. The material described by equations (1) and (2) is anisotropic and spatially varying. Manufacture of such a material would require detailed control of the six constitutive parameters which is quite difficult. In order to increase the manufacturability of a cylindrical cloak, the incident field can be decomposed into either transverse electric (TE) waves, in which the magnetic field is solely *z*-directed, or transverse magnetic (TM) waves, in which the electric field is solely *z*-directed. The decomposition is performed to reduce the number of constitutive parameters that require specificity from six to three. As an example, for a TE field incident on a cylindrical cloak, only the μ_z, ε_ρ, and ε_θ components of the constitutive parameter tensors impact the scattered field's behavior.

$$\mu_\rho = \frac{\rho - a}{\rho},\ \mu_\theta = \frac{\rho}{\rho - a},\ \mu_z = \frac{\rho - a}{\rho}\left(\frac{b}{b-a}\right)^2 \quad (1)$$

$$\varepsilon_\rho = \frac{\rho - a}{\rho},\ \varepsilon_\theta = \frac{\rho}{\rho - a},\ \varepsilon_z = \frac{\rho - a}{\rho}\left(\frac{b}{b-a}\right)^2 \quad (2)$$

In addition to field decomposition, simplified material parameter sets have been developed in order to increase manufacturability [7]–[10]. Note at $\rho = a$, ideal values for μ_θ and ε_θ are infinite. Simplified parameter sets typically eliminate the requirement for these infinite values. The penalty for this simplification is a reduction in cloaking effectiveness. However, these simplified cloaks do inherit many of the ideal cloak's energy bending properties.

There have been numerous simulations of cloaking geometries. The majority use the COMSOL Multiphysics package [11]–[16], a commer-

cially available finite-element-method (FEM) based package capable of handling cloaks' anisotropic, inhomogeneous constitutive parameters. There have also been cloak simulations using the finite difference time domain method [17]–[19]. Simulation results confirm cloaks behave as theoretically predicted.

In this paper, we first present background theory on analytic solutions for the scattering width of a PEC cylinder, and then compare the results to those obtained using the COMSOL Multiphysics software. We then discuss a method to approximate cloak parameters using layered homogenous isotropic materials. This leads to the development of a Green's function which can be used to determine the scattering width of a cloaked PEC cylinder. The Green's function solution is shown to be significantly faster and less computationally intensive than the FEM-based solution.

II. BACKGROUND THEORY

In this section, we present basic results for the scattering width of a PEC cylinder using theoretical methods and the COMSOL Multiphysics software. We also discuss the method proposed in [20] that uses isotropic materials to simulate anisotropic cloaking media. This is the basis for our Green's function implementation proposed in Section III.

A. Scattering Width of a PEC Cylinder

The two-dimensional scattering width, σ_{2D}, of a PEC cylinder for an incident TE plane wave propagating in free space is known to be [21]

$$\sigma_{2D} = \frac{2\lambda}{\pi}\left|\sum_{m=0}^{\infty}\varepsilon_m \frac{J_m^{'}(k_o a)}{H_m^{'(2)}(k_o a)}\cos(m\theta)\right|^2, \quad (3)$$

where k_o is the free space wave number, θ is the observation angle, a is the radius of the cylinder, and ε_m is 1 for $m = 0$ and 2 otherwise. Note that ' implies differentiation with respect to ρ. Equation (3) can be truncated based on the specified level of accuracy. In this paper, the summations in equation (3) and in equation (12) are truncated to $m = M$ such that

$$\begin{aligned} &x = \max\left|F_m\right|,\ m \in [0, M], \\ &\forall\ m > M,\ \left|F_m\right| < 0.01x, \end{aligned} \quad (4)$$

where $$F_m = \frac{J_m^{'}(k_o a)}{H_m^{'(2)}(k_o a)}, \qquad F_m = B_m^{n+1},$$

in equation (3) and in equation (19) respectively. The validity of truncating using equation (4) can be verified by comparing the calculated scattering widths of a PEC cylinder of radius $a = \lambda$ for $m = 10$ and $m = 50$. The metric we used to compare the similarity between the solutions is the average difference in σ_{2D}. Mathematically, this is

$$\Delta = \frac{1}{M}\sum_{m=1}^{M}\left|\sigma_{2D}^{A} - \sigma_{2D}^{B}\right|, \quad (5)$$

where M is the total number of observation angles, and the σ_{2D}-terms are the scattering widths we wish to compare. Δ for $\sigma_{2D}|_{m=10}$ compared to $\sigma_{2D}|_{m=50}$ is 0.0063 m^2, which is negligible since σ_{2D} is on the order of 10 m^2 for the measurement set.

Unfortunately, most objects of interest for which scattering width data is desired do not have nice analytic solutions such as equation (3). Other computational methods can be used for such calculations. FEM is a useful approach, particularly in the field of cloaks due to the spatial dependence of the constitutive parameters. However, the computational burden of the finite element method can be significant.

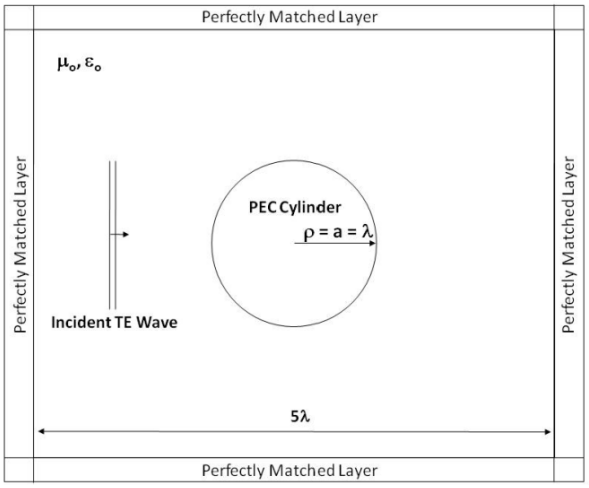

Fig. 1. Geometry for an FEM simulation of scattering from a PEC cylinder.

As an example, consider the geometry shown in Fig. 1. We wish to solve for the PEC cylinder's scattering width due to illumination by an incident TE plane wave. We can use the theoretical solution in equation (3) and compare with the FEM solution obtained using the COMSOL software. Note the computational boundary is only 5λ×5λ.

Therefore, Huygen's principle is used within the COMSOL software to transform the near field results to the far zone, from which scattering width data can be obtained.

Different uniform meshes were used in the COMSOL simulations, where a smaller maximum element length (MEL) corresponds to a finer, denser mesh. We simulated the geometry shown in Fig. 1 using seven different values of MEL and compared the results to the theoretical solution where m = 10. Results are shown in Table 1 with additional information on problem size and solution speed.

Table 1: Analytic and FEM Solution Comparison.

MEL	Unknowns	Time	$\Delta\sigma_{2D}\|_{m=10}$
0.5λ	2,056	0.17 s	0.171 m^2
0.25λ	3,832	0.23 s	0.125 m^2
0.1λ	23,146	1.04 s	0.039 m^2
0.075λ	40,654	1.67 s	0.039 m^2
0.05λ	92,168	4.02 s	0.041 m^2
0.025λ	366,024	16.5 s	0.043 m^2
0.01λ	2,292,872	1,493 s	0.043 m^2
m = 10	N/A	0.14 s	N/A
m = 50	N/A	0.25 s	0.006 m^2

Obviously there is good agreement between the analytic and FEM solutions. However, we needed a metric to define FEM solution accuracy. Therefore, based on the results in Table 1, we used a Δ on the order of 0.1 m^2 to be the threshold to define good agreement between the solutions. For the geometry in Fig. 1, an MEL of 0.1λ is sufficient to obtain good solution agreement. However, as will be seen shortly, there are cloak geometries where finer mesh densities are required due to the thinness of subdomains within the computational boundary. These geometries will require finer meshes, which will result in a larger number of unknowns. As shown in Table 1, solution time dramatically increases as the number of unknowns increases.

B. Cloak Approximation Using Homogenous Layers of Isotropic Material

Huang *et al.* implemented a simplified cloak using layered homogeneous materials to approximate a cloak's anisotropic material [20]. They use the fact a two-layered structure of homogeneous isotropic material can be treated as a single anisotropic medium provided the layers are small compared to wavelength. For a given set of two layers of material that are sufficiently thin, the effective permittivity values are [22]

$$\varepsilon_\theta = \frac{\varepsilon_1 + \eta\varepsilon_2}{1+\eta}, \tag{6}$$

$$\frac{1}{\varepsilon_\rho} = \frac{1}{1+\eta}\left(\frac{1}{\varepsilon_1} + \frac{\eta}{\varepsilon_2}\right), \tag{7}$$

where ε_1 and ε_2 are the relative permittivity of the two layers; and $\eta = d_2/d_1$ where d_i are the layer thicknesses. For this work, $\eta = 1$. They used equations (6) and (7) to derive the appropriate material parameters and thicknesses for a cylindrical cloak made out of homogeneous materials. They simulated a cloak which had the effective material properties similar to those of the reduced cloak put forth by Schurig *et al.* in [7] and obtained similar results.

Huang *et al.* did not use their method to approximate the functioning of an ideal cylindrical cloak, although they gave no reason why this could not be done. As a verification of their work, we performed a COMSOL simulation of an approximated ideal cloak. The spatial variation in the ideal cloak is first approximated using ten layers of homogeneous, anisotropic material, with the parameters ε_ρ and ε_θ evaluated at $\rho = \rho_n$ where ρ_n is the radial location of the n^{th} layer. Each homogeneous anisotropic layer is then approximated

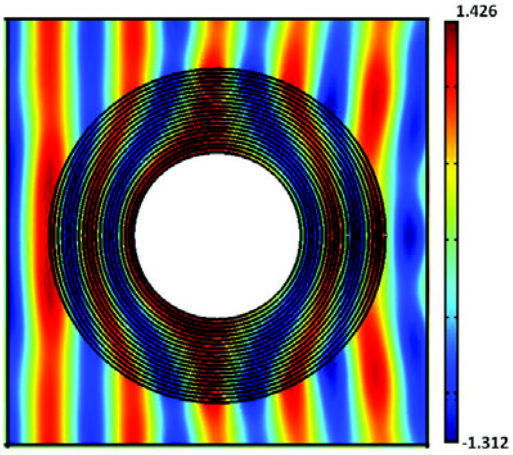

Fig. 2. Total magnetic field for an ideal cloak approximated using 20 layers of isotropic homogeneous material.

using two layers of homogeneous isotropic material with permittivity values defined by equations (6) and (7). Hence, 20 layers were used in this approximation. Layer values of μ_z were calculated for each layer by evaluating μ_z in equation (1) at $\rho = \rho_n$.

As shown in Fig. 2, small homogeneous layers can be used to adequately approximate the bulk anisotropic material parameters required for a cylindrical cloak. No comparison of this cloak's scattering width performance is done in this subsection, as the main point was to confirm Huang *et al.*'s method can be used to approximate an ideal cloak. Scattering width performance will be analyzed in a later section. We have confirmed a cloak can be realized using layers of homogeneous isotropic media, which leads directly to our Green's function implementation.

III. GREEN'S FUNCTION

Green's functions are commonly used in electromagnetic scattering problems. However, they have not been applied to solve radiation problems involving cloaks, likely due to the difficulty in their derivation due to the anisotropic nature of a cloak's material parameters. Methods similar to what we propose here has been used to study near and far field solutions for a PEC cylinder covered by an isotropic lossless layers [23], [24]. However, these analyses focused on the scattering properties of PEC cylinders layered with double-negative materials.

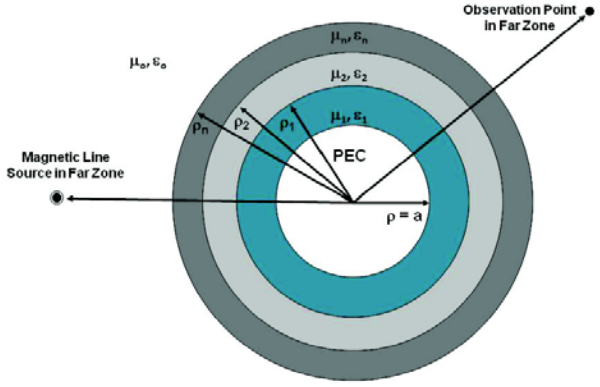

Fig. 3. Problem geometry for Green's function derivation.

As shown in Section II-B, a cylindrical cloak can be approximated by using concentric layers of isotropic material with homogeneous permittivity and permeability. To implement such a solution, consider a cloaked PEC cylinder of radius $\rho = a$ where the cloak is approximated by n layers of homogeneous material as shown in Fig. 3.

We developed the Green's function for a magnetic line source radiating in the presence of a PEC cylinder covered by n layers of homogeneous, isotropic material using the method described in [25]. The result is

$$\bar{G} = -\frac{j}{4}\sum_{m=0}^{\infty}\varepsilon_m \cos\left[m(\theta-\theta'\right] \left[J_m(k_o\rho_<) + \frac{B_m^{n+1}}{A_m^{n+1}} H_m^{(2)}(k_o\rho_<)\right] H_m^{(2)}(k_o\rho_>) \quad (8)$$

$$A_m^{n+1} = 1 \quad (9)$$

$$B_m^1 = -\frac{J_m^{'}(k_1 a)}{H_m^{'(2)}(k_1 a)} \quad (10)$$

where $\rho_<$, $\rho_>$ are the lesser of ρ and ρ' respectively, and θ, θ' are the observation and source angular locations. The remaining coefficients will be defined shortly. Note equation (8) is valid when observing the field where $\rho > \rho_n$ i.e. in the free space region.

Equation (8) contains components for the incident field and the scattered fields. The incident field is represented by the $J_m(k_o\rho_<)$ components while the scattered field is represented by the $H_m(k_o\rho_<)$ terms. Thus, we can rewrite the Green's function as two separate functions. We do this because our ultimate goal is to compute σ_{2D}, which we find as follows.

Without loss of generality, we will assume the magnetic line source is positioned at $\theta' = 180^o$. Additionally, we assume both the source and observation points are in the far zone. Using the large argument approximation for the Hankel function of the second kind [26], and knowing that in general, scattering width is found by

$$\sigma_{2D} = \lim_{\rho\to\infty} 2\pi\rho \frac{\left|H^s\right|^2}{\left|H^i\right|^2}, \quad (11)$$

the scattering width for a layered PEC cylinder with an incident TE plane wave traveling in the positive x direction is

$$\sigma_{2D} = \frac{2\lambda}{\pi} \frac{\left| \sum_{m=0}^{\infty} \varepsilon_m \cos(m\theta) \frac{B_m^{n+1}}{A_m^{n+1}} \right|^2}{\left| \sum_{m=0}^{\infty} \varepsilon_m (-j)^m \cos(m\theta) J_m(k_o b) \right|^2}. \quad (12)$$

The only unknowns in equation (12) are the B_m coefficients in the n layered regions. These coefficients are determined based on the junction conditions at the radial boundaries which force continuity of tangential magnetic and electric fields. Due to the PEC boundary at $\rho = a$, the value of B_m in the first region ($n = 1$) is known, which allows the remaining values to be found by solving a system of $2n$ equations.

To ensure the accuracy of the derived Green's function, we compared σ_{2D} calculated using the Green's function in equation (12) to the scattering width results obtained using a COMSOL simulation for a simplified cloak with material parameters put forth by Yan *et al.* and shown in equation (13).

$$\varepsilon_\rho = \left(\frac{\rho - a}{\rho} \right)^2 \frac{b}{b-a}, \; \varepsilon_\theta = \frac{b}{b-a}, \; \mu_z = \frac{b}{b-a}. \quad (13)$$

In order for the Green's function to accurately approximate a radially varying cloak as described in equation (13), the number of layers used in the formulation must be large. The Green's function results were determined using 5,000 layers to approximate the anisotropic material. The FEM results were obtained with MEL = 0.01λ. The calculated scattering widths from the two methods were very similar, as shown in Fig. 4. The Δ for the results in Fig. 4 was 0.004 m^2, which is quite good. Based on these results, we concluded our Green's function is an accurate method to obtain scattering width from cloaked cylinders. Next, we simulate various cloak geometries and compare the solution times using the Green's function and COMSOL.

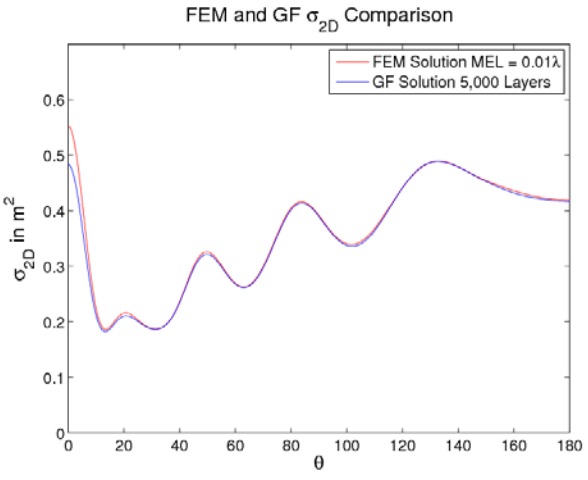

Fig. 4. Green's function and FEM results comparison.

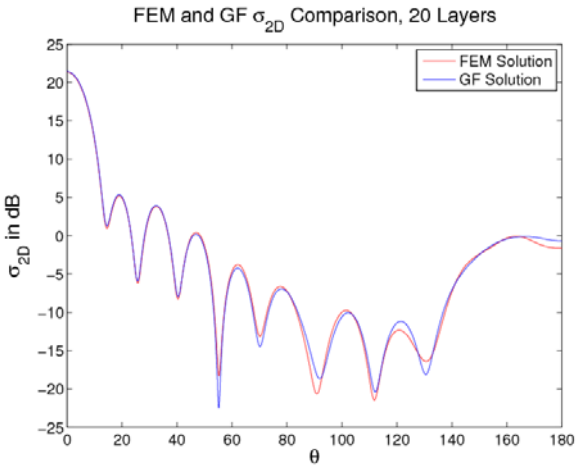

Fig. 5. Green's function and FEM results comparison for PEC with 20 layers.

IV. NUMERICAL BENEFIT

It is not yet possible to manufacture cloaks with the required spatially varying anisotropic parameters. Concentric rings of homogeneous anisotropic material can be used to approximate the spatial variation [7]. Such a realization can be simulated in COMSOL, but it is also well suited for our Green's function implementation. As an example, consider the COMSOL results shown in Fig. 2. Recall, this is a PEC surrounded by 20 layers of homogeneous material with material parameters chosen to approximate an ideal cloak. We simulated the same geometry using our Green's function and compared the scattering widths from the two methods. The results are shown in Fig. 5. We also compared the results from the two methods for a simulation using 40 layers of homogenous material to approximate an ideal cloak. These results are shown in Fig 6. Note these plots have σ_{2D} shown in dB rather than m^2 due to the large forward scattering.

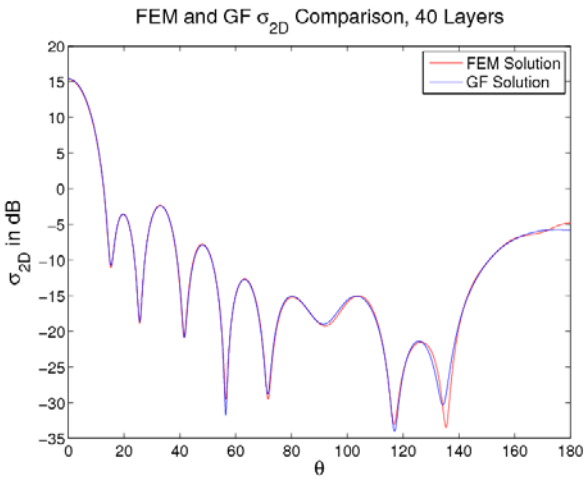

Fig. 6. Green's function and FEM results comparison for PEC with 40 layers.

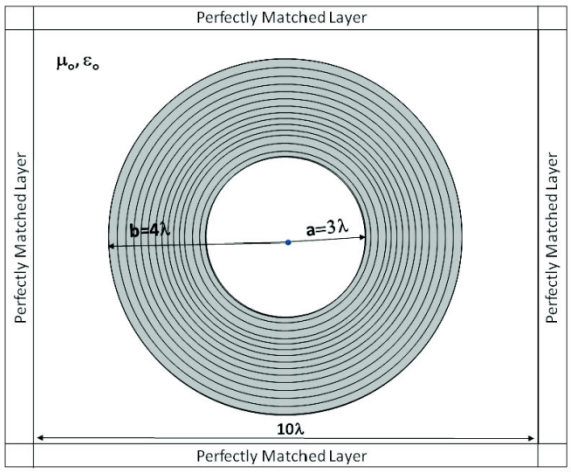

Fig. 7. Computational domain geometry for larger cloak sizes.

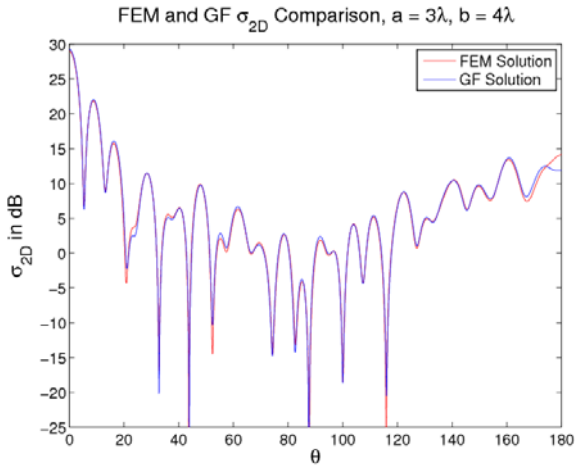

Fig. 8. σ_{2D} for larger cylinder and cloak sizes.

Note the similarities between the FEM and Green's function solutions. For the 20-layer simulation, Δ was 0.14 m^2, which shows good agreement between the two solutions. However, there is a noticeable difference in computation time. The Green's function solution took 2.28 s. The FEM solution was obtained by first creating a non-uniform mesh over the computational domain. This was necessary because the spacing between layers was only 0.05λ and 0.025λ for the 20 and 40-layer simulations respectively. A uniform mesh with MEL < 0.01λ was not possible due to memory limitations. The MEL in the concentric layers was limited to 0.007λ. This did not give us the desired number of elements in each layer for the 40-layer simulation, but this problem could not be avoided due to memory limitations. For the rest of the computation domain, an MEL = 0.05λ was used. For the 20-layer FEM simulation, the mesh had 911,004 elements and a solution time of 125 s.

The 40-layer simulation resulted in Δ = 0.04 m^2. The Green's function solution time was 2.82 s. The FEM solution used a similar non-uniform mesh with 881,892 elements and a solution time of 124 s. Obviously, the Green's function method is faster, particularly if a number of simulations are to be performed to conduct an optimization or an error analysis based on parameter or thickness variations in the layers. Additionally, if more layers are to be used, an FEM solution will require finer meshing within the layers, increasing the number of unknowns which will increase solution time.

Another benefit of using the Green's function to calculate scattering widths is when large cloak geometries are simulated. Up until this point, all previous simulations have used the cloak parameters such that $a = \lambda$ and $b = 2\lambda$. If a and b are increased, the computational domain in an FEM simulation increases. This will increase the number of unknowns if the same limits on MEL are used, ultimately resulting in a longer solution time. The MEL can be increased in order to prevent out-of-memory errors during solution at the penalty of reduced accuracy. Increasing the cloak radii in the Green's function does result in having to include more terms in the summation, but this increase in computational budget is minimal compared to the increased burden in an FEM simulation. As an example, consider the simulation geometry shown in Fig. 7. More elements are going to be needed

since the computational domain is 10λ×10λ. We performed a simulation of a 20-layer cloak of homogeneous material approximating the material parameters shown in equation (13) using COMSOL and our Green's function. The results are shown in Fig. 8. The Δ between the two simulations was 1.39 m^2, still reasonable, but getting worse due to the fact MEL had to increase in some portions of the geometry.

To reduce memory requirements for the FEM solution, a non-uniform mesh was applied. The MEL for the concentric ring was 0.01λ, while for the remaining areas, MEL = 0.3λ. Note the MEL has been increased compared to the same 20-layer simulation where $a = \lambda$ and $b = 2\lambda$, meaning FEM solution accuracy will decrease. The mesh consisted of 972,698 elements and a solution time of 116 s. In addition to the solution time, the code took 168 s to simply create the mesh. The solution time for the Green's function was 3.89 s, slightly longer due to the fact $m = 31$ in the summation due to the requirement in equation (4). Further increases in cloak size result in having to significantly increase MEL in order prevent mesh size from growing beyond the computational capabilities. The Green's function formulation can handle the larger problem sizes with a minimal impact to computation time.

V. CONCLUSION

We have shown a Green's function approach for determining scattering widths from a cylindrical cloak results in a significant computational savings. This savings can be useful if an error analysis or optimization studies are to be performed on a particular cloak geometry. Additionally, the computational domain size is directly related to the cylindrical cloak's radius. A larger cloak results in a larger domain size. The increase in computational domain requires either a longer solution time due to the increased number of elements or a reduction in mesh density which impacts solution accuracy. The Green's function implementation is much faster than an FEM solution and is more adept at handling larger problem geometries.

ACKNOWLEDGEMENTS

The views expressed in this paper are those of the authors and do not reflect the official policy or position of the United States Air Force, Department of Defense, or the United States Government.

REFERENCES

[1] J. B. Pendry, D. Schurig, and D. R. Smith, "Controlling electromagnetic fields," *Science*, vol. 312, no. 578, pp. 1780–1782, 2006.

[2] D. Schurig, J. B. Pendry, and D. R. Smith, "Calculation of material properties and ray tracing in transformation media," *Opt. Express*, vol. 14, no. 21, pp. 9794–9804, 2006.

[3] U. Leonhardt and T.G. Philbin, "General relativity in electrical engineering," *New J. Phys.*, vol. 8, no. 10, 2006.

[4] H. Chen, B.-I. Wu, B. Zhang, and J. A. Kong, "Electromagnetic wave interactions with a metamaterial cloak," *Phys. Rev. Lett.*, vol. 99, no. 6, 2007.

[5] Z. Ruan, M. Yan, C. W. Neff, and M. Qiu, "Ideal cylindrical cloak: Perfect but sensitive to tiny perturbations," *Phys. Rev. Lett.*, vol. 99, no. 11, 2007.

[6] A. J. Ward and J. B. Pendry, "Refraction and geometry in Maxwell's equations," *J. Mod. Opt.*, vol. 43, no. 4, pp. 773–793, 1996.

[7] D. Schurig, J. J. Mock, B. J. Justice, S. A. Cummer, J. B. Pendry, A. F. Starr, and D. R. Smith, "Metamaterial Electromagnetic Cloak at Microwave Frequencies," *Science*, vol. 314, no. 5801, pp. 977–980, 2006.

[8] W. Cai, U. K. Chettiar, A. V. Kildishev, V. M. Shalaev, and G.W. Milton, "Nonmagnetic cloak with minimized scattering," *Appl. Phys. Lett.*, vol. 91, no. 11, 2007.

[9] M. Yan, Z. Ruan, and M. Qiu, "Scattering characteristics of simplified cylindrical invisibility cloaks," *Opt. Express*, vol. 15, no. 26, pp. 17772–17782, 2007.

[10] P. J. Collins and J. S. McGuirk, "A novel methodology for deriving improved material parameter sets for simplified cylindrical cloaks," *J. Opt. A: Pure Appl. Opt.*, vol. 11, no. 1, 2009.

[11] S. A. Cummer, B. -I. Popa, D. Schurig, D.R. Smith, and J. Pendry, "Full-wave simulations of electromagnetic cloaking structures," *Phys. Rev. E: Stat. Phys., Plasmas, Fluids*, vol. 74, no. 3, 2006.

[12] H. Ma, S. Qu, Z. Xu, J. Zhang, B. Chen, and J. Wang, "Material parameter equation for el-

liptical cylindrical cloaks," *Phys. Rev. A: At. Mol. Opt. Phys.*, vol. 77, no. 1, 2008.

[13] D.-H. Kwon and D. H. Werner, "Two-dimensional eccentric elliptic electromagnetic cloaks," *Appl. Phys. Lett.*, vol. 92, no. 1, 2008.

[14] M. Rahm, D. Schurig, D. A. Roberts, S. A. Cummer, D. R. Smith, and J. B. Pendry, "Design of electromagnetic cloaks and concentrators using form invariant coordinate transformations of Maxwell's equations," *Photon. Nanostruct.: Fundam. Appl.*, vol. 6, no. 87, 2008.

[15] W. X. Jiang, T. J. Cui, G. X. Yu, X. Q. Lin, Q. Cheng, and J. Y. Chin, "Arbitrarily elliptical-cylindrical invisible cloaking," *J. Phys. D: Appl. Phys.*, vol. 41, 2008.

[16] W. X. Jiang, J. Y. Chin, Z. Li, Q. Cheng, R. Liu, and T. J. Cui, "Analytical design of conformally invisible cloaks for arbitrarily shaped objects," *Phys. Rev. E: Stat. Phys., Plasmas, Fluids*, vol. 77, no. 6, 2008.

[17] Y. Zhao, C. Argyropoulos, and Y. Hao, "Full-wave finite-difference time domain simulation of electromagnetic cloaking structures," *Opt. Express*, vol. 16, no. 9, pp. 6717–6730, 2008.

[18] R. Weder, "A rigorous analysis of high-order electromagnetic invisibility cloaks," *J. Phys. A: Math. Theor.*, vol. 41, 2008.

[19] Z. Liang, P. Yao, X. Sun, and X. Jiang, "The physical picture and the essential elements of the dynamical process for dispersive cloaking structures. *Appl. Phys. Lett*, vol. 92, no. 13, 2008.

[20] Y. Huang, Y. Feng, and T. Jiang, "Electromagnetic cloaking by layered structure of homogeneous isotropic materials," *Opt. Express*, vol. 15, no. 18, pp. 11133–11141, 2007.

[21] C. A. Balanis, *Advanced Engineering Electromagnetics*. John Wiley & Sons, Inc, Hoboken, New Jersey, 1989.

[22] B. Wood, J. B. Pendry, and D. P. Tsai, "Directed subwavelength imaging using a layered metal-dielectric system," *Phys. Rev. B: Condens. Matter*, vol. 74, no. 11, 2006.

[23] S. Arslanagic and O. Breinbjerg, "Electric-line-source illumination of a circular cylinder of lossless double-negative material: An investigation of near field, directivity, and radiation resistance," *IEEE Antennas Propag. Mag.*, vol. 48, no. 3, pp. 38–54, 2006.

[24] H. Yao, L. Li, and C. Qiu, "Electromagnetic scattering properties in a multilayered metamaterial cylinder," *IEEE Mediterranean Electrotechnical Conference*, May 2006.

[25] R. E. Collin, *Field Theory of Guided Waves*. John Wiley & Sons, Inc, New York, New York, second edition, 1991.

[26] M. Abramowitz and I. A. Stegun, editors, *Handbook of Mathematical Functions with Formulas, Graphs, and Mathematical Tables*. Dover Publications, Inc., New York, New York, 1970.

Jeffrey S. McGuirk received the B.S. degree in electrical engineering from the United States Air Force Academy, Colorado Springs, Colorado in 1995, the M.S. degree in electrical engineering from Iowa State University, Ames, Iowa in 1996, and the Ph.D. degree from the Air Force Institute of Technology, Dayton, OH in 2009. He is a member of the Eta Kappa Nu and Tau Beta Pi honor societies and has authored or co-authored five technical papers. He is currently at the Air Force Research Laboratory, Sensors Directorate, Wright-Patterson AFB, OH researching development of new and novel materials capable of producing intriguing electromagnetic effects.

Peter J. Collins received the B.A. degree from Bethel College, Arden Hills, MN, in 1985, the B.S. degree in electrical engineering from the University of Minnesota, Minneapolis, in 1985, and the M.S. and Ph.D. degrees from the Air Force Institute of Technology, Dayton, OH, in 1990 and 1996, respectively. He is a senior member of the IEEE, member of the Eta Kappa Nu and Tau Beta Pi honor societies, and is author or co-author of over 50 technical papers. Dr. Peter J. Collins is Associate Professor of Electrical Engineering with the Air Force Institute of Technology, Department of Electrical and Computer Engi-

neering, Wright-Patterson AFB, OH. Dr. Collins' research interests are in the areas of Low Observables, Electromagnetic Materials Design, and Remote Sensing along with the underlying foundational disciplines of Electromagnetic Theory, Computational Electromagnetics, and Signature Metrology.

Michael J. Havrilla received B.S. degrees in Physics and Mathematics in 1987, the M.S.E.E degree in 1989 and the Ph.D. degree in electrical engineering in 2001 from Michigan State University, East Lansing, MI. From 1990-1995, he was with General Electric Aircraft Engines, Evendale, OH and Lockheed Skunk Works, Palmdale, CA, where he worked as an electromagnetics engineer. He is currently an Associate Professor in the Department of Electrical and Computer Engineering at the Air Force Institute of Technology, Wright-Patterson AFB, OH. He is a member of URSI Commission B, a senior member of the IEEE, and a member of the Eta Kappa Nu and Sigma Xi honor societies. His current research interests include electromagnetic and guided-wave theory, electromagnetic propagation and radiation in complex media and structures and electromagnetic materials characterization.

Aihua Wood received the B.S. from Peking University, China, in 1984, MS and Ph.D. from the University of Connecticut in 1988 and 1990 respectively, all in applied mathematics. She was Visiting Assistant Professor at the Naval Postgraduate School in Monterey, CA for three years, Assistant Professor at the Penn State University Eire for one year before joining the faculty at the Air Force Institute of Technology in 1994. She has been a full professor of mathematics since 2002. Dr. Wood's research interests include partial differential equations, electromagnetic scattering, computational fluid dynamics, and finite element analysis. She has published over 40 archival journal articles.

Optimum Horn Antenna Design Based On an Integration of HFSS Commercial Code and Genetic Algorithms for the Feed Application of Reflector Antennas

Hsi-Tseng Chou[1], Chia-Wei Liu[2], Hsi-Hsir Chou[3] and Wen-Jiao Liao[4]

[1]The Department of Communication Engineering
Yuan Ze University, Chung-Li 320, Taiwan
hchou@saturn.yzu.edu.tw

[2] ElectroScience Laboratory,
The Ohio State University, Columbus, OH 43212, USA

[3] The Department of Engineering
Cambridge University, Cambridge, U.K.

[4] The Department of Electrical Engineering
National Taiwan University of Science and Technology, Taipei, Taiwan

***Abstract*—** The optimum design of horn antennas for the application as feeds to reflector antennas is performed utilizing a simulation tool based on an integration of HFSS commercial code as an electromagnetic computational engine and an add-on optimization scheme of genetic algorithm. This work is motivated by the need of antenna operations at multiband frequencies, where the horn antennas tend to radiate narrower beams at higher frequencies and result in inefficient uses of the reflector surface since the narrow beams will illuminate only a portion of the reflector surface. Optimum design of the horn antenna may significantly increase efficiency. The philosophy of this work is based on a fact that the currently available commercial codes are reliable and relatively accurate in the analysis with more efforts tending to enhance the computational efficiency. The quality of the antenna design will mainly rely on an effective optimization algorithm that can be and should be developed independently according to engineers' own need, since the variables and cost functions for optimization can be flexibly selected. The integration of existing analysis codes, as mentioned above, and self-developed algorithms will be most effective for an engineer in the customized antenna design. The concepts and strategies are addressed with numerical examples to validate.

***Index Terms*—** Reflector Antenna, Feed Horn, Genetic Algorithm, Optimization Algorithm, Code Integration.

I. INTRODUCTION

The boom of satellite communications for digital TV program reception [1] has increased the uses of reflector antennas that provide sufficiently high gain and directivity. The increasing trend for using reflector antennas is in the multiband and multi-satellite operations by utilizing a single reflector with either multi-feeds, pointing to various satellites and operating independently at various frequencies, or a single feed operating at multiple frequencies [2]. The requirements for feed radiations become very strict since a single reflector is desired to be used. First of all, the electrical sizes of the reflector antenna increase with the increases of frequencies even though its physical size remains same. At higher frequencies of operation, the reflector has a larger electrical size in terms of wavelengths. Similarly, a horn antenna operated at a higher frequency has a larger aperture size in terms of wavelengths, and radiates narrow beams [3]. They will illuminate only a portion of the reflector's surface if the reflector surface is

designed to meet the requirements of a low frequency operation. One typical example is the simultaneous use of 20 and 30 GHz frequency bands for a reflector antenna, which is popularly employed in satellite communications. Thus, at higher frequencies the efficiency of utilizing the reflector surface can be relatively low unless the radiation patterns of the feeds at the multiple frequencies are simultaneously optimized to provide a global maximum efficiency for the utilization of the reflector surface.

It is thus motivated in this paper to develop useful simulation tools that can be efficiently employed in the design of such optimum horn antennas to avoid the need of tuning antenna parameters in an ad hoc manner, which is relatively time consuming and inefficient. Prior works have attempted to integrate EM numerical methods and optimization approaches such as the genetic algorithm [4─6]. Chen et. al [7] demonstrates that the NEC code can be integrated within an GA-based automated fish bone antenna design optimizer.

Considering the development of design tools, currently available commercial codes based on finite element method [8], HFSS [9], have been shown to be very reliable and relatively accurate in the electromagnetic (EM) analysis of antenna performance with most of the current efforts tending to enhance the computational efficiency. Thus, the quality of the antenna design and its performance will mainly rely on an effective optimization procedure that can be and should be developed independently according to engineers' own needs. An automatic optimization procedure may significantly save the engineers' efforts, which were spent in tuning the antenna structures manually. It is noted that even though some simple optimization functions are available in HFSS, however, the framework of this paper allows the variables and cost functions for optimization be flexibly selected and defined. Also, the engineers can focus on developing their own design procedure and algorithms to optimize the antenna designs to the best extent of their experiences and knowledge. The integration of this existing analysis code and self-developed algorithms is apparently most effective for an engineer in the customized antenna design. Furthermore, it may extend the application scopes of the simulation tool since a variety of new features may be developed.

This code integration is developed to automate the optimization process. A program is established to monitor the optimization process and interact with the computation engine, which is HFSS in this paper, to optimize the radiations of the feed horn antennas. It may, however, be extended to treat a variety of antenna types since the fundamental concepts and code structure remain similar. The procedure begins with an initial setting within the framework of HFSS. The computation engine returns prescribed performance parameters (i.e., radiation patterns, return loss, etc.). The program next adjusts the stepping size of the adjustable parameters according to its built-in optimization algorithm. The above process is performed iteratively until the desired performance or the specified iteration number is met. In this paper, genetic algorithm (GA) [10─12] is employed to realize the concept because it can be effectively employed to optimize discrete variables.

As to its application potentials, such an add-on optimization program could be made more capable than the optimization functions provided by commercial simulation packages. The optimization criteria are not limited to antenna structure parameters, and can be the structure itself, which is suitable for antenna design using genetic algorithms. Furthermore, design packages from different venders could be coordinated using this intermediate program, and thus create most values in the antenna design. A potential example is to further integrate the EM analysis code of the reflector antennas [13, 14], which will make the design of the entire reflector antenna system in a self-completeness fashion. This extension will be reported in the future phase of this work.

This paper is formatted in the following order. Section 2 addresses the implementation strategies of this code integration as well as the interfaces to interact with the HFSS. Section 3 demonstrates the concepts by considering the radiation patterns optimization of a single band and a dual-band horn antenna designs for the application of reflector's feed in the satellite communications. Finally a short discussion is presented in section 4 for a conclusion.

II. IMPLEMENTATION STRATEGIES

A. General Concepts and the Program Structure

The concept of this work follows a general

optimization procedure of an antenna design as illustrated in Figure 1(a). It starts with an initial guess of the horn antenna structure and parameter inputs to classify the antenna radiation through the EM analysis using HFSS. The antenna radiations are justified by a comparison with the expectations, such as beamwidths, sidelobe levels and cross-polarizations, through an evaluation of a cost function or a fitness function. If the expectations have been reached, then the design procedure is completed. Otherwise, new designs with improved radiation characteristics are created based on the changes in the values of the fitness function, where the new antenna structures are produced by a GA procedure. Those new antenna structures are used in the next iteration (or next generation) for HFSS analysis to justify their performances with respect to the expectations. This procedure continues until the expectations are reached.

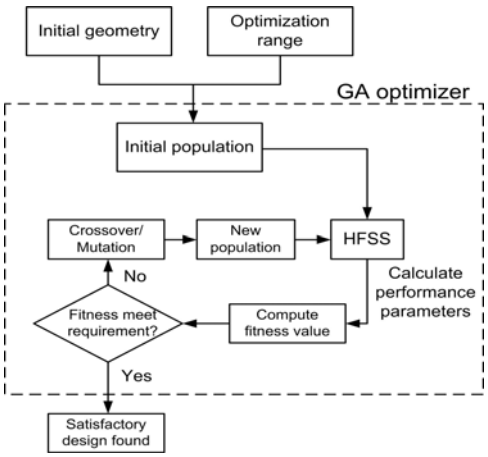

Fig. 1. The optimization procedure of a feed horn antenna design as well as the program structure of the proposed strategies to integrate HFSS commercial analysis code within the genetic algorithm.

To realize the concepts with respect to the utilization of HFSS as an EM analysis engine with an add-on procedure of GA to adjust the antenna's parameters. It is established within a framework of an automation control program that first sets up the program control parameters such as the expectations of the desired radiation patterns and the maximum number of iterations, and then establishes the procedures of code control and optimization algorithm. The initial antenna setting is analyzed by HFSS to estimate antenna performance which is used to compute the fitness values. Thus the parameters with respect to the antenna operation, such as the operational frequency bands and radiation analysis, are input through the automation program to HFSS. The main body of the automation program is composed by four blocks. The "geometry controller" specifies the parameters and variables of the antenna structure to be optimized such as the dimensions and coordinates of particular geometries in the structure, which are used in the "GA operator" block to produce new values for creating a new antenna structure with superior performance. The "GA operator" implements the GA algorithm. Also the antenna performance with respect to the design anticipation is evaluated in the "fitness function" block to justify whether the expectation has been reached based on the analysis of "HFSS simulation" block which uses the HFSS as the EM analysis tool. If the fitness value meets the prescribed conditions of requirement, we can declare that a satisfying design is found. Otherwise, the GA operator will sort designs according to the fitness values, then generate new designs as well as new values of the parameters for the next generation from superior designs.

B. Genetic Algorithm for Antenna Design Optimization ("GA operator" block)

GA is employed to optimize the antenna structure to meet the prior requirements of the antenna operation. It sorts the design according to computed values of the fitness function, and creates new designs according to the superior designs from previous generations as illustrated in Figure 2(a). For the case shown, there are eight genes (n=8) representing eight antenna design. Each gene comprises a set of parameters' values for an individual antenna designs. The genes are created from superior parents in attempt to generate even better performance. The values of the fitness function are computed for each gene, and compared to justify the superiority of the antenna performance. In Figure 2(a) it is assumed that a larger fitness value indicates a superior performance of the antenna associated with this gene. The superior genes are retained while the rest are abandoned in the next generation. New genes are produced from the superior parent genes (i.e., the superior genes retained in the previous

generation) based on a roulette wheel parent selection approach. The creation of the new genes uses either crossover or mutation methods as illustrated in Figure 2(b). The crossover method means that design parameters are swapped between two parent designs, while the mutation method implies that a parameter of the parent gene is replaced with a randomly generated number. The decision of using either crossover or mutation method is also random. The selection of parent designs is done via the roulette wheel method, that is, a superior design is assigned to a larger piece in the wheel, which is equivalent to a larger probability density value. Therefore, superior parents are more likely to produce more children. In this work, the crossover and mutation are performed based on the operations over the binary codes of the parents' genes. For the crossover method, assuming the values of each parameter of a gene are represented by N_g bits, and randomly selecting an integer number, N_c ($1 \leq N_c \leq N_g$), the corresponding parameter of the offspring gene, X_o, is produced by extracting the first N_c bits from the parameter of the first parent gene, $X_{p,1}$, and the last ($N_g \leq N_c$) bits from that of the second parent gene, $X_{p,2}$. Similarly mutation is performed based on randomly selected bits of the parent gene, and the polarities of the selected bits are inverted. These crossover and mutation operations are subsequently performed over every parameter of a gene.

After the prescribed number of iterations has been performed, the gene with the largest fitness value is chosen as the optimized antenna design.

C. Interface to Interact with HFSS

(1) Initial parameter setup:

Within the framework of the automation control program, a subroutine is established to specify the configurations of the horn antenna including the geometrical parameters. An initial antenna setting is first performed within the work of this subroutine. The fundamental parameters such as the sampled frequencies,

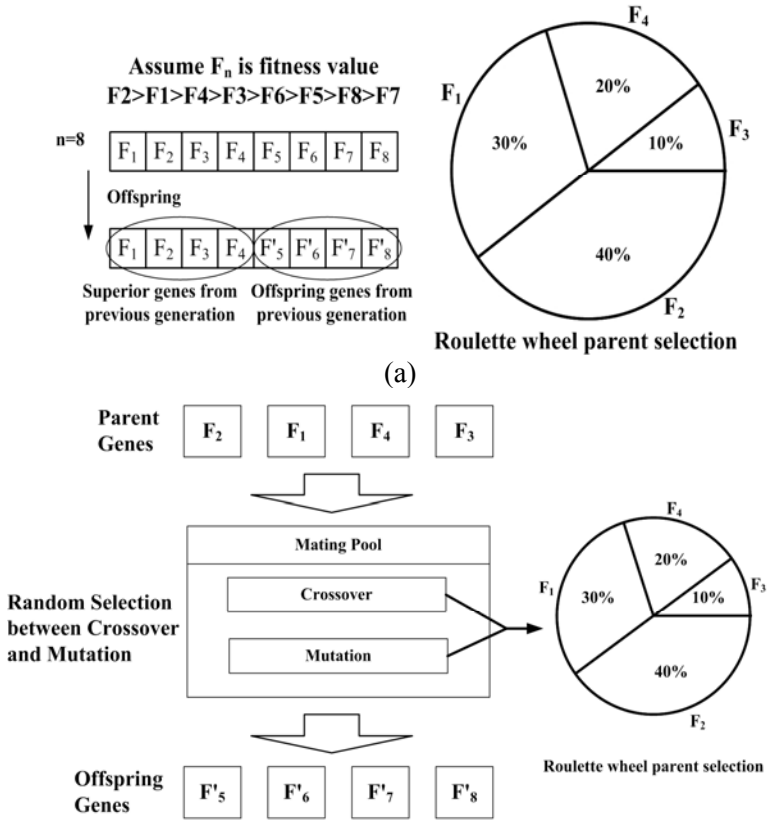

Fig. 2. The illustration of genetic algorithm to generate new antenna structures with superior performance: (a) general concepts and (b) production of superior offspring genes.

radiation patterns and geometries of antenna structures are assigned tentatively. This subroutine transforms the values of the parameters into a script file (called VBScript file by HFSS [9]) that can be recognized by HFSS, and then passes the parameters to the HFSS to perform the EM analysis and compute the radiations patterns of the initial antenna structure.

The selection of the initial antenna structure plays a dominant role for the success of the optimization procedure. It should be capable of providing the essential possibility to achieve the design goal since the optimization procedure tends to fine tune the values of the antenna's parameters instead of altering the structure dramatically. For example, if equal beamwidth in the radiation band is desired, the changes in antenna's parameters should result in substantial difference in radiation patterns for the first few iterations and gradually converge until the optimum design is reached. In this case, the GA procedure will tune the parameter values to adjust the radiation patterns in an effective fashion until the designated beamwidth features are obtained.

(2) Interaction with the HFSS by a VBScript file

Interactions of the subroutines within the automation control program with HFSS are performed by using a VBScript file which can be executed in HFSS. In this case, the commands and functions within the antenna configuration subroutine that specify the antenna structures can be properly identified and transformed into the format recognizable by HFSS. The antenna model is then established within the HFSS GUI program. Commands and functions that read the antenna radiation data can be similarly established by identifying the commands in the HFSS VBScript file, which can be used to compute the fitness functions. The following statements show an example of HFSS's internal functions that define a "Waveport Port" [9] for the excitation of the horn antenna within a waveguide:

```
oModule.AssignWavePort _
Array( _
"NAME:WavePort", _
"NumModes:=", 1, _
"PolarizeEField:=", false, _
"DoDeembed:=", false, _
"DoRenorm:=", false, _
Array("NAME:Modes", _
Array("NAME:Mode1", _
"ModeNum:=", 1, _
"UseIntLine:=", false) _
), _
"Objects:=", Array("circle"))
```

They can be established by using the fprintf command in C-language. For example, the function can be set up by following statement:

```
fprintf(fid, "%s%c%s%c%s", "Set oModule =
oDesign.GetModule(",symbol,"BoundarySetup",
symbol,") \n");
```

Other functions of HFSS can be established in a similar fashion, and are not repeated here for simplification.

(3) Intervention with HFSS Execution via key-board controlling keys

The execution of the entire antenna design procedure is performed within the control program. The program knows when to call the HFSS for EM analysis, when the HFSS has completed the analysis, how to access the antenna radiation data and where to pass the parameters between HFSS and the GA operator via the VBScript file and data files. The access of HFSS is performed by simulating key-board controlling keys using C-languages commands and ANSI codes [15] for English characters. The key-board controlling keys allow one to run the functions of HFSS through its GUI program. Two examples of running the HFSS analysis and retrieving the radiation patterns from HFSS, which are key functions required in this code integration, are demonstrated. The execution of other functions within HFSS can be performed similarly. The following statements are part of the C-language commands that are used to execute a VBScript file named "modify", which perform the antenna model establishment and execute the HFSS analysis:

```
1    ShowWindow(handle,SW_SHOW
NORMAL);
2    SetForegroundWindow(handle);
3    SetActiveWindow(handle);
4
5    keybd_event(VK_MENU,0,0,0);    //key
"alt"
```

```
6       keybd_event(84,0,0,0);          //key "T"
7       Sleep(100);
8       keybd_event(VK_MENU,0,KEYEVENT
F_KEYUP,0); //Release key "alt"
9     keybd_event(84,0,KEYEVENTF_KEYUP,0);
        //release key "T"
```

The above statements emulate the keyboard strokes and hence provide a means to communicate with HFSS. Their results are illustrated in Figure 3. Lines 1─3 lock the HFSS GUI windows so that the following operations can be performed without being interfered by other codes running in the computer. Lines 5─9 execute the input of key-board command "Alt-T" and will open an HFSS window pending from "Tools" icon to run script commands as shown in Figure 3(a). There are also other lines that simulate the input of key "s" from keyboard, which will open the window for file access from the hard disk to run a script file. Thus a window is opened for inputting the filename of the script file, where a script file named "modify" is input one character after another using above fashion. Figure 3(b) shows the dialog window evoked.

After the HFSS analysis, the data of the radiation patterns should be retrieved. Using statements similar to the one shown above, data can be retrieved and saved into a file that can be accessed by the automation program to compute the values of the fitness functions. Note that the statements should be repeated if multiple sets of data are required in the optimization procedure. For example, the radiation patterns of different observation planes can be treated as different sets of data and one should execute the statements separately.

After all radiation patterns are saved as external files, they may be employed in the automation program to compute the fitness values, and can be subsequently used in the GA procedure to produce a better design in the iterative procedure.

III. DEMONSTRATION EXAMPLES

A. Single Band Horn Antenna Design with Similar Beamwidths at Two Principal Planes

The first example considers the design of a single band horn antenna for radiation with equal beamwidths at two principal planes so that it can be employed as a feed to a rotationally symmetric reflector antenna. The operation frequency is assumed to be 20 GHz. A -10 dB normalized beamwidth of 60 degrees (i.e., ±30 degrees) is pursued in this design. The antenna structure considered is illustrated in Figure 4, where the corrugations are perpendicular to the antenna aperture in consideration for mass production. In this case, 3 corrugations are implemented, and 13 parameters associated with depth, width and thickness of the corrugations are employed as the variables to be adjusted along the optimization

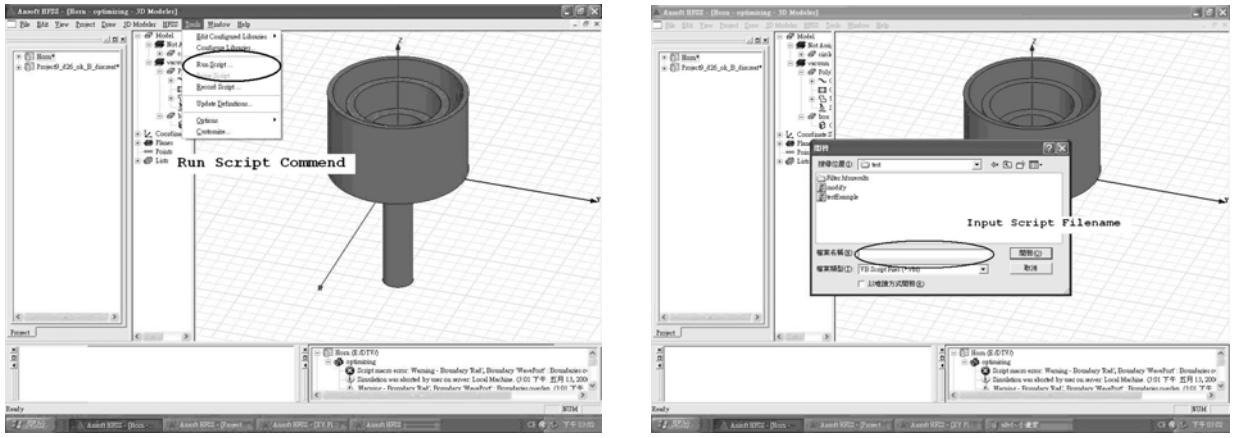

(a) (b)

Fig. 3. The procedure within HFSS GUI to execute a VBScript file: (a) "Alt-T" to open the window of the "Tools" icon, and (b) run a script file.

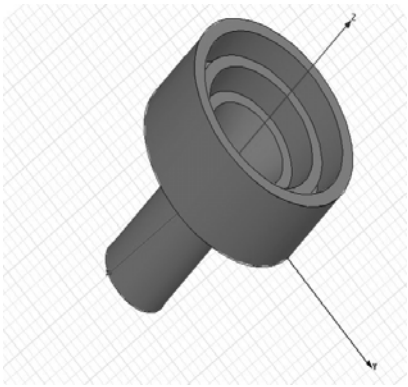

(a)

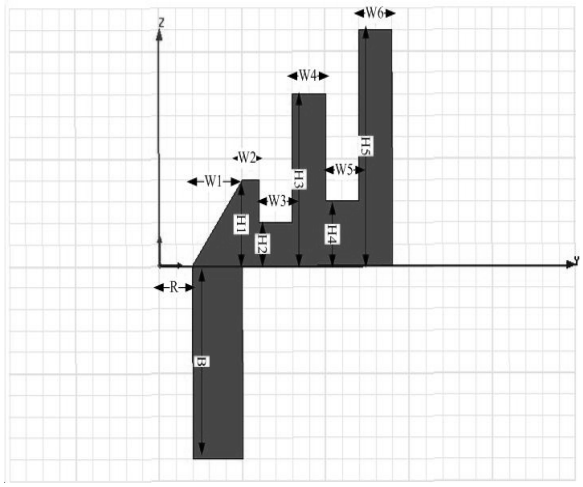

(b)

Fig. 4. The corrugated horn antenna structure for the feed to a reflector antenna. The corrugation is perpendicular to the antenna aperture for the convenience of a mass production: (a) horn structure and (b) cross section and parameters.

procedure so that the overall radiation patterns can be rotationally symmetric along the boresite. Note that 8 bits are employed to each parameter of the antenna structure in this case.

The radiation patterns at the two principal planes are used to calculate the fitness function, where the fitness function for the n^{th} gene is defined by

$$F_n = \frac{1}{\left(1+\sum_{m=1}^{M}\Delta G_{nm}\right)\left(1+\sum_{p=1}^{2}\Delta B_{np}\right)}, \tag{1}$$

where

$$\Delta G_{nm} = \begin{cases} \left|G_{nm,E} - G_{nm,H}\right| & \left|G_{nm,E} - G_{nm,H}\right| > G_{tol} \\ 0 & \left|G_{nm,E} - G_{nm,H}\right| \le G_{tol} \end{cases}, \tag{2}$$

$$\Delta B_{np} = \begin{cases} \left|B_{np} - B_{req}\right| \Big/ B_{req} & \Delta B_{np} \Big/ B_{req} > B_{tol} \\ 0 & \Delta B_{np} \Big/ B_{required} \le B_{tol} \end{cases}. \tag{3}$$

In (2), $G_{nm,E}$ and $G_{nm,H}$ are the radiation gain patterns sampled at E- and H-planes, respectively (assuming M samples at each plane), and G_{tol} is the allowable tolerance for the pattern difference at the two principal planes. In general specifying main beam pattern and first sidelobe level is enough for good performance since the corrugated horn antenna has characteristics of low sidelobes. The difference between the patterns at the two principal planes is computed in (2). If the difference is larger than the allowable tolerance, then it is included in the computation of fitness value. On the other hand, if the difference is smaller than the tolerance, then the patterns are considered as being matched and the difference is ignored. Note that each set of genes represents an individual antenna structure, and thus the pattern difference should be computed for each gene. In this case, 10 genes (n = 1 ~ 10 in (1)) are employed in the GA optimization.

Similarly, B_{np}(p = 1, 2) specify the -3dB beamwidth at the two principal planes so that the radiation patterns can satisfy the required beamwidth, B_{req}. In fact, (3) computes the differences of the beamwidths. If the difference is larger than the allowable tolerance, B_{tol}, then it is included in the computation of fitness function. However, if the difference is smaller than the tolerance, it is ignored since the beamwidth requirement is satisfied.

The summations of ΔG_{nm} and ΔB_{np} contribute to the denominator of F_n. A proper design, which meets the pattern specifications, will yield a fitness value of one (F_n = 1) that is the largest value possible in the optimization procedure. A larger F_n value implies a superior performance as required in the GA procedure. Figure 5(a) shows the radiation patterns of an initial arbitrary geometry setting with parameters specified in Table 1, where it is observed that the pattern at ϕ = 0° plane has a larger

beamwidth than that at $\phi = 90°$ plane. In particular, the -10 dB beamwidths are 70° and 55° at $\phi = 0°$ and $\phi = 90°$ planes, respectively. It is noted that this initial setting of waveguide radius is 2.873mm, which makes the operational frequency below the cutoff frequency of a fundamental mode propagation. Thus the antenna will not radiate and makes the simulated gain severely small (roughly -76dBi). The proposed tool will automatically correct this problem and optimize the structure until it fulfills the desired requirements. Figure 5(b) shows the radiation patterns of the optimized antenna design, where one has observed almost identical main beam patterns at the two principal planes. In particular, the -10 dB beamwidth is 58 degrees as required in the design criterions. The values of the optimized parameters are also shown in Table 1 for comparison. In this design optimization, the analysis of each antenna structure costs 8 minutes of CPU time running on an AMD K8 3000 (with 1 GB RAM) computer. The overall CPU time is 26.7 hours for the entire optimization procedure, where approximately 250 antenna structures have been analyzed with HFSS. Note that most of the CPU time was spent in evaluating radiation patterns from various designs in the population via HFSS while the CPU time spent in performing crossover/mutation operations is negligible.

B. Horn Antenna Design with Equal Beamwidths in Radiation Patterns at Two Operation Frequencies

The second example considers a dual band horn antenna design that is operated at 20 and 30 GHz. The antenna is employed as the feed of a reflector antenna. Thus it is desired for the horn antenna to radiate with equal beamwidths so that the reflector surface can be well illuminated at the two different bands. In this case, the design goal is to have a -10dB beamwidth of 70 degrees with maximum gains. Similar to the previous example, a corrugated horn structure illustrated in Figure 4 is employed. Values of the initial setting parameters are given in Table 2. Total of 13 parameters are employed to specify the antenna structure. The terrible radiation patterns of the initial setting are shown in Figure 6(a). The gains at 20 and 30 GHz are less than -72 dBi. Furthermore, similar to the previous example, most of the energy return back to the waveguide and doesn't radiate because

Table 1: The initial and optimized values of the antenna dimensions for the first example.

Parameter Name	Initial Values (mm)	Optimized Values (mm)
R	2.873	4.4444
B	24.206	26.667
W1	2.4286	4.86
W2	1	1
W3	1	1
W4	1	1
W5	1	1
W6	1	1
H1	7.2222	14.365
H2	3.8571	3.143
H3	14.841	21.825
H4	7.2222	15.317
H5	15.794	26.889

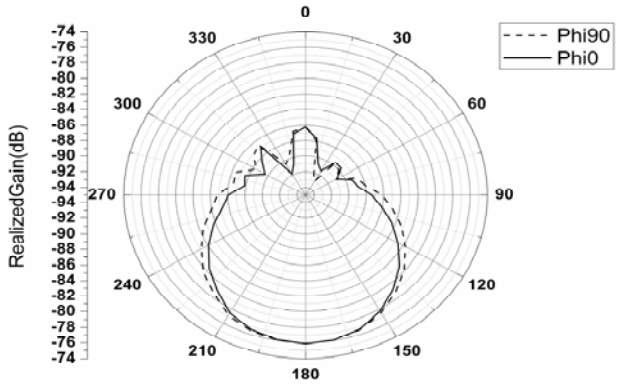

(a)

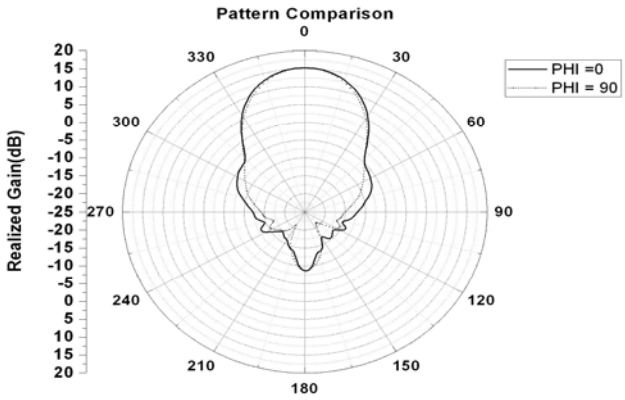

(b)

Fig. 5. Radiation patterns of the horn antenna at the two principal planes before (a) and after the optimization (b). The desired radiation direction in (a) should point to 0 degree as achieved in (b).

the fundamental mode is not supported in this initial guess of waveguide radius. The GA algorithm adjusts the dimensions of the corrugations to optimize the radiation patterns at these two frequency bands. The radiation patterns at the two principal planes are employed to justify the required beamwidth performance. The four sets of patterns were employed to compute the fitness function. The fitness function for n^{th} set of genes is defined similarly by

$$F_n = \frac{1}{\left(1+\sum_{m=1}^{M}\Delta G_{nm}\right)\left(1+\sum_{p=1}^{4}\Delta B_{np}\right)}, \quad (4)$$

where

$$\Delta G_{nm} = \begin{cases} \sum_{q=2}^{4}\left|G_{nm,q} - G_{nm,1}\right|; & \Delta G_{nm} > G_{tol} \\ 0 & \Delta G_{nm} \le G_{tol} \end{cases}, \quad (5)$$

$$\Delta B_{np} = \begin{cases} \left|B_{np} - B_{req}\right| \Big/ B_{req} & \Delta B_{np} > B_{tol} \\ 0 & \Delta B_{np} \le B_{tol} \end{cases}. \quad (6)$$

In (5), $G_{nm,q}$ (q = 1~4) indicates one of the four radiation patterns. In particular, $G_{nm,1}$ is selected to the one with beamwidth closest to the specification. The computation of (5) intends to minimize the differences in the four patterns. ΔG_{nm} =0 if the difference between patterns are all smaller than the tolerance threshold. Equation (6) drives the beamwidths of the four patterns close to the required beam width. Similar to the characteristics described in the previous example, a proper design will yield a fitness value of one (F_n = 1). Similar to the previous example, 10 genes are employed in each generation to determine superior parents and each parameter of the antenna structure is represented by 6 bits. These optimization parameters are selected to provide a relatively quick convergence in the GA optimization procedure.

The proposed scheme is performed to optimize the antenna structure for its patterns at both 20 and 30 GHz. Figure 6(b) shows the radiation patterns of the optimized antenna design, which has identical main beam patterns in the two principal planes at both 20 and 30 GHz. In particular, the beam width is 72 degrees as required in the design criterions. Approximately compared with Figure 6(a), the gains at both frequencies are almost identical and are approximately 14 dBi. The values of initial setting and optimized design parameters are shown in Table 2 for comparison, while the performance parameters such as gain, beamwidth, and front-to-back ratio at 20 and 30 GHz are tabulated in Table 3. In this design optimization, each antenna structure costs 20 minutes of CPU time, which is 2 times larger than that in the previous example because now the analysis needs to be performed at 2 frequencies. The whole simulation cost 25.5 hours of CPU time, which comprised 75 HFSS analyses (i.e., 75 antenna structures have been analyzed in the GA procedure).

Table 2: The initial and optimized values of the antenna dimensions for the second example.

Parameter Name	Initial Values (mm)	Optimized Values (mm)
R	2.254	4.9841
B	22.46	24.683
W1	2.4285	2.0476
W2	1.2857	1.8571
W3	2.5873	1.3016
W4	2.0714	1.8809
W5	1.2222	1.5714
W6	1.8881	2.0714
H1	7.3333	6.7619
H2	3.6508	2.619
H3	11.937	10.6984
H4	8.2689	7.1429
H5	14.048	14.2381

Table 3: Comparison of radiation performance of initial setting and optimized designs.

Parameter Name	Initial Setting	Optimized Design
Gain @ 20 GHz	-73 dBi	14 dBi
10 dB beamwidth @ 20 GHz	180 deg.	72 deg.
Front-to-back ratio @ 20 dB	12 dB	30 dB
Gain @ 30 GHz	-75 dBi	14 dBi
10 dB beamwidth @ 30 GHz	150 deg.	72 deg.
Front-to-back ratio @ 30 dB	12 dB	37 dB

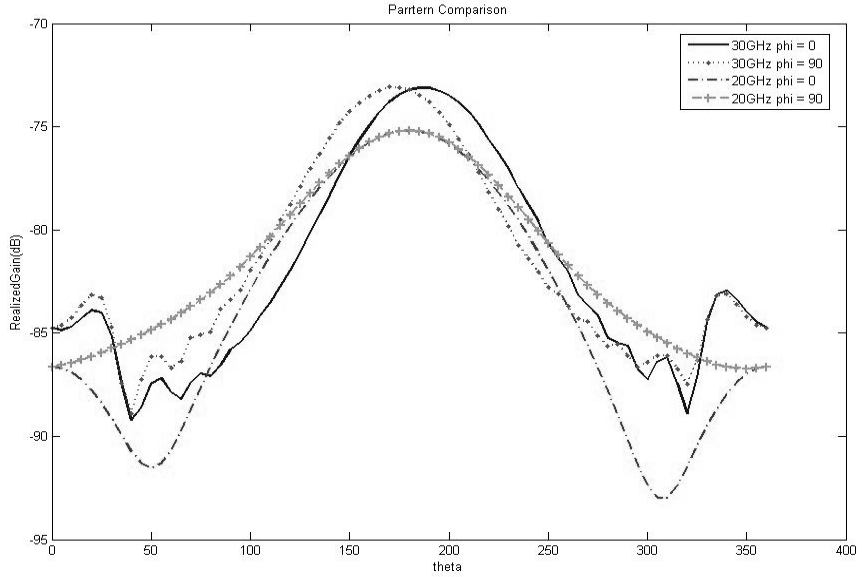

(a)

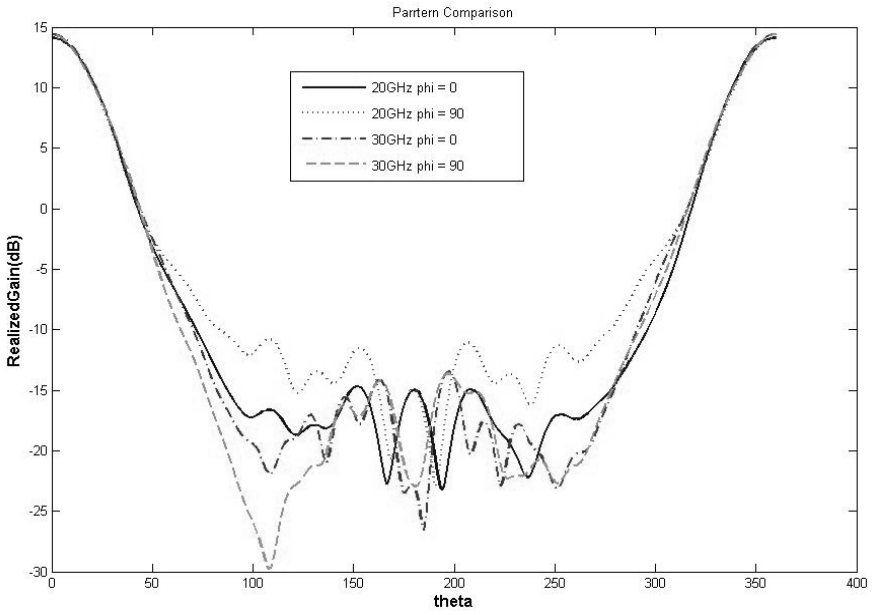

(b)

Fig. 6. The radiation patterns of the horn antenna at the two principal planes, which are operated at 20 and 30 GHz. The desired radiation direction in the initial setting (a) should point to 0 degrees as achieved after optimization in (b).

IV. CONCLUSION

In this work, a GA-based design optimizer and HFSS simulation tools are integrated within an automated control program to optimize the design of horn antennas for the application as feeds to reflector antennas. The validity of this work is verified via the optimization of the radiation patterns of the dual band antennas so that the effective antenna aperture of the reflector can be maximized. The presented examples show that the

optimization can be performed automatically and therefore save tremendous efforts compared to manual tuning.

REFERENCES

[1] O. Yamada, H. Matsumura and M. Sasaki, "Development of Satellite and Terrestrial Digital Broadcasting System in Japan," *IEEE MTT-S International Microwave Symposium Digest*, vol. 1, pp. 71-75, June 7-12, 1998.

[2] E. Lier and R. Landes, "High Gain Linearly Polarized Dual-Band Horn for Multi-feed Reflector Antenna", *Electronic Letters*, vol. 39, no. 17, pp. 1230-1232, Aug. 2003.

[3] C. A. Balanis, *Antenna Theory- Analysis and Design*, Chap. 13, 2nd Ed., John Wiley & Sons, New York, 1997.

[4] J. Kim, T. Yoon, J. Kim and J. Choi, "Design of an ultra wide-band printed monopole antenna using FDTD and genetic algorithm," *Microwave and Wireless Components Letters*, vol. 15, no. 6, pp. 395-397, Jun. 2005.

[5] H.-J. Wang, K.-F. Man, S.-W. Zhang, J. Li and H.-G. Liu, "Large Bandwidth Fourfold-T-shaped Microstrip-fed Slot Antenna Using FDTD and Genetic Algorithm," *Proceeding of ICIT 2005*, pp. 287─290, Dec. 2005.

[6] S. Alfonzetti, G. Borzi, E. Dilettoso and N. Salerno, "Optimization of a Patch Antenna by Genetic Algorithms and a Hybrid FEM/RBCI Method," *Proceeding of 12th Biennial IEEE Conference on Electromagnetic Field Computation*, p. 375, 2006.

[7] X. Chen, K. Huang and X.-B. Xu, "Automated design of a three-dimensional fishbone antenna using parallel genetic algorithm and NEC," *Antennas and Wireless Propagation Letters*, vol. 4, pp. 425-428, 2005.

[8] J. L. Volakis, A. Chatterjee and L. C. Kempel, *Finite Element Method for Electromagnetics-Antennas, Microwave Circuit and Scattering Applications*, IEEE Press, New York, 1998.

[9] Ansoft Corporation, *High Frequency Structure Simulator (HSFF) User Manual*, Pittsburgh, PA, Ansoft Corporation, 2001.

[10] F. Hsu, P.-R. Chang and K.-K. Chan, "Optimization of two-dimensional radome boresight error performance using simulated annealing technique," *IEEE Trans. on Antennas Propagat.*, vol. 41, pp. 1195-1203, Sept. 1993.

[11] J. H. Holland, "Genetic algorithm," *Scientific American*, pp. 44-51, Jul. 1992.

[12] J. M. Johnson, Y. Rahmat-Samii, "Genetic algorithms in engineering electromagnetics," *IEEE Antennas and Propagat. Magazine*, vol. 39, pp. 7-21, Aug. 1997.

[13] T.-H. Lee and R.C. Rudduck, *OSU Reflector Antenna Code- Version 3.0 (NECREF Version 3.0)*, Technical Report 318021-1, ElectroScience Lab., Ohio State University, Feb. 1994.

[14] P. H. Nielsen and S. B. Sorensen, *GRASP9 Software User Manual, version 8.0*, Copenhagen, Denmark, TICRA, 1997.

[15] P.S. Wang, *An Introduction to ANSI C on Unix*, Belmont, CA, Wadsworth, 1992.

Hsi-Tseng Chou was born in Taiwan, in 1966. He received his B.S. degree in electrical engineering from National Taiwan University in 1988, and his M.S. and Ph. D. degrees also in electrical engineering from Ohio State University (OSU) in 1993 and 1996, respectively. He joined Yuan-Ze University (YZU), Taiwan, in August 1998, and is currently a professor in the Department of Communications Engineering.

His research interests include wireless communication network, antenna design, antenna measurement, electromagnetic scattering, asymptotic high frequency techniques such as Uniform Geometrical Theory of Diffraction (UTD), novel Gaussian Beam techniques, and UTD type solution for periodic structures. Dr. Chou has received two awards from Taiwanese Ministry of Education and Ministry of Economic Affairs in 2003 and 2008, respectively to recognize his distinguished contributions in promoting academic researches for industrial applications, which were the highest honors these two ministries have given to university professors to recognize their industrial contributions. He has published more than 250 journal and conference papers.

Dr. Chou is a senior member of IEEE AP-S and an elected member of URSI International Radio Science US commission B.

Chia-Wei Liu was born in Taiwan, in 1983. He received his B.S. degree in communication engineering from Yuan Ze University in 2006. He is currently an M.S. student in the Electroscience Laboratory, Ohio State University. His research interests include EM numerical simulations and antenna designs for wireless communications.

Hsi-Hsir Chou was born in ChangHua Taiwan, in 1975. He received his PhD degree in Engineering from Cambridge University, U.K. in 2008.

He was involved in collaborating with ALPS UK Co. Ltd and Dow Corning Co. Ltd in the development of patented free-space optical interconnection technologies, ferroelectric liquid crystal devices and carbon nanotube dielectric devices during his PhD program at Cambridge University from 2004 to 2008. He joined the Department of Engineering Science, Oxford University, U.K. in July 2008 as a Post-Doctoral Researcher in the development of high-speed visible light communication technologies sponsored by Samsung Electronics Co. Ltd., Korea, before he returned Taiwan to join the Communication Research Center, Yuan Ze University, Taiwan as a Researcher in May, 2009. His current research interests include free-space optical interconnection technologies, ferroelectric liquid crystal devices, carbon nanotube dielectric devices and antenna design.

Dr. Chou is a lifetime member of Trinity College, Cambridge and a Fellow of Cambridge Overseas Society since 2005.

Wen-Jiao Liao was born in Taipei, Taiwan. He received the B.S. degree in electrical engineering from the National Taiwan University, Taipei, Taiwan in 1995. He received the M.S. and Ph.D. degrees in electrical engineering from The Ohio State University, Columbus, in 1999 and 2003, respectively. After receiving his Ph.D. degree in 2003, He was employed by Syntonics, LLC as a project scientist. In 2004, he continued his research work in the Electroscience laboratory of the Ohio State University as a post-doctoral researcher. In 2004-2007, he was an Assistant Professor at Yuan-Ze University in the Department of Communications Engineering. He is currently an Assistant Professor at National Taiwan University of Science and Technology in the Department of Electrical Engineering. His main interests are antenna design and measurement, wave propagation, EMC/EMI issues, electro-optical sensor signatures, and image processing.

Investigation on the Electric Field Inverse Problem of HV Transmission Lines and Discussion on Its Application

Fan Yang [1], Hao Wu[1], Wei He[1], Tao Chen [2]and Duan Nie [3]

[1] State Key Laboratory of Power Transmission Equipment & System Security and New Technology, College of Electrical Engineering, Chongqing University
Chongqing, 400044 China
yangfancqu@gmail.com

[2] Chongqing Electric Power Research Institute, Chongqing 401123, China
chentaocqep@yahoo.cn

[3] Chongqing Power Grid, Chongqing 400014, China
diduancq@yahoo.cn

***Abstract*—**The electric field inverse problem of high voltage transmission lines is investigated in this paper. Firstly the equations for the electric field forward problem of transmission lines were formulated, then equations for the inverse problem were formulated according to the forward problem and the least square theory. A method to solve the inverse problem is presented in the paper, in which the global regularization was used to process the ill-posed characteristic of the inverse problem. The Damped Gauss-Newton iterative method was used to search the optimum solution.

A 500kV double-circuit transmission line was taken as an example for the calculations of the inverse problem. The inverse problems for different situations were calculated, including the situation when the transmission lines were in normal operation, and the situation when the transmission lines were in faulty state. The solutions to the inverse problem with and without regularization were compared in the paper, and the results indicated that the global regularization can effectively eliminate the ill-pose of the inverse problem. The electric field inverse problem can be used to confirm the electrification state of the ultra high voltage transmission lines, and also can be used in the environmental assessment tests to reduce the measurement workload.

***Index Terms*—**Transmission line, electric field, inverse problem, global regularization, Damped Gauss Newton.

I. INTRODUCTION

The electromagnetic field in the vicinity of high-voltage (HV) transmission lines (TLs) were investigated comprehensively in the past two decades, including the measurements on the electric field, magnetic field, audible noise, and the calculations of the electric field and magnetic field produced by TLs [1-3]. For the calculations of the electric field and magnetic field produced by the HV TLs, besides the sizes of the TLs, the electrical parameters of TLs, such as potential, phase angle, should be given, then the electric field at the measuring points can be computed.

A. Forward Problem and Inverse Problem of TL Electric Field

The process in which the electric field is calculated by the given parameters of the source, is usually called the "forward problem". And according to the definition of the "forward problem", the electric field "inverse problem" of TLs is the process to compute the parameters of the source according to the electric field at the measuring points. Using the forward problem of the TLs, we can assess the environmental influence caused by the TLs, and through the calculation of the inverse problem, the parameters of the source can be confirmed.

B. Application of the Electric Field Inverse Problem of TLs

Recently the application of the electric field

inverse problem has arisen more frequently in engineering, such as with the detection of the electrification state of the ultra-high-voltage (UHV) TLs, and the environmental assessment of TLs.

With the increase of installed capacity in China, it's necessary to develop UHV power transmission, ranging from a 750kV voltage rating to 1200kV. According to the safety operation rules, it must be confirmed whether the transmission lines are charged during equipment maintenances, which needs electroscopes for different voltage rating [9, 10]. With the increase of voltage rating, distance between transmission lines and ground grows. For instance, when the height of transmission lines of 750kV voltage rating may exceed 30m, it's not convenient to adopt the traditional insulating stick or insulating rope to detect electrification state any more. Using the electric field inverse problem in this paper, the potential and phase angle of the transmission lines can be calculated according to the measured electric field strength at the measuring points, then the electrification state of the TL can be confirmed.

In addition, assessments on the electromagnetic environment around the HV TLs have been carried out around the world. In the environmental assessment on the TLs, the electric and magnetic strength of a large number of points should be measured, which means a huge workload. In order to reduce the workload in the environmental assessment tests, the electric field inverse problem of the TLs can be used. That is, according to the measured electric field strength at some measuring points near the ground, the parameters of the field source can be calculated by solving the inverse problem, then with the obtained parameters of the TLs, the real electric field distribution around the transmission lines can be calculated. Hence some measurement workload can be avoided by using the inverse problem.

Therefore the solution to the electric field inverse problem of TLs is significant for the application of the electric field inverse problem.

And in the remaining parts of the paper the method to solve the inverse problem will be presented, which are organized as follows: Section II presents the way to set up the model of the inverse problem for the 500kV double-circuit TLs. The method to solve the inverse problem is described in Section III. Due to the ill-posed characteristic and the ill-conditioning characteristic of the solution to the inverse problem, the global regularization is used to deal with the ill-posed characteristic caused by the interference and errors. Damped Gauss-Newton (DGN) method is used to search the optimum solution to the inverse problem. Section IV shows some computational examples, and results indicate that the global regularization can effectively eliminate the ill-posed characteristic. Applications of the inverse problem for the electric field of TL in the practical engineering are presented in Section IV. Finally concluding remarks will be given in Section V.

II. MODEL AND EQUATION FOR THE ELECTRIC FIELD INVERSE PROBLEM OF TRANSMISSION LINE

A. Model Setup

A 500kV double-circuit three-phase TL was taken as an example. The cross section and the distribution of the measuring points are shown in Fig. 1. The parameters in the model are as follows: D_1=4.5m, D_2=5.5m, D_3=11.5m, H_1=11m, H_2=18m. H_3 is the distance between the measuring points and the ground, and H_3=1.8m. The equivalent radius (R') of the four-bundle conductor is 0.323m, the radius (r) of the sub-conductor is 0.0148m, and the radius of lightning conductor (R'_L) is 0.0054m. In the computation, the influence from the conductor sag was ignored.

B. Equation for the Electric Field Forward Problem

The forward problem is the process to compute the electric field at the measuring points according to the potential and phase angle of the TL. The charge simulation method (CSM) is the most frequently used method according to the characteristics of the electric field around the TL [1-3].

According to the principle of CSM, line simulation charges were used to simulate the free charge in the TLs and lightning lines. And the simulation charge was located at the center of the conductor and lightning conductor, and each conductor was simulated with one line simulation charge. Set the count of the simulation charges as M, for the model shown in Fig. 1 M = 8. Set the count of matching points in the model as N, hence M=N. According to the Maxwell equations, the

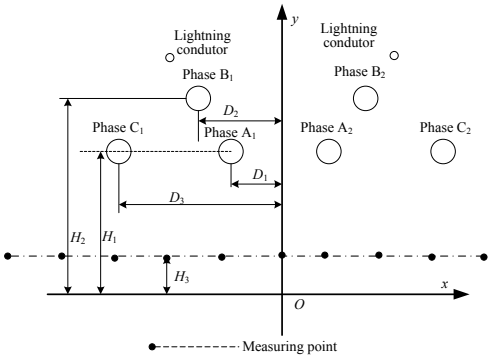

Fig. 1. Schematic diagram of cross section of the 500KV double-circuit three-phase transmission line.

size of the simulation charges could be obtained according to (1), then the electric field at any measuring point could be computed according to (2).

$$[p][Q]=[\varphi] \tag{1}$$

$$\begin{aligned}[f_x][Q]&=[E_x]\\ [f_y][Q]&=[E_y]\\ [f_z][Q]&=[E_z]\\ [E]&=\sqrt{E_x^2+E_y^2+E_z^2}\end{aligned} \tag{2}$$

where $[p]$ is the potential coefficient between the simulation charges and matching points. $[Q]$ is the size of the simulation charges, and $[\varphi]$ is the potential at the matching points. $[f_x]$, $[f_y]$, $[f_z]$ are the electric field strength coefficient between the simulation charges and measuring points along x, y, z axis respectively. $[E_x]$, $[E_y]$, $[E_z]$ are the corresponding electric field strength, and $[E]$ is the total electric field strength at the measuring points.

C. Equation for the Electric Field Inverse Problem

The inverse problem is the process to calculate the potential and phase angle of the TLs according to the electric field at the measuring points.

Similar to the calculation of the electric field forward problem of the TLs, the CSM was used and the size of the simulation charges was computed first. However, different from the calculation of the forward problem, the size of the simulation charges was computed according to (2) in the inverse problem, instead of (1) used in the forward problem.

Hence anew problem rises up. For equation (2), we can not find its solution directly, so the equation described by (2) must be converted. The least squares theory has been proved to be an effective way to solve question similar with (2) [4, 5], then the solution to the inverse problem can be converted into an extreme value problem. Suppose the nonlinear operator of the forward problem is $F(q)$, here q is the size of the simulation charges, and then the nonlinear inverse problem described by (2) can be rewritten as follows:

$$E=F(q). \tag{3}$$

The corresponding least square equation is as follows:

$$\min_q \left\|E-F(q)\right\|^2 \tag{4}$$

where E is the measured electric field strength at the measuring points. For the model shown in Fig. 1, the count of the simulation charges is 8 (M=8), and the count of the measuring points is usually confirmed according to the engineering requirements.

To compute the real potential and phase angle of the TL using the electric field inverse problem, the more measuring points are set, the more real information of the TL can be obtained. Therefore the count of measuring points N is often larger than M for the model shown in Fig. 1. So (1) is a nonlinear over-determined equation.

III. SOLUTION TO THE ELECTRIC FIELD INVERSE PROBLEM

A. Least Square Solution to the Nonlinear Inverse Problem

For the nonlinear least squares problem shown in (3), the piece-wise linearization iterative algorithm can be used [6, 7]. In order to realize the approximation of the nonlinear operator F, it is necessary to consider the Taylor expansion of $F(q+\delta q)$ at q:

$$\begin{aligned}F(q+\delta q)=F(q)+\frac{\partial F}{\partial q}\delta q+\frac{1}{2}\left(\frac{\partial^2 F}{\partial q^2}\right)(\delta q)^2\\ +R(q,\delta q)\end{aligned}, \tag{5}$$

where $R(q, \delta q)$ is a remainder term. When $\left\|\delta q\right\|$ is small enough, as to the right side of equation (5), the high-order terms can be ignored and the right side can be approximated with the first approximation, then

$$F(q+\delta q)\approx F(q)+\frac{\partial F}{\partial q}\delta q. \tag{6}$$

Therefore, the linear relationship between $\delta E = F(q+\delta q)-F(q)$ and δq can be obtained as follows:

$$\delta E \approx \frac{\partial F}{\partial q}\delta q \ . \qquad (7)$$

Suppose $q^*=q+\delta q$ is the exact solution to equation (3). That is, $F(q^*)=E$, here E is the electric field strength at the measuring points. Then, at point q close to q^*, according to equation (6), the linear operator equation about δq can be obtained as follows:

$$E - F(q) \approx \frac{\partial F}{\partial q}\delta q \, . \qquad (8)$$

The linear operator equation (6) constitutes the basis of the Newton-type iterative solution method of the nonlinear equations.

For the least squares problem shown as equation (4), if q is the optimum solution, the necessary condition is that the gradient of q ($g(q)$) at q is zero. Suppose the objective function for (1) is Φ, that is, $\Phi=\left\| E-F(q) \right\|^2$. Then, the following can be reformulated:

$$\begin{aligned} g(q) = \nabla\phi &= [F(q)-E]\frac{\partial F(q)}{\partial q} \\ &= J^T(q)[F(q)-E] = 0 \end{aligned} \ , \qquad (9)$$

where J is the Jacobean matrix corresponding to $[F(q)-E]$.

Equation (9) is the normal equation of the nonlinear least square problem. Therefore, the solution to the nonlinear least square problem can be transferred into the solution to the normal equation. But the normal equation is still a nonlinear equation. In order to resolve this problem, the Hessian matrix can be also introduced here [7].

B. Global Regularization and Damped Gauss-Newton Method

The electric field inverse problem of TLs is the process to compute the potential and phase angle according to the electric field at the measuring points. Because the electric field at the measuring points is the measured value, interference maybe comes up, which will result in a wrong solution to the inverse problem; this is the so-called ill-posed characteristic of the solution to the inverse problem. To reduce the ill-posed of the inverse problem, regularization is frequently used in the solution to the inverse problem.

The linear equations (9) obtained from the linearization of the nonlinear equation will inherit the ill-conditioning characteristic of the original equation, so it is necessary to introduce the regularization. Regularizing the linear equation $E - F(q^{(k)}) \approx \frac{\partial F}{\partial q^{(k)}}\delta q$ corresponding to equation (8), then the following optimization problem can be obtained.

$$\min\left\{ \left\| E - F(q^{(k)}) - \frac{\partial F}{\partial q^{(k)}}\delta q \right\|^2 + \alpha \left\| W(\delta q) \right\|^2 \right\} \ , \qquad (10)$$

where W is a linear operator. If $W=I$, the regularization will be imposed on δq. This is the "crawling method", and it has the following disadvantages: 1) it can not control the characteristics of all the solutions. Because the regularization is imposed on δq, rather than q. 2) The solution q^* depends on the initial solution $q(0)$ and the minimum path $\delta q(k)$, k=1, 2, …, N, where N is the iterative times. 3) If different methods are used to calculate the value of $\delta q(k)$, different q^* will be obtained.

In order to overcome the disadvantages of the "crawling method", in this paper, the following global regularization was adopted.

$$\min\left\{ \left\| E - F(q^{(k)}) - \frac{\partial F}{\partial q^{(k)}}\delta q \right\|^2 + \alpha \left\| W(q^{(k)} + \delta q) \right\|^2 \right\} . \qquad (11)$$

In the so-called global regularization, the regularization is imposed on q, so the obtained step size may not be small. It is actually the linearization of the following optimization problem.

$$\min\left\{ \left\| E - F(q) \right\|^2 + \alpha \left\| W(q) \right\|^2 \right\} . \qquad (12)$$

Equation (12) is the regularization of the original nonlinear inverse problem.

C. Damped Gauss-Newton Iterative Method

To ensure the objective function value for (12) diminish in the next iteration, the Damped Gauss-Newton iterative method was used in this paper. In the DGN, the δq is replaced with $\omega\delta q$ ($0.1<\omega<0.5$) to make the δq small enough, which make the objective function value for (12) diminish in the next iteration.

To ensure the objective function value for (12) diminish in the next iteration, the Damped Gauss-

Newton (DGN) iterative method was used in this paper. In the DGN, the δq is replaced with $\omega\delta q$ ($0.1<\omega<0.5$) to make the δq small enough, which make the objective function value for (12) diminish in the next iteration.

IV. CALCULATION EXAMPLES

To verify the validation of the method presented in the method, model shown in Fig. 1 was taken as an example. To get more real information of the TL, 11 points are laid out along a horizontal line with a height of 1.8m from the ground as shown in Fig.1. The distance between two adjacent measuring points is 5m.

For the solution to the electric field inverse problem of the TL, the measured electric field strength at the 11 measuring points, which may contain interference, should be given first. To verify the validation of the method proposed in this paper, a set of simulated measured electric field strength at the measuring points was offered in the following way. Firstly according to the computation method of the forward problem, the electric field strength at all the measuring points was calculated with the parameters when the TLs were in normal condition, which could be taken as the standard value of the electric field strength at the measuring points. Add a random error data with ±10% (Note: the errors of the symmetric points are equal) to the standard values of the electric field strength at all the measuring points, and the sum could be taken as the simulated measured values of the electric field strength.

Calculations on the electric field inverse problem of the TL at different situation were carried out in the paper, such as the TLs were in normal operation, or in faulty state respectively.

Table 1. Solution without regularization.

Conductor	A_1	B_1	C_1	A_2	B_2	C_2
Potential (10^5V/m)	2.516	2.449	1.593	1.121	2.494	3.024
Phase angle	116.3	186.1	242.1	31.9	83.0	237.6

Table 2. Solution with regularization.

Conductor	A_1	B_1	C_1	A_2	B_2	C_2
Potential (10^5V/m)	3.016	3.037	3.031	2.997	3.042	3.023
Phase angle	0.7	121.0	240.0	0	120.2	239.7

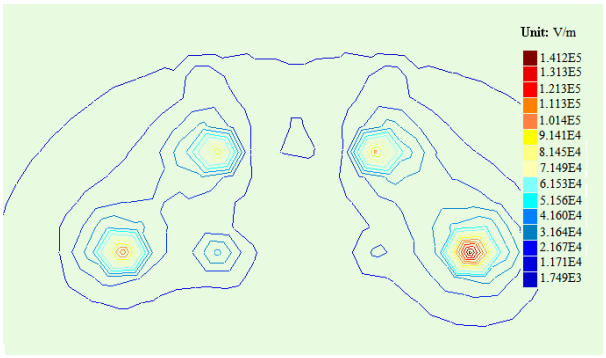

(a)

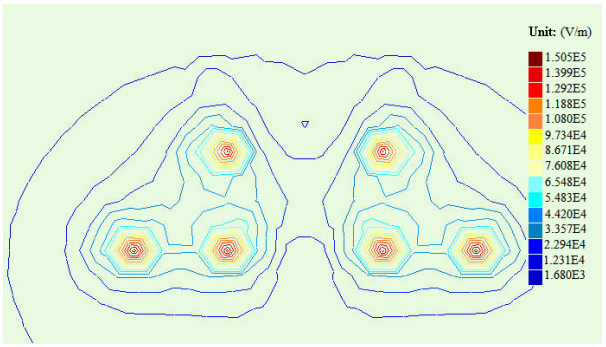

(b)

Fig. 2. Electric field distribution in the vicinity of 500kV double-circuit TLs for normal operation situation, (a) Without regularization, (b) With regularization.

A. Calculation for Normal Operation

When the TL shown in Fig. 1 was in normal operation, the parameters of the TL were as follows: phase potential was 303kV, and the phase angle from A1 to C1 was 0º, 120º, 240º. Hence the simulated electric field strengths at the 11 measuring points were as follows: 2.680 kV/m, 4.718 kV/m, 7.214 kV/m, 7.250 kV/m, 8.954 kV/m, 10.706 kV/m, 8.954 kV/m, 7.250 kV/m, 7.214 kV/m , 4.718 kV/m, 2.680 kV/m. As to the lightning conductor, both the boundary potential and phase were zero.

Table 1 and Fig. 2 (a) are the computational results when the global regularization was not adopted. Table 2 and Fig. 2 (b) are the computational results when the global regularization was adopted. It can be seen from Table 1 and 2 that, when the regularization was not used, the deviations of the computational results are relatively large, which indicate that the

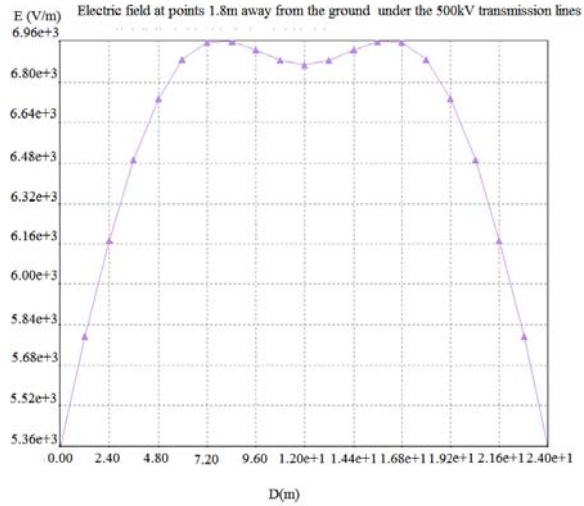

(a)

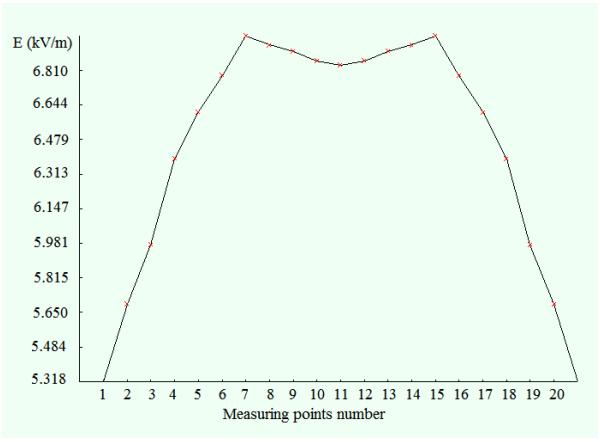

(b)

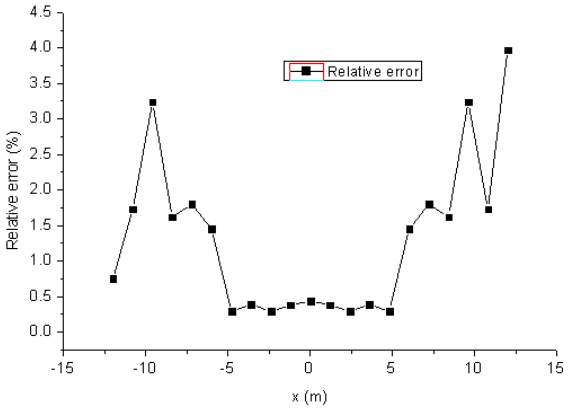

(c)

Fig. 3. Comparison between the results obtained by (a) the IES-Electro, (b) the inverse problem, and (c) the relative error.

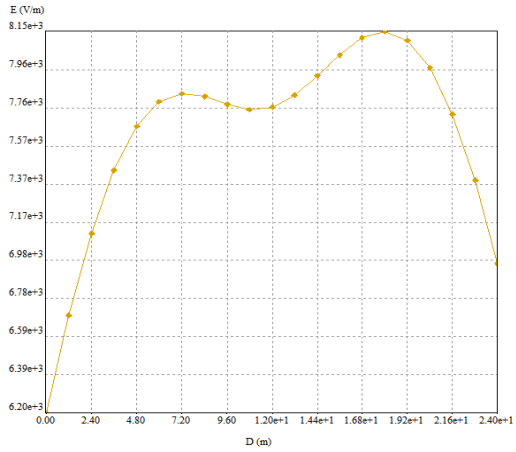

(a)

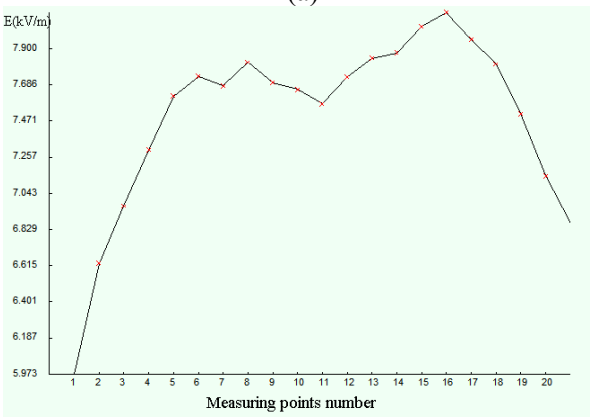

(b)

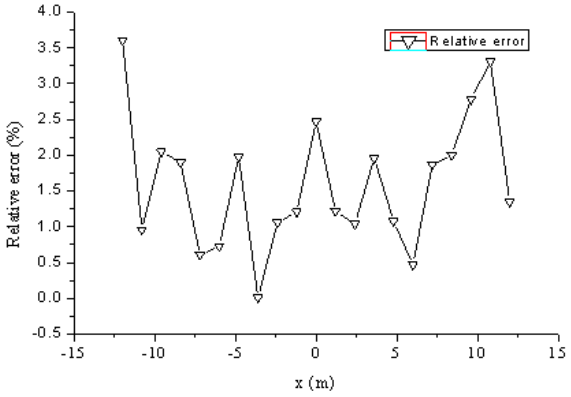

(c)

Fig. 4. Electric field at measuring points obtained by (a) IES-Electro, (b) the inverse problem, and (c) the relative error.

global regularization can effectively eliminate the influence caused by the interference in the measurement.

In order to verify the accuracy of the method used to solve the inverse problem, further calculations were carried out. In the model shown

in Fig. 1, along the horizontal line with a height of 1.8m from the ground, 21 points from left to right are selected for computation. The distance between two adjacent measuring points is 1.2m. The electric field strength at the 21 measuring points was computed respectively with the IES-Electro software and the inverse problem method proposed in this paper, the IES-Electro software is a BEM based software [8]. Fig. 3 shows the comparison between the results obtained by method in this paper and IES-Electro. It can be seen from the computation results that the maximum relative error is 3.97%, which is within the allowed error range. Hence the accuracy of the method to solve the electric field inverse problem of the TL was verified.

B. Calculation for Faulty State

Suppose that line of phase C1 was in phase anomaly state, of which the phase angle was 120º, and the line of phase B1 was short-circuit. Hence the simulated measured electric field strength at the 11 measuring points was computed, and the following was its value: 3.724 kV/m, 6.004 kV/m, 8.726 kV/m, 9.182 kV/m,10.475 kV/m, 11.556 kV/m, 9.313 kV/m, 7.263 kV/m, 7.186 kV/m, 4.684 kV/m, and 2.62 kV/m.

In order to better verify the accuracy of the solution to the inverse problem, the electric field strength at the 21 measuring points were computed with the IES-Electro and method in this paper respectively, and the computation results are shown in Fig. 4, including the actual electric field strength and the relative error. It can be seen from the computational results that the maximum relative error is 3.61%, which is within the allowed error range. Hence when the TLs were not in normal operation state, the method in the paper is still can solve the inverse problem correctly.

V. CONCLUSIONS

The electric field inverse problem of transmission lines was investigated in this paper. First the equations for the electric field forward problem were formulated, and equations for the inverse problem were formulated according to the forward problem and the least square theory. A method to solve the inverse problem was presented in the paper, in which the global regularization was used to process the ill-posed characteristic of solution to the inverse problem. And the DGN iterative method was used to search the optimum solution.

A 500kV double-circuit transmission line was taken as an example for the calculation of the inverse problem. The inverse problems for different situations were calculated, including the situation when the transmission lines were in normal operation, and the situation when the transmission lines were in faulty state. Solutions to the inverse problem with regularization and without regularization were compared, and results indicate that the global regularization can effectively eliminate the ill-pose of the inverse problem.

Application of the electric field inverse problem was discussed in the paper. It could be used to confirm the electrification state of the UHV TLs, and also could be used in the environmental assessment tests to reduce the measurement workload.

ACKNOWLEDGEMENT

This study is supported by National ‘111’ project (B08036), the State Key Laboratory project (2007DA10512709102) and the National College Students Innovation project (091061106). The authors wish to acknowledge the support provided by the Chinese NSF and Chongqing Science & Technology Commission.

REFERENCES

[1] B. Florkowska, A. Jackowicz-Korczynski, and M. Timler, “Analysis of electric field distribution around the high-voltage overhead transmission lines with an ADSS fiber-optic cable”, *IEEE Transactions on Power Delivery*, vol.19, no.3, pp. 1183-1189, 2004.

[2] Y. Liu, L.E. Zaffanella, “Calculation of electric field and audible noise from transmission lines with non-parallel conductors”, *IEEE Transactions on Power Delivery*, vol.11, no.3, pp. 1492-1497, 1996.

[3] D. Lee, K.-Y. Shin, and S.-D. Lee, “Technique to decrease the electric field intensity on conductor surface using the asymmetrical-sized conductor bundle”, *IEEE/PES Transmission and Distribution Conference*, vol. 4, pp. 1-6, 2008.

[4] E. Coccorese, R. Martone, and F.C. Morabito, “A neural network approach for the solution of electric and magnetic inverse problems”,

IEEE Transactions on Magnetics, vol. 30, no. 5, pp. 2829-2839, 1994.

[5] M.A. Hussain, B. Noble, and B. Becker, "Computer simulation of an inverse problem for electric current computed tomography using a uniform triangular discretization", *The Annual International Conference of the IEEE Engineering in Engineering in Medicine and Biology Society*, pp. 448-450, 1989.

[6] M. Trlep, A. Hamler, B. Hribernik, "The use of DRM for inverse problems of Poisson's equation", *IEEE Translations On Magnetics*, vol.36, no.4, pp. 1649-1652, 2000.

[7] H. Kama, and Z. Xiang, *The inverse problem in Electromagnetic field and its application,* The Science Press, 2005.

[8] http://www.integratedsoft.com/

[9] IEEE Standard 1127-1990, "IEEE guide for the design, construction, and operation of safe and reliable substations for environmental acceptance".

Fan Yang is with the College of Electrical Engineering, Chongqing University. His main research field is regarding the numerical calculation of electromagnetic fields and applications in power systems. He received his Ph.D degree of electrical engineering from Chongqing University in 2008.

Hao Wu is studying for her Bachelor's degree in the College of Electrical Engineering, Chongqing University. Her main interests include the design of algorithms and programming.

Wei He is with the College of Electrical Engineering, Chongqing University. His main research field is regarding the electromagnetic field compatibility and fault detection of electric apparatuses.

Tao Chen is with the Chongqing Electric Power Research Institute. Her main research field is regarding the electromagnetic field compatibility of power systems. She received her Ph.D degree in 2006 at Chongqing University.

Duan Nie is with the Chongqing Power Grid. Her interests include the fault detection of high-voltage equipments.

Modified Double-Ridged Antenna for 2-18 GHz

Alireza Mallahzadeh and Ali Imani

Faculty of Engineering, Shahed University, Tehran, Iran
mallahzadeh@shahed.ac.ir , imani@shahed.ac.ir

***Abstract*—** In this paper, the design and simulation of a modified double-ridged antenna for 2-18 GHz is presented. The designed antenna has a voltage standing wave ratio (VSWR) less than 2.4 for the frequency range of 2-18 GHz and is most suitable as a feed element in the reflectors of the radar systems and EMC applications. The proposed antenna had distortion in radiation patterns in the 10-14 GHz frequency range. This problem has been modified by shaping of ridges. The proposed antenna is simulated with commercially available packages such as CST microwave studio and Ansoft HFSS in the operating frequency range. Simulation results for the VSWR, radiation patterns, and gain of the designed antenna over the frequency band 2-18 GHz are presented and discussed.

***Index Terms*—** Horn antenna, Waveguide, Double-ridged Waveguide, VSWR, Polarization.

I. INTRODUCTION

Broad band, ultra wide band and high gain antennas are one of the most important devices for microwave and millimeter wave applications, electromagnetic compatibility testing, and standard measurements [1–9]. The proposed antenna is similar to horn antennas.

Conventional horn antennas have a limited bandwidth. To extend the maximum practical bandwidth of these antennas, ridges are introduced in the flare section of the antenna. The idea of using ridges in waveguides was adopted in horn by Walton and Sundberg [10], and completed by Kerr in early 1970 when they suggested the use of a feed horn launcher whose dimensions were found experimentally [11]. This is commonly done in waveguides to increase the cutoff frequency of the second propagating mode (TE11) and thus expands the single-mode range before higher order modes occur [12-14]. In [15-16], an E-plane sectoral horn for broadband application using a double-ridge is provided.

A detailed investigation on 1–18 GHz broad-band pyramidal double-ridge horn (DRH) antenna was reported in [17]. As indicated in that paper there is some deterioration in the radiation pattern at higher frequencies. In [18], a broadband electromagnetic compatibility pyramidal DRH antenna for 1 to 14 GHz was reported by Botello, Aguilar and Ruiz. An improved design of the double-ridged pyramidal horn antenna was presented in [19]. Another design of the double-ridged pyramidal horn antenna in the 1–18 GHz frequency range with redesigned feeding section was presented in [20] where several modifications were made in the structure of a conventional double-ridged guide horn antenna.

The distortion of radiation patterns of higher frequencies, cross polarization, the back lobe, and side lobe level (SLL) are the significant disadvantages of the conventional double-ridged horn antenna. Based on the papers available in open literature, VSWR, cross polarization, side lobe level of double-ridged pyramidal horn antennas need to be improved [20].

In this paper, based on the double-ridged rectangular waveguide, a double-ridged antenna including a 50 Ω coaxial feed input is proposed. Accordingly, a waveguide transition structure for the single-mode, the TE10 mode, with low return loss performance is presented. It can be shown that the radiation pattern at higher frequencies, 10–14 GHz would deteriorate over the broadside direction. To overcome this problem, shaping of ridges is introduced leading to a better radiation pattern over the broadside direction. The proposed antenna is simulated with commercially available packages such as Ansoft HFSS which is based on the finite element method and CST microwave studio which is based on the finite integral technique. Simulation results for the VSWR, gain, and radiation patterns of the designed antenna at various frequencies are presented.

II. DESCRIPTION OF THE ANTENNA CONFIGURATION

Figure 1 shows the configuration of the proposed antenna. The overall length of the designed antenna and the distance between tow exponential taper in aperture are 105 mm and 80 mm, respectively. This antenna is divided into three parts: a double-ridged rectangular waveguide, a cavity back, and the exponential tapered part. In the next sections design details for each part will be described.

A. Double-Ridged Rectangular Waveguide Design

The double-ridged rectangular waveguide and a cavity back are the two main parts of the coax to waveguide transition. For single-mode operation, an increase of the bandwidth between the TE10 and the TE11 modes and an impedance match to the impedance of coaxial cable (50Ω) can be obtained by loading ridges with a very small gap. In the first step, as shown in Fig. 2, a two-port rectangular waveguide without coaxial probe for single-mode (i.e., TE10 mode) operates in the frequency range 2–18 GHz is simulated with Ansoft HFSS. The height and width of the designed ridges and distance between the ridges are h=12.2mm, w=2.5 mm, and s=0.6 mm, respectively which are loaded in a rectangular waveguide as shown in Fig. 1.

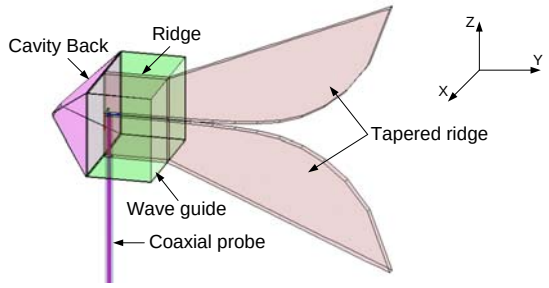

Fig. 1. Configuration of the proposed antenna.

The dimensions and overall length of the rectangular waveguide are a=40 mm, b=25 mm and l=20 mm, respectively. The S12 parameters of the TE10 and TE11 modes in the waveguide versus the frequency are presented in Fig. 3. It can be seen that the lowest mode (i.e., TE10) is the fundamental propagation mode in the waveguide. In Fig. 3, we observe that higher order modes (e.g., TE11) cannot propagate in the waveguide because the S12 parameter is much lower than 0 dB. The characteristic impedance of the fundamental propagation mode (i.e., TE10) versus frequency is presented in Fig. 4. It is obvious from this figure that the characteristic impedance varies between 49.5 Ω and 60 Ω. Therefore, we have very good impedance matching between the coaxial line and double-ridged rectangular waveguide for single-mode operation over the entire frequency band of 2–18 GHz.

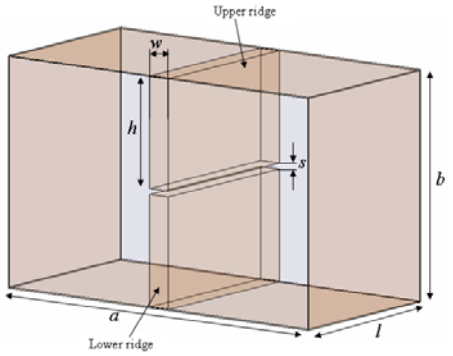

Fig. 2. Two port double-ridged rectangular waveguide without coaxial probe.

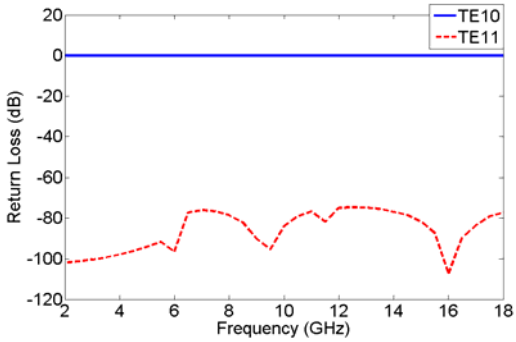

Fig. 3. S12 parameter of the propagation mode (TE10) and non propagation mode (TE11) versus frequency.

B. Coaxial to Double-Ridged Rectangular Waveguide Transition

It is necessary to use a transition between the coaxial probe and the double-ridged rectangular waveguide. The transition between the coaxial probe and the double-ridged waveguide is important to the return loss performance of the antenna. The principal goal is obtaining low levels of VSWR throughout the transformation of the TEM- mode in the coaxial section to the TE-mode in the waveguide. In order to achieve low VSWR, the cavity back length and probe spacing from the ridged edge should be optimized. Numerous

simulations have been made to optimize the transitional performance using Ansoft HFSS. In our simulations we assumed that the double-ridged rectangular waveguide absorbs the full wave that is propagated from the coaxial probe.

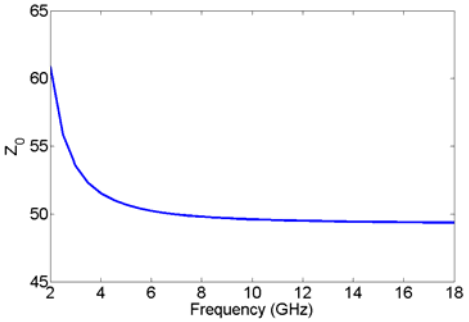

Fig. 4. Characteristic impedance of the fundamental propagation mode (TE10) versus frequency.

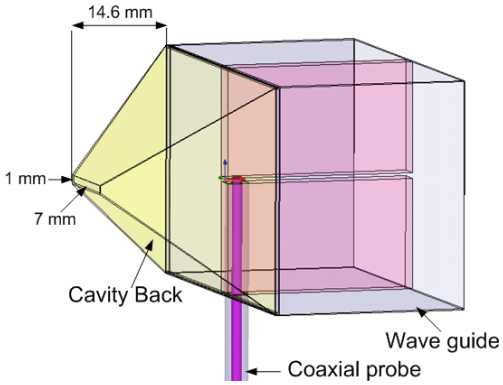

Fig. 5. Cavity back for return loss improvement in the waveguide transition.

It is very common to use a cavity back to obtain a much lower return loss in coaxial to double-ridged waveguide transitions. It was found that the VSWR of the antenna is critically dependent on the shape and dimensions of the cavity back. We consider a conical shaped cavity. The cavity dimensions which are obtained using the optimization method are shown in Fig. 5.

C. Exponential Tapered Part Design

The design of the exponential tapered part is the most significant part in the antenna design. The exponential tapered part varies the impedance of the guide from 50 Ω at the feeding point (double-ridged rectangular waveguide) to 377 Ω at the aperture of the antenna [6]. The impedance variation in the tapered part is as (1):

$$Z(y) = z_0 e^{ky} \quad , \quad (0 \le y \le L) \qquad (1)$$

where y is the distance from the waveguide aperture and L is the axial length (with L=70 mm) of the antenna opening (exponential tapered part). The k is calculated as follow [17]:

$$k = \frac{1}{L}\ln\left(\frac{Z_L}{Z_0}\right) \qquad (2)$$

in which Z_0 and Z_L are the characteristic impedances of double-ridged rectangular waveguide and free space, respectively. In order to synthesize the exponential tapered part, the following algorithm is proposed:

Table 1: The detailed design dimensions of the flare section.

Waveguide number	Length of the wave-guide aperture (mm)	Character-istic impedance (Ω)	Height of the tap-ered ridge (mm)
1	12.5	50	12.2
2	15.25	61.2	14.86
3	18	74.9	17.4
4	20.75	91.6	19.86
5	23.5	112.2	22.07
6	26.25	137.3	23.8
7	29	168	24.5
8	31.75	205.6	23.65
9	34.5	251.7	21
10	37.25	308	15.2

The axial length of the antenna opening (L) is divided into ten sections, which results in 10 smaller double-ridged rectangular waveguides. Each corresponding aperture size is obtained from the main horn antenna structure. Then, the height of each double-ridged rectangular waveguides should be optimized (by Ansoft HFSS) in such a way that the corresponding characteristic impedance is equal to (1). The detailed design dimensions of the exponential tapered part are shown in Table 1. After obtaining the height of the exponential tapered part we connect them together. The final shape appears as an exponential taper and is shown in Fig. 6. We can see that at first, the height of the section increases and then decreases.

III. SIMULATION RESULTS

In this section simulation results of the proposed antenna are presented. To emphasize on validity of the simulated results, two commercially available software packages, the HFSS and CST have been used. Both show very close results confirming that the simulated results are reasonably accurate. The VSWR of the designed antenna is presented in Fig. 7. As shown, the maximum value of the VSWR is less than 2.4 over the operating band of 2 to 18 GHz.

Fig. 8 shows co- and cross polar far-field radiation patterns in Y-Z plane for various frequencies (2, 7, 12, 18 GHz). It can be seen that the designed antenna exhibits low cross polarization in the entire operating bandwidth. Unfortunately, the proposed antenna has distortion in radiation patterns at higher frequencies (10-14 GHz). A new technique employed to improve this problem.

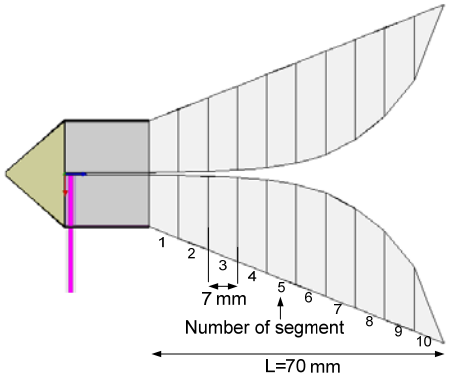

Fig. 6. The proposed antenna made from ten smaller waveguides each of different height (cut view).

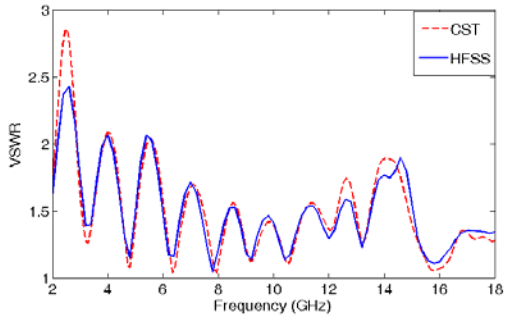

Fig. 7. Simulated VSWR of the designed antenna.

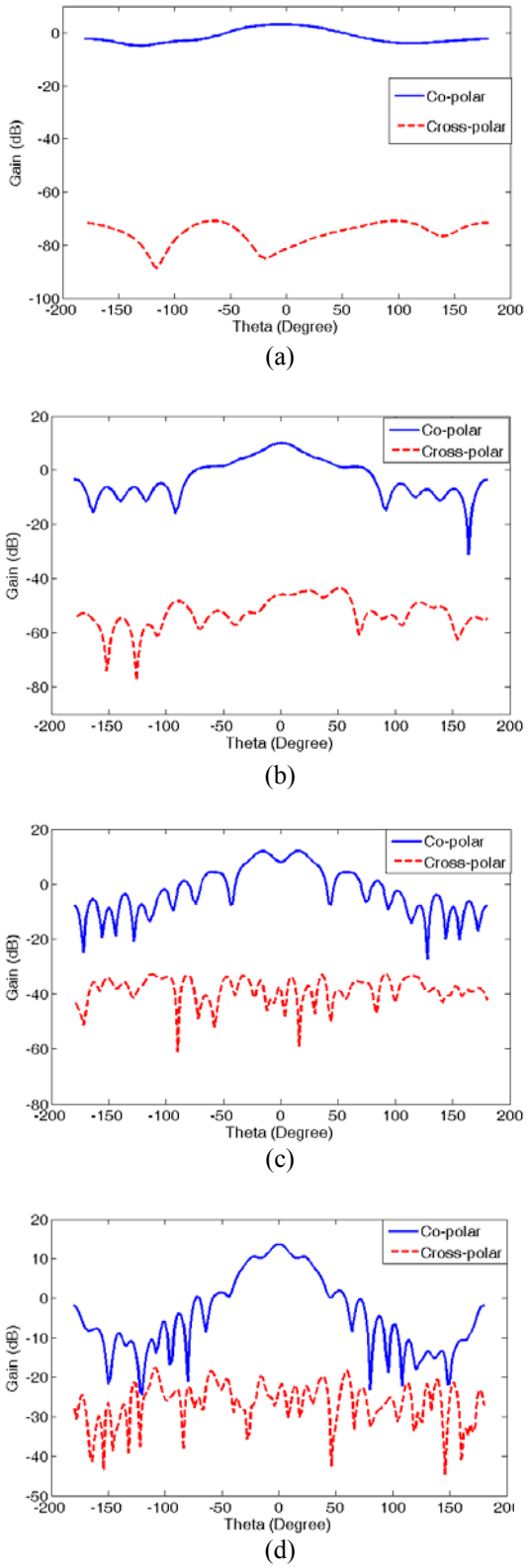

Fig. 8. Simulated radiation patterns of antenna at: (a) 2 GHz, (b) 7 GHz, (c) 12 GHz, and (d) 18 GHz.

IV. MODIFIED DESIGN OF THE PROPOSED ANTENNA

Radiation patterns of the proposed antenna at higher frequencies (10-14 GHz) deteriorate. This can be due to the field distribution over the aperture plane that has a destructive effect in the far field at the broadside direction. To overcome this by new technique a pair of added ridges were placed on the end and top of the exponential tapered part. The modified antenna is shown in Fig. 9. In order to achieve good radiation pattern, the dimensions of the added ridge should be optimized. Simulations show that this structure changes the dispensation of the fields over the antenna aperture that cause destroyer effects of them in the 10-14 GHz exterminate and hence we have a well-shaped main beam over the frequency range of 2–18 GHz. The corresponding VSWR of the modified antenna is shown in Fig. 10.

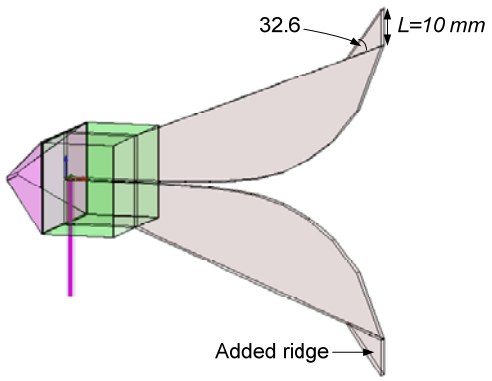

Fig. 9. Configuration of the modified proposed antenna.

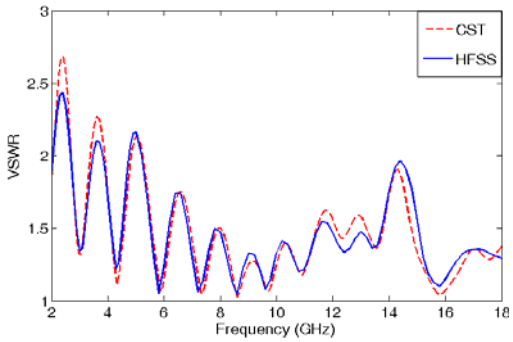

Fig. 10. Simulated VSWR of the modified proposed antenna.

The radiation patterns of the modified antenna are shown in Figs. 11 for the frequencies 2, 7, 12, 18 GHz. The gain of the proposed antenna versus frequency is shown in Fig. 12. It can be seen that the gain of the antenna increases as frequency increases. The maximum value of gain occurs at the end of the operating frequency band (18 GHz).

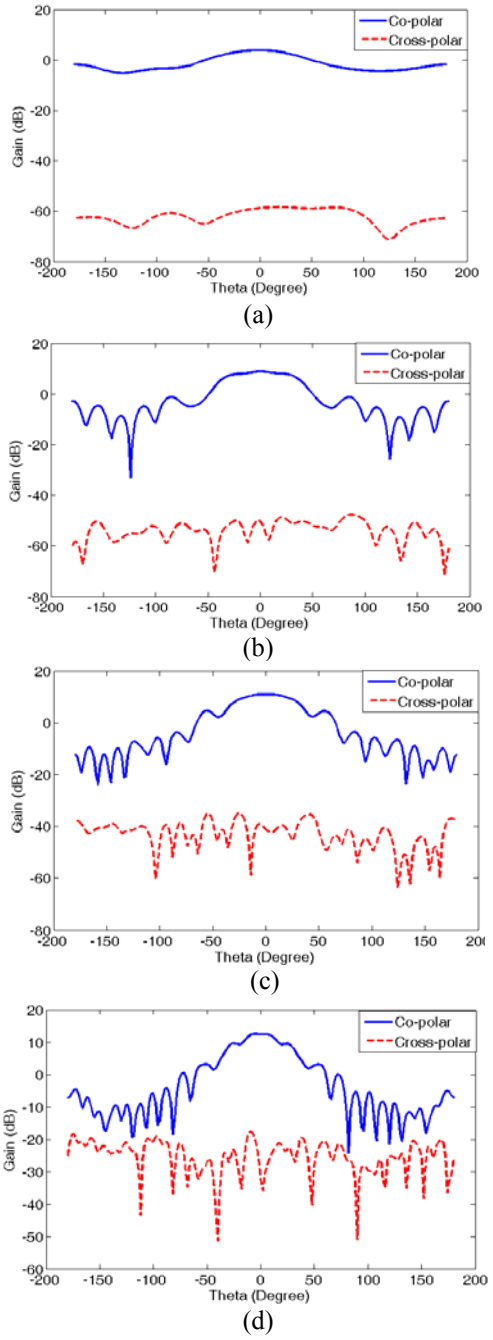

Fig. 11. Simulated radiation patterns of the modified proposed antenna at: (a) 2 GHz, (b) 7 GHz, (c) 12 GHz, (d) 18 GHz.

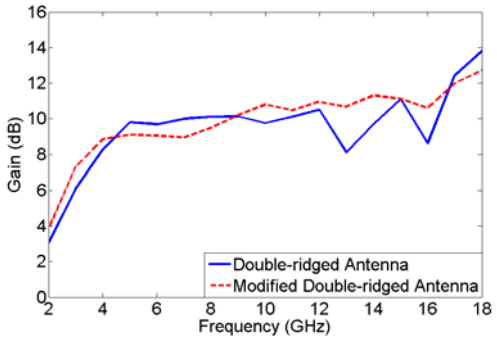

Fig. 12. Gain versus frequency for the proposed antenna.

V. CONCLUSION

In this paper, a modified double-ridged antenna has been proposed for the 2-18 GHz band. Ansoft HFSS and CST software were used for analysis of the designed antenna. Compared to conventional double-ridged horn antennas with rectangular apertures, the designed antenna (with lower size of aperture) has lower weight, and low cross polarization. Incidentally, fabrication of the proposed antenna is easier than for double-ridged horn antennas. The distortion of the radiation patterns at higher frequencies is the significant disadvantage of the conventional broadband double-ridged pyramidal horn antenna. Our proposed antenna doesn't show the above mentioned disadvantage at higher frequencies. Furthermore, the designed antenna provides good VSWR (less than 2.4) over the operating frequency band. Based on these characteristics, the proposed antenna can be useful for EMC applications.

ACKNOWLEDGEMENT

This paper has the financial support of the Iran Telecommunication Research Centre.

REFERENCES

[1] H. Li, B. Z. Wang, and W. Shao, "Novel broadband reflectarray antenna with compound-cross-loop elements for millimeter-wave application," *Journal of Electromagnetic Wave and Applications*,vol. 21, no. 10, pp. 1333–1340, 2007.

[2] W. Ren, J. Y. Deng, and K. S. Chen, "Compact PCB monopole antenna for UWB applications," *Journal of Electromagnetic Wave and Applications*, vol. 21, no. 10, pp. 1411–1420, 2007.

[3] Y. Coulibaly, T. A. Denidani, and L. Talbi, "Design of a broadband hybrid dielectric resonator antenna for X-band," *Journal of Electromagnetic Wave and Applications*, vol. 20, no. 12, pp. 1629–1642, 2006.

[4] M. Naghshvarian-Jahromi, "Compact UWB bandnotch with transmission-line-fed," *Progress In Electromagnetics Research B*, vol. 3, pp. 283–293, 2008.

[5] S. N. Khan, J. Hu, J. Xiong, and S. He, "Circular fractal monopole antenna for low Vswr UWB applications," *Progress In Electromagnetics Research Letters*, vol. 1, pp. 19–25, 2008.

[6] M. A. Saed, "Broadband CPW-FED planar slot antennas with various tuning stubs," *Progress In Electromagnetic Research,* vol. 66, pp. 199–212, 2006.

[7] S. Xiao, J. Chen, X.-F. Liu, and B. Z. Wang, "Spatial focusing characteristics of time reversal UWB pulse transmission with different antenna arrays," *Progress In Electromagnetics Research B*, vol. 2, pp. 189–206, 2008.

[8] X.-C. Yin, C. Ruan, Y.-C. Ding, and J.-H. Chua, "A planar U type monopole antenna for UWB applications," *Progress In Electromagnetics Research Letters*, vol. 2, pp. 1–10, 2008.

[9] J.-J. Jiao, G. Zhao, F.-S. Zhang, H.-W. Yuan, and Y.-C. Jiao, "A broadband CPW-FED T-shape slot antenna," *Progress In Electromagnetic Research,* vol. 76, pp. 237–242, 2007.

[10] K. L. Walton and V. C. Sundberg, "Broadband ridged horn design," *Microwave J.*, pp. 96–101, March 1964.

[11] J. L. Kerr, "Short axial length broad-band horns," *IEEE Trans. Antennas Propagat.*, vol. AP-21, pp. 710–714, Sept. 1973.

[12] S. Hopfer, "The design of ridged waveguides," *IRE Trans. Microwave Theory Tech.*, vol. MIT-3, pp. 20–29, October 1955.

[13] S. B. Cohn, "Properties of ridged waveguide," *Proc. IRE*, vol. 35, pp. 783–788, Aug. 1947.

[14] D. A. Jarvis, and T. C. Rao, "Design of double-ridged rectangular waveguide of arbitrary aspect ratio and ridge height,"

Microw. Antenna Propagat., IEE Proc., vol. 147, pp. 31–34, 2000.

[15] C. Reig and E. Navarro, "FDTD analysis of E-sectoral horn antenna for broadband applications," *IEEE Trans. Antennas Propag.*, vol. 45, no. 10, pp. 1484–1487, Oct. 1997.

[16] R. Bunger, R. Beyer, and F. Arndt, "Rigorous combined mode-matching integral equation analysis of horn antennas with arbitrary cross section" *IEEE Trans. Antennas Propag.*, vol. 47, no. 11, pp. 1641–1648, Nov. 1999.

[17] C. Bruns, P. Leuchtmann, and R. Vahldieck, "Analysis and simulation of a 1–18 GHz broadband double-ridged horn antenna," *IEEE Transaction on Electromagnetic Compatibility*, vol. 45, pp. 55–59, February 2003.

[18] M. Botello-Perez, H. Jardon-Aguilar, and I. Ruiz, "Design and simulation of a 1 to 14 GHz broadband electromagnetic compatibility DRGH antenna," *ICEEE-ICE 2005, 2nd International Conference on Electrical and Electronics Engineering*, pp. 118–121, Sept. 2005.

[19] V. Rodriguez, "New broadband EMC double-ridged guide horn antenna," *R. F. Des*., pp. 44–47, May 2004.

[20] M. Abbas-Azimi, F. Arazm, J. R. Mohassel, and R. Faraji-Dana, "Design and optimization of a new 1–18 GHz double ridged guide horn antenna," *Journal of Electromagnetic Wave and Applications*, vol. 21, no. 4, pp. 501–506, 2007.

Alireza Mallahzadeh was born in Bushehr, a beautiful city in the south of Iran in 1977. He received the B.S. degree in electrical engineering from Isfahan University of Technology, Isfahan, Iran, in 1999 and the MSc. degree in electrical engineering from Iran University of Science and Technology, Tehran, Iran, in 2001, and the PhD. degree in electrical engineering from Iran University of Science and Technology, Tehran, Iran, in 2006. He is a member of academic staff, Faculty of Engineering, Shahed University. He is interested in numerical modeling, antennas and microwaves.

Ali Imani was born in Malayer, Iran, in 1982. He received the B.S. degree in electrical engineering from Tabriz University, Tabriz, Iran, in 2006, and the M.Sc. degree in electrical engineering from Shahed University, Tehran, Iran, in 2009, and he is currently a PhD. student at the Iran University of Science and Technology, Tehran, Iran. His research interests include Electromagnetics Theory, Microwave Structures, slot antennas, double and quad ridged antennas, and monopole antennas.

Two-Dimensional Pattern Scanning by Linear Phased Array with Pattern Reconfigurable Elements

Yan-Ying Bai, Shaoqiu Xiao, Bing-Zhong Wang, and Shanshan Gao

The Institute of Applied Physics, University of Electronic Science and Technology of China, Chengdu, China, 610054
xiaoshaoqiu@uestc.edu.cn

Abstract–In this paper, a linear phased array with pattern reconfigurable elements is studied to perform a two-dimensional pattern scanning. Compared with the traditional linear array, the new linear array can scan the patterns in two-dimensional directions , i.e. θ-direction and φ-direction. The results indicate that the main beam of the proposed array can continuously scan from θ=30° to θ=150 ° in the *E*-plane by adjusting the feed phases of reconfigurable elements and from φ=-50° to φ=50° in the H-plane by switching the elements operating states.

Index Terms–array antenna, reconfigurable, pattern synthesis, scanning, microstrip antenna.

I. INTRODUCTION

Phased array is studied extensively because it can provide a high gain and scan its patterns [1]. The elements in phased array may be arranged in a line or a plane. The linear phased array is used widely due to its simple configuration, and it can scan its radiation pattern in one-dimension. To perform a beam scanning in two-dimension, traditionally, a planar phased array is necessary, thus the complexity and cost of the array will be increased significantly. Recently, the reconfigurable antenna, which can reconfigure its patterns and frequencies using PIN or MEMS switches, has been presented and studied extensively [2-3]. Because an additional degree of freedom is added, the reconfigurable antenna has a tremendous potential to improve the performance of the phased array. Some efforts have been made to apply the reconfigurable antenna into phased array design [4]. In this paper, a linear phased array with pattern reconfigurable elements is proposed to realize two dimensional scanning through adjusting reconfigurable element feed phases in one dimension and shifting the elements operating states in the other dimension.

II. RECONFIGURABLE ANTENNA ELEMENT

The geometry of the antenna is shown in Fig. 1. The antenna consists of three parallel strips printed on a grounded dielectric substrate with a relative dielectric constant of ε_r=2.2 and a thickness of H=6.35mm. All of the strips have a width of W=2.0mm. The center strip length is L_m=29mm, and is fed with a coaxial probe. This feed probe is moved g=11.8mm away from the end of the center strip to improve the impedance match. The two parasitic strips have the same length of L_r=33mm. The space between the adjacent strips is S=20mm. A gap with a width of d_m=1.2mm is located close to each end of the parasitic strips and 2.0mm (d_1) away from the strip end. Four switches, i.e., k1, k2, k3 and k4, are installed in four gaps, respectively. The parasitic strips can be elongated or shortened by closing or opening the switches. The ground

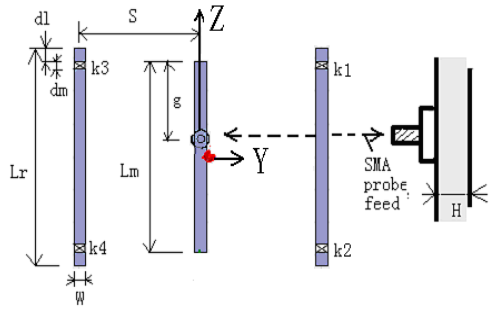

Fig. 1. Geometry of the pattern reconfigurable antenna element.

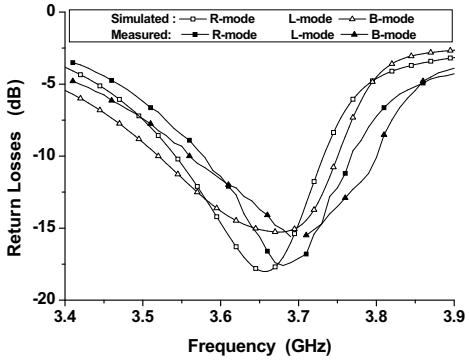

Fig. 2. Simulated and measured return losses for the three modes.

plate has an area of 90mm×140mm.

When *k*1 and *k*2 are open, *k*3 and *k*4 are closed, the effective length of the left parasitic strip is longer than the right one, and the pattern in *xoy*-plane turns right (i.e., positive plane). In this case the antenna operation is called *R*-mode. According to the symmetry, when *k*1 and *k*2 are closed, *k*3 and *k*4 are open, the called *L*-mode can be constructed and its pattern in *xoy*-plane turns left (i.e., negative plane).When all switches are open, the antenna pattern is broadside, the same as the conventional antenna, shortly named *B*-mode. The antenna is simulated using commercial software Ansoft HFSS9.0. As in [5-7], the ideal switch model is used in measuring the characteristics because it can provide an acceptable error. The simulated and measured return losses are shown in Fig. 2. The result indicates that the antenna can operate well around 3.67GHz in the three modes. The simulated and measured radiation patterns in the *E*-plane (*xoz*-plane) and *H*-plane (*xoy*-plane) at 3.67GHz are shown in Fig. 3. Based on Fig. 3, it can draw the conclusion that the main beam of the antenna can be scanned in *H*-plane by switching the antenna states among *L*-, *R*-, and *B*-modes. The main beam direction and the corresponding half power beam coverage in *H*-plane are (*R*-mode, φ=30°, 2°~60°), (*L*-mode, φ=-30°, -2° ~-60°) and (*B*-mode, φ=0°, -30°~30°), respectively. The gains are 8.80, 8.80 and 8.03dBi, and the half power beam coverage in *E*-plane are (53°~117°), (53°~117°) and (48°~138°), respectively, for *L*-, *R*- and *B*-modes.

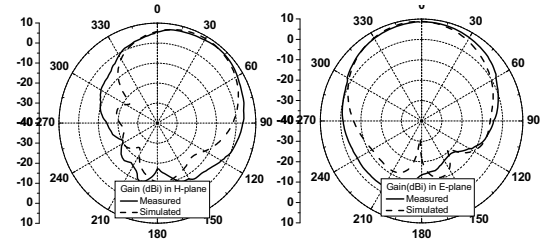

(a)

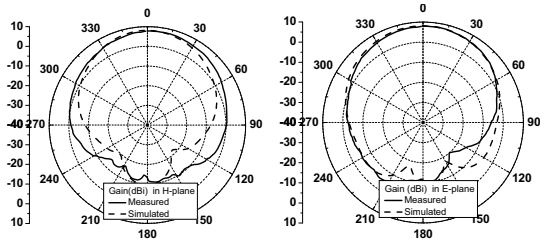

(b)

Fig. 3. Simulated and measured radiation patterns at 3.67 GHz; (a) *R*-mode and (b) *B*-mode.

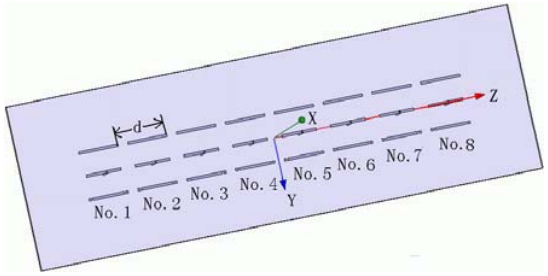

Fig. 4. Configuration of the linear phased array.

III. LINEAR PHASED ARRAY WITH RECONFIGURABLE ANTENNA ELEMENTS

Figure 4 shows the configuration of the proposed linear phased array. Eight elements, named *No.1-No.8*, are arranged along *z*-axis with an element spacing of $d=\lambda_0/2$, where λ_0 is the wavelength in free space at the operation frequency. All of the elements in the phased array operate with the same mode. The return losses of each port and the mutual couplings between elements are studied. When the array operates with *R*-mode, the simulated return losses of each port and the mutual couplings between two adjacent elements are shown in Fig. 5. In this figure, it can be observed that a return loss of -18dB is achieved for each port and a mutual coupling of less than -26dB is obtained between the adjacent elements at the operation frequency of 3.67GHz. The additional studies also demonstrate that the mutual coupling between other elements is lower due to a larger spacing. When the phased array operates with *B*-mode, the low return losses and the weak mutual couplings between antenna elements can be obtained, too.

The radiation characteristics of the uniform phased array are analyzed. When the phased array operates in *R*-mode, the array can scan its patterns in *E*-plane (i.e., $\varphi=30^o$) by changing the progressive phase $\Delta\psi$. The local coordinate system $x'y'z'$ displayed in Fig. 6 is used to observe the patterns of the phased array. The *E*-plane scan characteristic vasi $\Delta\psi$ are shown in Fig. 7(a) and the patterns in *H*-plane are shown in Fig.7(b). While the array is scanning, the x' axis and z' axis are turning in the plane $\varphi=30^o$ (i.e., *E*-plane) of the *xyz* coordinate system with the x' axis pointing to the maximum radiation at all time. The y' axis is perpendicular to the $x'o'z'$ plane, is pointing the positive direction of the y axis and is changeless. The $x'o'y'$ plane is the *H*-plane of the array, so the *H*-plane of the array is being changed while the array is scanning.

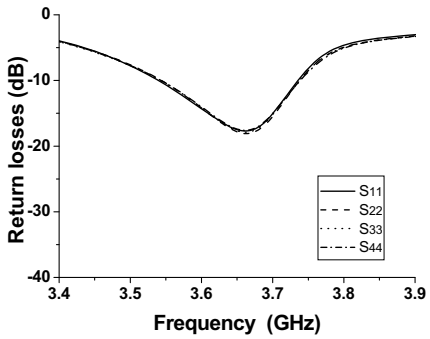

(a)

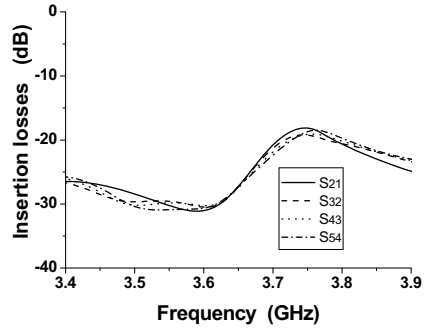

(b)

Fig. 5. Simulated return losses of each port and mutual coupling between adjacent elements in R-mode: (a) return loss and (b) mutual coupling.

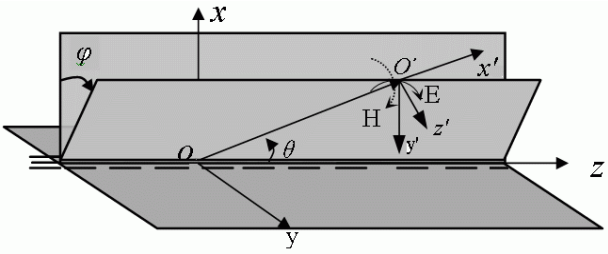

Fig. 6. Three-dimensional coordinate systems for array with R-mode.

Based on the symmetry, when the linear phased array operates in *L*-mode the radiation characteristics can be obtained. When the array operates with *B*-mode, it can scan its patterns in *E*-plane (i.e., $\varphi=0^o$) and the results are shown in Fig. 8. While scanning, the local coordinate system $x'y'z'$ is constructed as the one in *R*-mode and the scan characteristic in *H*-plane are obtained. The detailed data of *R*- and *B*-mode are listed in Table 1. From Table 1, we can

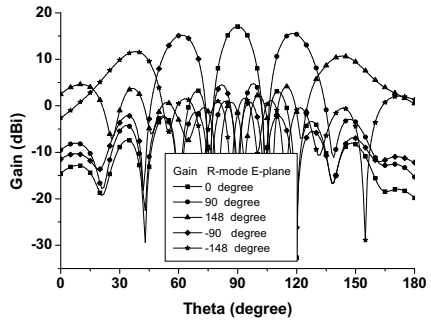

(a)

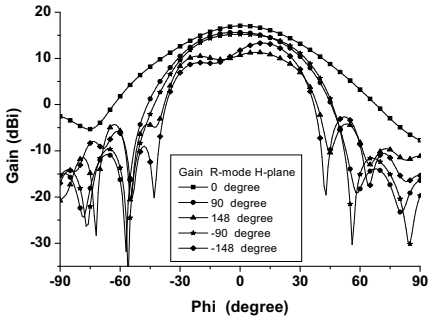

(b)

Fig. 7. Radiation pattern of linear phased array in R-mode with various progressive phases: (a) *E*-plane: φ=30° and (b) *H*-plane.

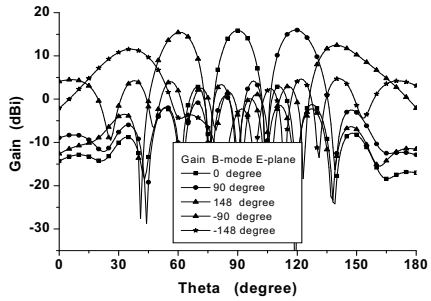

(a)

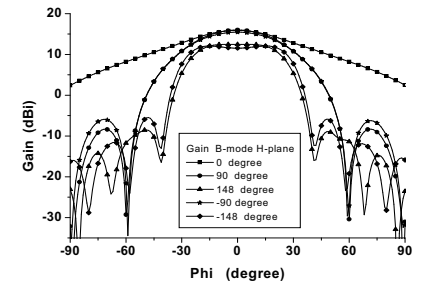

(b)

Fig. 8. Radiation pattern of the linear phased array in *B*-mode with various progressive phases: (a) *E*-plane: φ=0° and (b) *H*-plane.

observe that unlike the traditional linear array, the proposed linear phased array can realize the two-dimensional pattern scanning (i.e., θ-direction and φ-direction). Based on the studies above, the proposed linear array can continuously scan its main beam from θ=30° to θ=150° in *E*-plane by adjusting the feed phases of reconfigurable elements and from φ=-50° to φ=50° in *H*-plane by shifting the elements operating states.

Table 1. Pattern characteristics in *R*- and *B*-modes with various progressive phases.

$\Delta\psi$	Predicted main beam directions (θ_0, φ_0)	3dB beam coverage in local coordinate system shown by Fig. 5coverage		Gain (dBi)
		E-plane($x'o'z'$-p	H-plane($x'o'y'$-pl	
***R*-mode**				
-148°	(38°,	θ'=80° ~98°	φ'=-5° ~-25°	12.3
-127°	(47°,	θ'=82° ~98°	φ'=-24° ~27°	13.0
-90°	(62°,	θ'=82° ~96°	φ'=-23° ~26°	15.2
-60°	(71°,	θ'=84° ~96°	φ'=-25° ~26°	16.3
-30°	(81°,	θ'=84° ~95°	φ'=-23° ~26°	16.8
0°	(90°, 30°)	θ'=84°~96°	φ'=-24°~26°	17.0
30°	(99°,	θ'=84° ~96°	φ'=-24° ~25°	16.9
60°	(109°,	θ'=84° ~96°	φ'=-24° ~25°	16.5
90°	(118°,	θ'=84° ~97°	φ'=-24° ~25°	15.6
127°	(131°,	θ'=83° ~99°	φ'=-25° ~25°	13.4
148°	(143°,	θ'=81°	φ'=-5° ~25°	11.3
***B*-mode**				
-148°	(36°,	θ'=78° ~101°	φ'=-28° ~28°	11.5
-127°	(47°,	θ'=78° ~98°	φ'=-24° ~24°	14.5
-90°	(61°,	θ'=77° ~96°	φ'=-24° ~24°	15.4
-60°	(71°,	θ'=84° ~96°	φ'=-27° ~26°	15.6
-30°	(81°,	θ'=84° ~96°	φ'=-28° ~28°	15.7
0°	(90°, 0°)	θ'=84° ~96°	φ'=-29° ~29°	15.9
30°	(100°,	θ'=84° ~95°	φ'=-28° ~28°	16.0
60°	(109°,	θ'=86° ~96°	φ'=-26° ~25°	16.1
90°	(119°,	θ'=86° ~97°	φ'=-23° ~23°	16.0
127°	(133°,	θ'=82° ~101°	φ'=-22° ~22°	14.8
148°	(140°	θ'=82° ~102°	φ'=-24° ~24°	12.5

IV. CONCLUSION

A linear phased array with pattern reconfigurable elements is proposed in this paper. The array elements operate in three switchable states with good performances. The linear phased array can perform the two-dimensional pattern scanning by combining

the reconfigurable antenna technology with the traditional linear phased array antenna. The new linear array can scan its main beam from θ=30° to θ=150° in *E*-plane by adjusting the feed phases of reconfigurable elements and from φ=-50° to φ=50° in H-plane by switching the elements operating states.

ACKNOWLEDGEMENT

This work was in part supported by aviation Science Foundation under grant 20090180007, in part by the new-century talent program of the education department of China under grant NCET070154, in part by national defense research funding under grant 08DZ0229 and 09DZ0204, and in part by research funding of the 25th Institute of China Aerospace Science and Industry Corp.

REFERENCES

[1] J. M. Robert, *Phased Array Antenna Handbook,* Second Edition, Beijing: Publishing House of Electronics Industry, 2007.

[2] J. Zhang and A. Wang, "A Survey on reconfigurable antennas", *Microwave and Millimeter Wave Technology International Conference, ICMMT 2008*, vol. 3, pp. 1156 -1159, April 2008.

[3] H. H. Greg and J. T. Bernhard, "Integration of packaged RF MEMS switches with radiation pattern reconfigurable square spiral microstrip antennas", *IEEE Transactions on Antennas and Propagation*, vol. 54, no. 2, pp. 464- 469, 2006.

[4] T. L. Roach and J. T. Bernhard, "Investigation of Side lobe Level Performance in Phased Arrays with Pattern Reconfigurable Elements", *IEEE Antennas and Propagation International Symposium*, pp. 105-108, June 2007.

[5] S. Zhang, G. H. Huff, J. Feng, and J. T. Bernhard, "A Pattern Reconfigurable Microstrip Parasitic Array", *IEEE Transactions on Antennas and Propagation*, vol. 52, pp. 2773-2776, 2004.

[6] F. Yang and Y. Rahmat-Samii, "Patch antenna with switchable slot (PASS): dual frequency operation", *Microwave and Optical Technology Letters*, vol. 31, no. 3, pp. 165-168, 2001.

[7] J. Kiriazi and H. Ghali, "Reconfigurable dual-band dipole antenna on silicon using series MEMS switches", *IEEE Antennas and Propagation Society International Symposium*, vol. 1 , pp. 403-406, June 2003.

Yan-Ying Bai received the B.S. degree in physics from Jishou University, Jishou, China, in 2000, and the M.S. degrees in electromagnetic field and microwave engineering from the University of Electronic Science and Technology of China (UESTC), Chengdu, in 2005. She is pursuing her PhD degree and has gone in for antenna study since 2008 at UESTC.

Shaoqiu Xiao received the B.S. degree in physics from Jishou University, Jishou, China, in 1997, and the M.S. and Ph.D. degrees in electromagnetic field and microwave engineering from UESTC, Chengdu, in 2000 and 2003, respectively. In January 2004, he joined the Institute of Applied Physics, UESTC, as a Lecturer. Since July 2004, he has been with the Wireless Communications Laboratory (WCL), National Institute of Information and Communications Technology of Japan (NICT), Singapore. His research interests are antenna design, MMIC design and computational electromagnetics.

Size Reduction and Harmonic Suppression of Parallel Coupled-Line Bandpass Filters Using Defected Ground Structure

F. Karshenas[1], A. R. Mallahzadeh[1], and J. Rashed-Mohassel[2]

[1] Faculty of Engineering, Shahed University, Tehran, Iran
Begrezen@yahoo.com

[2] Faculty of Engineering, University of Tehran, Iran

***Abstract*—** A novel miniaturized parallel coupled-line bandpass filter with suppression of second, third and fourth harmonic frequencies, is demonstrated in this paper. The new filter is based on the slow-wave effect of the Defected Ground Structure (DGS) to achieve size minimization, while the spurious responses are eliminated by the band-rejection property of the DGS unit. These features offer the classical parallel coupled-line bandpass filter simultaneous compactness and wide stopband performance. Using the proposed DGS unit, does not require the filter parameters to be recalculated and, this way, the classical design methodology for microstrip parallel coupled-line filters can still be used. As an example, a 2.0 GHz parallel coupled-line filter has been designed and measured in order to show the validity of the proposed DGS. Compared with the conventional parallel coupled-line bandpass filters, the second, third and fourth measured spurious responses are suppressed to -45, -43 and -34 dB, respectively. In addition, the size of the prototype filter is reduced by 20% compared to that of the conventional parallel coupled-line filter.

***Index Terms*—** Coupled line filter, bandpass filter, Defected Ground Structure.

I. INTRODUCTION

Designing a bandpass filter with wide bandwidth, compact size, low insertion loss and also wideband rejection is still a challenging task. In planar microstrip realization, one of the most common implementation methods is to use a cascade of parallel coupled sections. Although this type of filter is indeed very popular and simple to implement, it does suffer from a fundamental limitation, namely, the presence of spurious responses which are generated at multiples of center frequency f_0, due to the unequal even- and odd-mode phase velocities of the coupled line. To eliminate these unwanted responses, especially for the second and third spurious responses, some methods have been recently proposed. In [1] and [2], an over-coupled resonator is proposed to extend phase length for the odd-mode to compensate difference in phase velocities. The structures in [3] and [4] use capacitors to extend the traveling path of the odd-mode. In [5], the authors used substrate-suspension technology with similar effectiveness. In addition to these structures, sinusoidal perturbation along the coupled-line width has been used [6]. The periodic sinusoidal perturbation offers wave impedance modulation so as to yield Bragg reflection at some frequencies. Besides the sinusoidal etching, indentation of rectangular-wave contour (square grooves) is presented in [7] and [8] and identical even- and odd-mode electrical lengths are achieved. Recently, Ahn [9] have studied parallel coupled-line resonators with defected ground structures (DGS) for suppression of the first spurious harmonic.

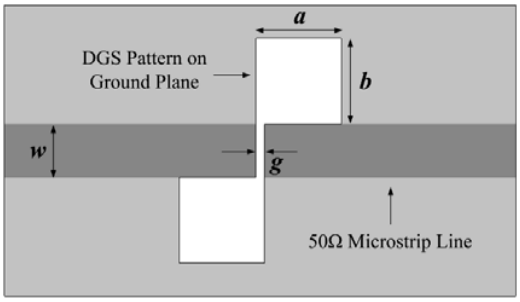

Fig. 1. Schematic top view of a slanted dumb-bell shaped DGS unit (w= 3.09 mm, a=b=5 mm, g=0.5 mm).

In addition to the disadvantage of spurious

responses, the conventional parallel coupled-line bandpass filter occupies large circuit size due to long strips of resonant conductors, which render the process inefficient and costly. In order to filter-size diminution, a novel terminated parallel coupled-line was recently proposed by Cheong [10]. This new coupled-line element cascade configuration leads to a new *N*-stage parallel coupled-line bandpass filter. In addition to this structure, Liu [11] introduced modified maximally flat parallel coupled-lines resonators by using enhanced coupling techniques.

Despite the above methodological differences, none have provided simultaneous multispurious suppression and major size reduction. In this paper, a novel DGS structure for microstrip parallel coupled-line filters is proposed to suppress the second, third and fourth harmonics simultaneously. Using the proposed DGS structure, the size of a parallel coupled-line filter is reduced up to 20% compared to that of the conventional parallel coupled-line filter, due to the slow-wave effect. In addition, the design procedure is very simple and does not need a recalculation of the coupled-line dimensions (space between lines and line width). This enhanced performance of the proposed bandpass filter has been verified by simulation and measurement; and a good agreement between these results is obtained.

II. CONFIGURATION AND EQUIVALENT CIRCUIT OF SLANTED DUMB-BELL DGS

Electromagnetic bandgap (EBG) and the defected ground structures (DGS) have recently gained numerous applications in microwave and millimeter-wave frequency bands with various configurations [12]–[16]. The DGS of a microstrip line is implemented by making artificial defect on the ground. Ground defect changes the distribution of shield current in the ground plane and the properties of microstrip changes accordingly.

The configuration of the proposed DGS on the ground plane of a microstrip line is shown in Fig. 1. It has a 50-Ω microstrip line on the top and a slanted dumb-bell shaped pattern which is etched in the ground plane. Slanted dumb-bell shaped DGS consists of two rectangular defects which are positioned in an aslant fashion and a slim vertical gap, wherein defects are coupled through the gap. This DGS was chosen with respect to the structure of the parallel coupled-line filter, since a normal dumb-bell shaped DGS may not be applied to a parallel coupled-line filter properly and it can overlap the adjacent resonators, thereby causing failure during the filter's operation.

As shown in Fig. 1 the microstrip line width is chosen as w=3.09 mm, for the 50Ω characteristic impedance. The substrate used in the simulation has the same parameters as FR4 with a board thickness of 1.5 mm. Simulation results are shown in Fig. 2, which illustrate the characteristic of a one-pole low-pass filter. The simulations are performed using CST Microwave Studio simulator which is based on finite integral technique.

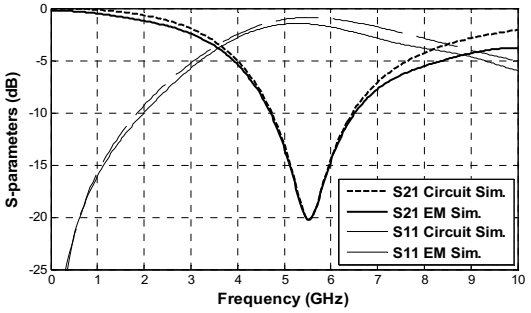

Fig. 2. EM and circuit simulations S-parameters.

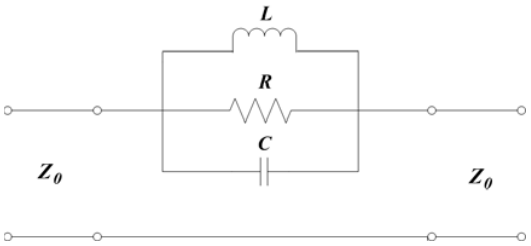

Fig. 3. Equivalent circuit of the microstrip line with one DGS unit.

As shown in Fig. 3, the frequency characteristics of the proposed DGS can be modeled by a simple parallel RLC resonator circuit which blocks the signal as an open at the resonant frequency [17]. The parameters of the equivalent circuit can be extracted from the simulated transfer characteristics. The inductance and the capacitance of the parallel RLC resonant circuit are related to the shape of the defects, as well as the gap width between the two left-hand-side defect and right-hand-side defect. This parallel RLC resonance can be used to reduce the length of the open transmission line resonator and shift the spurious response of an open transmission line resonator to a higher frequency

such that interference can be minimized. By the modeling technique in [17], the circuit parameters can be determined from equations (1)-(3).

$$C = \frac{\omega_c}{2Z_0(\omega_0^2 - \omega_c^2)} \quad (1)$$

$$L = \frac{1}{4\pi^2 f_0^2 C} \quad (2)$$

$$R = \frac{2Z_0}{\sqrt{\frac{1}{|S_{11}(\omega_0)|^2} - \left(2Z_0\left(\omega_0 C - \frac{1}{\omega_0 L}\right)\right)^2} - 1} \quad (3)$$

Here, ω_0 is the angular resonant frequency, ω_c is the lower 3-dB cutoff angular frequency, and Z_0 is the characteristic impedance of the microstrip line. Fig. 2 compares the S-parameters calculated by electromagnetic (EM) simulation for slanted dumb-bell shaped DGS in Fig. 1 and those calculated using the equivalent circuit in Fig. 3. Circuit simulation is performed by employing Advanced Design System (ADS) simulator.

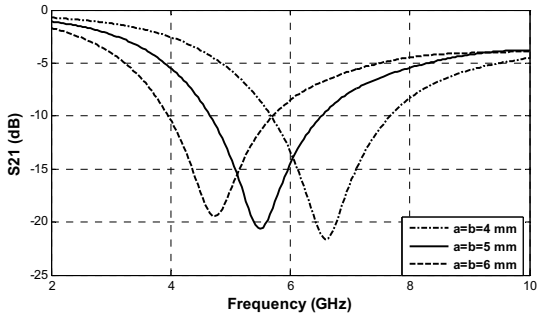

Fig. 4. Simulated insertion loss of slanted dumb-bell shaped DGS unit with different sizes. Here g=0.5 mm, the relative dielectric constant of the substrate is 4.4 and the thickness of the substrate is 1.5 mm.

For the slanted dumb-bell cell shown in Fig. 1, the resonant frequency (f_0) depends on the physical dimensions of the cell. For example f_0 can be reduced by using smaller gap g, larger a, or larger distance between the two squares. In fact, the etched gap and the etched square defect are related with the effective capacitance and inductance of the microstrip line. As the etched area of the square defect is decreased and the gap distance is kept constant to 0.5 mm, the effective series inductance decreases, and decreasing the series inductance gives rise to a higher cutoff frequency, as seen in Fig. 4. Since g is generally limited by PCB fabrication techniques, increasing the size of the cell is the practical approach of reducing the resonant frequency.

III. MICROSTRIP PARALLEL COUPLED-LINE BPF WITH SLANTED DUMB-BELL DGS

In order to demonstrate the effectiveness of the proposed DGS pattern, a parallel coupled-line filter with 2.0 GHz center frequency and 10% fractional bandwidth with slanted dumb-bell DGSs has been designed, and compared with a conventional parallel coupled-line filter. Same procedure can be used for harmonic suppression and size reduction of the parallel coupled-line filters with different response specifications.

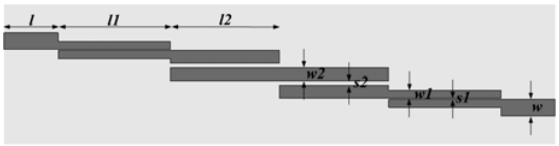

Fig. 5. Schematic top view of a three-order conventional parallel coupled-line filter (l_1=20.70 mm, l_2=20.08 mm, l=10 mm, w_1=1.53 mm, w_2=2.45 mm, w=3.09 mm, s_1=0.15 mm, s_2=0.77 mm, ε_r =4.4).

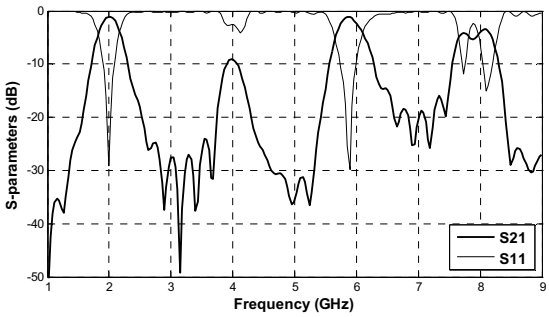

Fig. 6. Simulated S-parameters of the conventional parallel coupled-line filter.

Conventional parallel coupled-line filter exhibiting an N-order filter response comprises of N open transmission line resonators which are designed to have a length of approximately half of the wavelength, $\lambda_g/2$, at the center frequency. Therefore, the physical size of the conventional parallel coupled-line filter is large due to the length of the open transmission line resonators. This is a major disadvantage because it can be inefficient and costly for circuit applications.

Dimensions of a conventional parallel coupled-line filter are calculated for maximally flat response using [18]. Fig. 5 shows the design parameters of the conventional parallel coupled-line filter. A substrate with dielectric constant of 4.4 and a thickness of 1.5 mm is used.

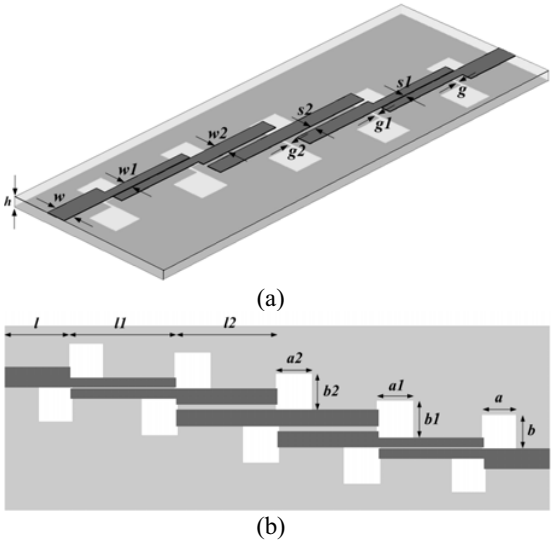

Fig. 7. Proposed parallel coupled-line filter (a) 3D view and (b) top view (l_1=15.70 mm, l_2=15.08 mm, l=10 mm, w_1=1.53 mm, w_2=2.45 mm, w=3.09 mm, s_1=0.15 mm, s_2=0.77 mm, ε_r=4.4, h=1.5 mm, a=b=5.1 mm, a_1=b_1=5.5 mm, a_2=b_2=5.5 mm, g=g_1=g_2=0.5 mm).

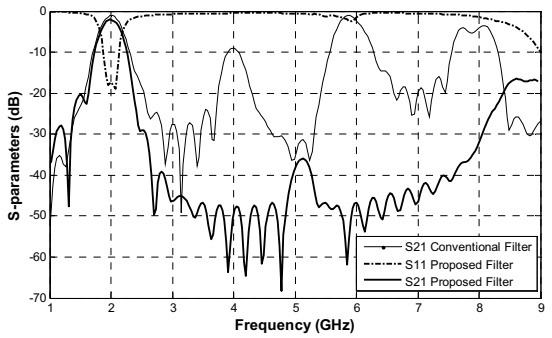

Fig. 8. Comparison between the simulated S-parameters of the proposed and conventional parallel coupled-line filter.

Simulated S-parameters of the conventional filter are shown in Fig. 6. The response curve shows that the spurious harmonics of the parallel coupled-line filter are around 4, 6, 8 GHz, which are multiples of the center frequency. This is another disadvantage of the conventional parallel coupled-line filter, because many other circuits can generate unwanted harmonics at these frequencies.

The configuration of the proposed parallel coupled-line filter with five slanted dumb-bell shaped DGS sections is illustrated in Fig. 7. To simplify the design process and simple fabrication, the etched pattern is symmetrically located under the microstrip line. The lattice dimensions of the 1st and 5th DGS sections and the 2nd, 3rd and 4th DGS sections are similar and are assigned to be 5.1 mm× 5.1 mm and 5.5 mm× 5.5 mm, respectively. The etched gap width is chosen to be 0.5 mm for both types of the DGS units. The length of the narrow gap is the same as the line-width of the corresponding open transmission line resonators.

The increase in effective inductance from insertion of the DGS can provide longer electrical length of transmission line than that of a conventional line, which enables size reduction of resonators. Since, the filter consists of three open transmission line resonators; we use three DGS units for size reduction i.e. 2nd, 3rd and 4th DGS units. Except the length of the resonators, other design parameters of the conventional parallel coupled-line filter remain intact. The 1st and 5th DGS units do not have any impact on the length, center frequency and bandwidth of the filter but are used to suppress the harmonic produced in 5.20 GHz (Fig. 8). As shown in Fig. 5 and Fig. 7, the conventional parallel coupled-line filter has the total length of 101 mm while the size of parallel coupled-line filter with slanted dumb-bell shaped DGS is 81 mm, this results 20% size reduction.

The band-rejection property of the DGS can be utilized in selective suppression of the unwanted harmonics. Since the resonant frequency of the DGS depends on the size of the defect on the ground, we need to adjust the size of defects to suppress the second, third and fourth harmonics simultaneously. Comparison of transmission characteristics between conventional and proposed parallel coupled-line filter described in Fig. 7 is given in Fig. 8. The simulation, exhibits that the proposed filter has successfully improved the spurious harmonics at $2f_0$, $3f_0$ and $4f_0$. The center frequency and bandwidth of the fundamental passband is kept as in the original filter and no significant deviation is observed. Furthermore, the insertion and return losses are -2.45 dB and -18.77 dB at the center frequency, respectively. The insertion loss is slightly larger due to the use of the DGS and high dielectric losses with loss tangent of 0.02.

Fig. 9 shows a general circuit model for modeling a parallel coupled-line filter with slanted dumb-bell shaped DGS. Each one of the DGS units is modeled with a parallel RLC resonant circuit, placed in series along the transmission line. Circuit parameters can be easily found from EM simulations using equations (1)-(3). Fig. 10 shows the S_{21} calculated by electromagnetic (EM) simulation and those calculated by using the equivalent circuit in Fig. 9. The equivalent-circuit simulation is performed by employing ADS. For S_{21} simulation, circuit simulation agrees with EM simulation at the low frequency region below 6 GHz. The difference at high frequencies is due to the radiation at DGS sections. In both simulations, it may be observed that the second, third and fourth harmonics are suppressed simultaneously by using DGS units.

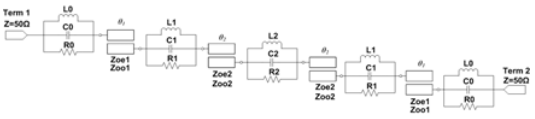

Fig. 9. Equivalent circuit model of the proposed parallel coupled-line bandpass filter.

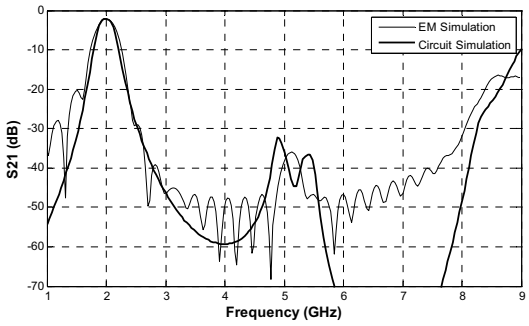

Fig. 10. S-parameters by EM and circuit simulations for the proposed parallel coupled-line filter.

IV. EXPERIMENT AND MEASUREMENT

An experimental parallel coupled-line filter is constructed using the results of the simulation. Fig. 11 shows the top and bottom views of the fabricated parallel coupled-line filter with slanted dumb-bell shaped DGS.

The measurements were performed with a vector network analyzer (Agilent 8722ES). Fig. 12 provides a comparison between simulated and measured transmission characteristics of the proposed parallel coupled-line filter. Good agreement between simulations and experimental data has been obtained. The little differences found can be due to the tolerances in the fabrication process.

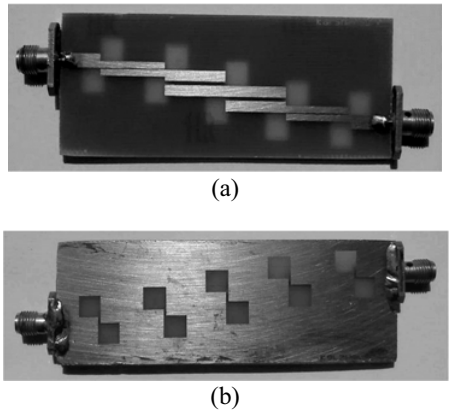

(a)

(b)

Fig. 11. Fabricated parallel coupled-line filter with slanted dumb-bell shaped DGS (a) top view and (b) bottom view.

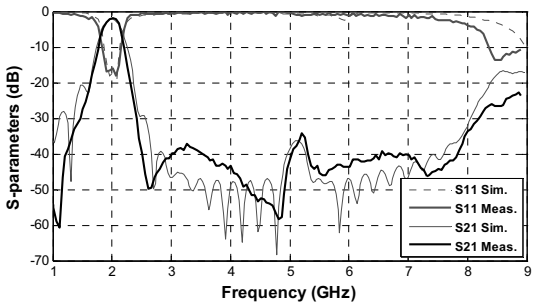

Fig. 12. Measured and simulated S-parameters of the proposed filter.

V. CONCLUSION

In this letter, a compact parallel coupled-line filter having harmonic suppression has been presented. Due to the increased slow wave factor and electrical length of the microstrip line with slanted dumb-bell shaped DGS, the size of the original parallel coupled-line filter has been reduced successfully without any critical deviation in center frequency and bandwidth. In addition, because of the band-rejection property of the slanted dumb-bell shaped DGS, the second, third and fourth harmonic frequencies are rejected. The proposed parallel coupled-line filter has been modeled by an equivalent-circuit and the simulation results of circuit modeling were in good agreement with those of EM simulation. By the simulation and experimental results of a 2.0

GHz prototype filter with 10% fractional bandwidth, 20% size miniaturization and a rejection level of better than 34 dB until $4f_0$ in the stopband can be achieved.

REFERENCES

[1] B. Easter and K. A. Merza, "Parallel-coupled-line filters for inverted-microstrip and suspended-substrate MIC's," *11th European Microwave Conference*, pp. 164-168, 1981.

[2] A. Riddle, "High performance parallel coupled microstrip filters," *IEEE MTT-S International Microwave Symposium Digest*, vol. 1, pp. 427-430, 1988.

[3] S. L. March, "Phase velocity compensation in parallel-coupled microstrip," *IEEE MTT-S International Microwave Symposium Digest*, vol. 82, pp. 410-412, 1982.

[4] J. Bahl, "Capacitively compensated high performance parallel coupled microstrip filters," *IEEE MTT-S International Microwave Symposium Digest*, vol. 2, pp. 679-682, 1989.

[5] T. Kuo, M. Jiang, and H. J. Chang, "Design of parallel-coupled microstrip filters with suppression of spurious resonances using substrate suspension," *IEEE Transactions on Microwave Theory and Techniques*, vol. 52, pp. 83-89, 2004.

[6] T. Lopetegi, M. A. G. Laso, J. H. M. Bacaicoa, D. Benito, M. J. Garde, M. Sorolla, and M. Guglielmi, "New microstrip "wiggly-line" filters with spurious passband suppression," *IEEE Transactions on Microwave Theory and Techniques*, vol. 49, pp. 1593-1598, 2001.

[7] T. Kuo, W. H. Hsu, and W. T. Huang, "Parallel coupled microstrip filters with suppression of harmonic response," *IEEE Microwave and Wireless Components Letters*, vol. 12, pp. 383-385, 2002.

[8] B. S. Kim, J. W. Lee, and M. S. Song, "Modified microstrip filters improving the suppression performance of harmonic signals," *IEEE MTT-S International Microwave Symposium Digest*, vol. 1, pp. 539-542, 2003.

[9] J. S. Park, J. S. Yun, and D. Ahn, "A design of the novel coupled-line bandpass filter using defected ground structure with wide stopband performance" *IEEE Transactions on Microwave Theory and Techniques*, vol. 49, no. 1, pp. 2037-2043, January 2001.

[10] P. Cheong and K. W. Tam, "Novel folded-end parallel-coupled-line microstrip filter with 2nd and 3rd harmonic responses suppression," *Mediterranean Microwave Symp*., p. 115, 2004.

[11] J. C. Liu, B. H. Zeng, J. M. Chang, C. H. Chien, C. C. Chang, and D. C. Chang, "Modified maximally flat parallel-coupled lines for band-pass filter applications and miniaturizations," *Microwave and Optical Technology Letters*, vol. 50, pp. 902-906, 2008.

[12] X. Q. Chen, X. W. Shi, Y. C. Guo, and M. X. Xiao, "A novel dual band transmitter using microstrip defected ground structure," *Progress In Electromagnetics Research (PIER)*, vol. 83, pp. 1-11, 2008.

[13] R. Sharma, T. Chakravarty, S. Bhooshan, and A. B. Bhattacharyya, "Design of a novel 3dB microstrip backward wave coupler using defected ground structure," *Progress In Electromagnetics Research (PIER)*, vol. 65, pp. 261-273, 2006.

[14] H. D. Oskouei, K. Forooraghi, and M. Hakkak "Guided and leaky wave characteristics of periodic defected ground structures," *Progress In Electromagnetics Researc (PIER)*, vol. 73, pp. 15-27, 2007.

[15] J. Chen, Z. B. Weng, Y. C. Jiao, and F. S. Zhang, "Lowpass filter design of hilbert curve ring defected ground structure," *Progress In Electromagnetics Research (PIER)*, vol. 70, pp. 269-280, 2007.

[16] J. S. Lim, H. S. Kim, D. Ahn, and S. Nam, "A power amplifier with efficiency improved using defected ground structure," *IEEE Microwave and Wireless Components Letters*, vol. 11, pp. 170-172, 2001.

[17] D. Ahn, J. Park, C. Kim, J. Kim, Y. Qian, and T. Itoh, "A design of the low-pass filter using the novel microstrip defected ground structure," *IEEE Transactions on Microwave Theory and Techniques*, vol. 49, pp. 86-93, 2001.

[18] S. B. Cohn, "Parallel-coupled transmission-line-resonator filters," *IRE Transactions on Microwave Theory and Techniques*, vol. 6, pp. 223-231, 1958.

Fardad Karshenas was born in Urmia, Iran, on March 22, 1982. He received the B.Sc. degree in bioelectric engineering from Shahed University, Tehran, Iran, in 2006, where he is working toward the M.S degree in electrical engineering.

His research interests are in the area of phased array, electromagnetic band-gap structures, filters and horn antennas.

Alireza Mallahzadeh was born in Bushehr, a beautiful city in the south of Iran in 1977. He received the B.S. degree in electrical engineering from Isfahan University of Technology, Isfahan, Iran, in 1999 and the MSc. degree in electrical engineering from Iran University of Science and Technology, Tehran, Iran, in 2001, and the PhD. degree in electrical engineering from Iran University of Science and Technology, Tehran, Iran, in 2006. He is a member of academic staff, Faculty of Engineering, Shahed University, Tehran, Iran. He has participated in many projects relative to antenna design, which resulted in fabricating different types of antennas for various companies. Also, he is interested in numerical modeling, and microwaves.

Jalil Rashed-Mohassel is a member of academic staff, Faculty of Engineering, Tehran University. Formerly he was with the university of Sistan and Baluchestan, Zahedan, Iran, where he held several academic and administrative positions. In 1994 he joined University of Tehran where he is doing teaching and research as a professor in antennas, EM theory and applied mathematics. He served as the academic Vice-Dean, Faculty of Engineering and is currently academic Vice-Chairman of ECE department, member of Center of Excellence on Applied Electromagnetic Systems and the director of the microwave laboratory. He received his MSc. in Electronics Engineering from University of Tehran in 1976 and his PhD. degree in Electrical Engineering in 1982 from University of Michigan, Ann Arbor.

Design and Analysis of Microstrip Photonic Band Gap Filter for Suppression of Periodicity

R. N. Baral and P. K. Singhal

Department of Electronics
Madhav Institute of Technology and Science
Gwalior – 474 005, INDIA
r_n_baral@yahoo.co.in, pks_65@yahoo.com

Abstract–A design for a microstrip band reject filter is presented in this paper. The proposed filter is compact in structure and provides an accurate band gap. Optimized length is applied to photonic band gap (PBG) structures etched in the ground plane for suppressing periodicity in the frequency response. Detailed analysis of the frequency response of the conventional microstrip filter along with the PBG filter has been carried out in this paper.

Keywords – Microstrip, Band Reject Filter (BRF), Photonic Band Gap (PBG).

I. INTRODUCTION

In recent times, the design of filters has become an active research area as filtering is important when used in close proximity to other circuit components, like power amplifiers in the transmitter part and low noise amplifiers in receiver part, for various RF applications. Filters can be implemented with shunt stubs [1] or stepped impedance lines in microstrip circuit [2], but these techniques require a large circuit and provide a narrow band, along with a spurious pass-band in stopband. PBG structures provide an alternative solution for these problems in microwave applications.

Microstrip lines incorporating photonic band gap structures exhibit slow wave characteristics which can be exploited to control the size of circuit layouts and periodicity. PBG structures are periodic where the propagation of waves is not allowed
for some frequency bands or directions, according to the Bragg condition [3]. This is quite similar to the energy band gap concept in solid-state materials, photonic crystals, etc., which provides a means to control propagation of the electromagnetic wave.

The present work is based on the design of a conventional band reject filter with optimum design parameters [3]. The frequency response possesses periodicity, but with the help of a periodic array of structures etched on the ground plane, the spurious band gap is controlled. We show that a discrete periodic pattern is able to suppress the periodicity in the frequency response by adjusting etched size in the ground plane. For synthesis of the circuit, rigorous analysis is required, particularly for the etched section, which is very difficult to calculate. Here, we have used method of moments based IE3D simulation software [4], for the complete analysis; subsequently the result obtained is discussed.

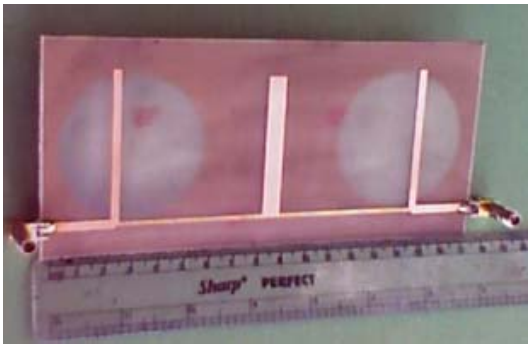

Fig. 1. Photographed layout of PBG filter.

II. FILTER DESIGN AND ANALYSIS

As shown in Fig. 1, the proposed filter is a transmission line network of a bandstop filter with open-circuited stubs, where the shunt, quarter wave-length open-circuited stubs are separated by unit elements, also called connecting lines, that are one quarter wavelength long at the mid stop band frequency. Theoretically, these filters can be designed to have any stopband width. But these filters are more suitable for the realization of wide-band band stop filters. The band reject filter is designed using the following equations for Ω_c = 1rad/sec and prototype elements, $g_0 = g_4 = 1$; $g_1 =$

$g_3 = 0.94806$; $g_2 = 1.67311$; $J_{1,2} = J_{2,3} = 0.56648$; [2]

$$Z_A = Z_B = Z_0/g_o \quad (1)$$
$$Z_i = Z_0/g_i \quad (2)$$
$$Z_{i,\,i+1} = Z_0/J_{j,j+1} \quad (3)$$

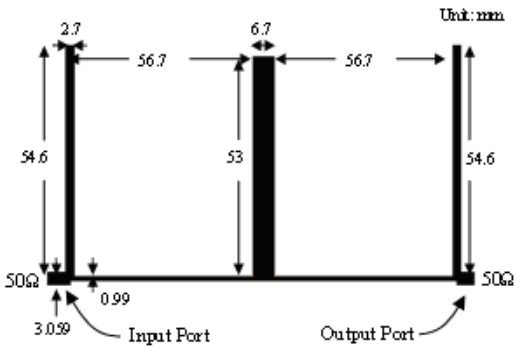

Fig. 2. Layout of microstrip band reject filter.

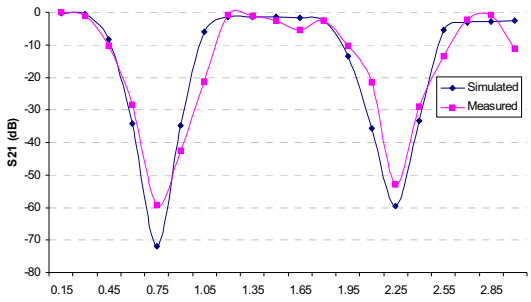

Fig. 3. Insertion loss plot of microstrip BRF.

The following are the design parameters for the proposed band stop filter:

Mid-band frequency, $f_0 = 0.75$GHz,
Dielectric constant, $\varepsilon_r = 4.4$,
Substrate thickness, h = 1.6 mm,
Loss tangent, tanδ = 0.02,
Pass band ripple = 0.1 dB,

The electrical parameters for the filter network are calculated as, $Z_0 = Z_A = Z_B = 50\Omega$, $Z_1 = Z_3 = 52.74$, $Z_2 = 29.88\Omega$, $Z_{1,2} = Z_{2,3} = 88.26\Omega$. The layout of the band stop filter is shown in Fig. 1. The microstrip filters is subsequently simulated through IE3D commercial tool [4]. The comparison plot of simulated and measured results is shown in Figs. 3 and 4. It is observed that the filter responses have spurious stop bands periodically centered at frequencies that are odd multiples of f_0. And for the microstrip band reject filter, the spurious band is found at 2.25 GHz which is '$3f_0$'.

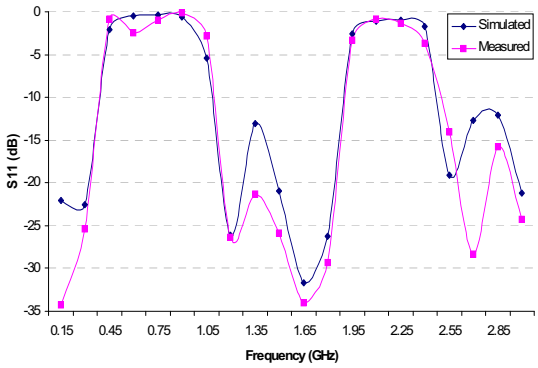

Fig. 4. Return loss plot of microstrip BRF.

III. PBG IMPLEMENTATION AND ANALYSIS

Initially, photonic band gap devices were proposed in optical applications, which have a property of preventing light from propagating in certain frequency bands [5]. In this work, we show that PBG structures with discrete periodic pattern are able to suppress the periodicity in the frequency response, with respect to 'n' – order of approximation or the number of PBG structures etched in the ground plane.

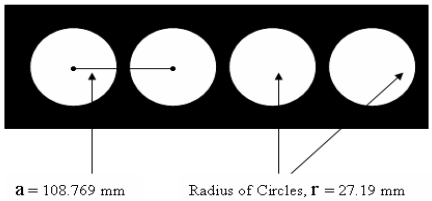

Fig. 5. Ground plane of the PBG filter.

According to the Bragg condition, the PBG structure satisfies the condition $a = \lambda_g/2$; where 'a' is the pattern period and λ_g is the guided mode wavelength [6]. And for PBG microstrip structures with circular etched holes, the optimal etched hole size is a ratio of r/a = 0.25, r – being the circle radius [7]. And it is stated in [8] they have stopband regions at different harmonics.

Fig. 5 shows the etched ground for the PBG band stop filter. The period between circles 'a' is calculated to be 108.77 mm, for $\lambda_g = 217.54$ mm and radius of the circles, r = 27.19 mm. The analytical and measured plots for insertion loss and return loss, for the PBG filter are shown in

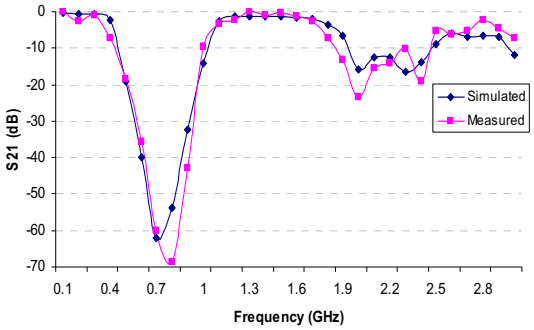

Fig. 6. Insertion loss plot for PBG filter.

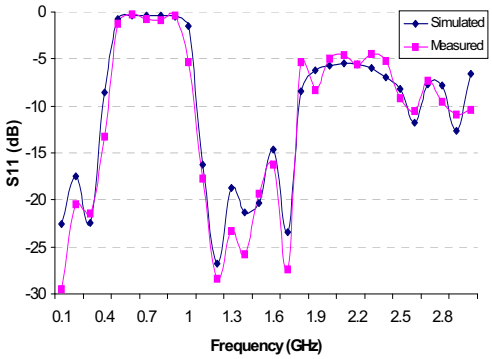

Fig. 7. Return loss plot for PBG filter.

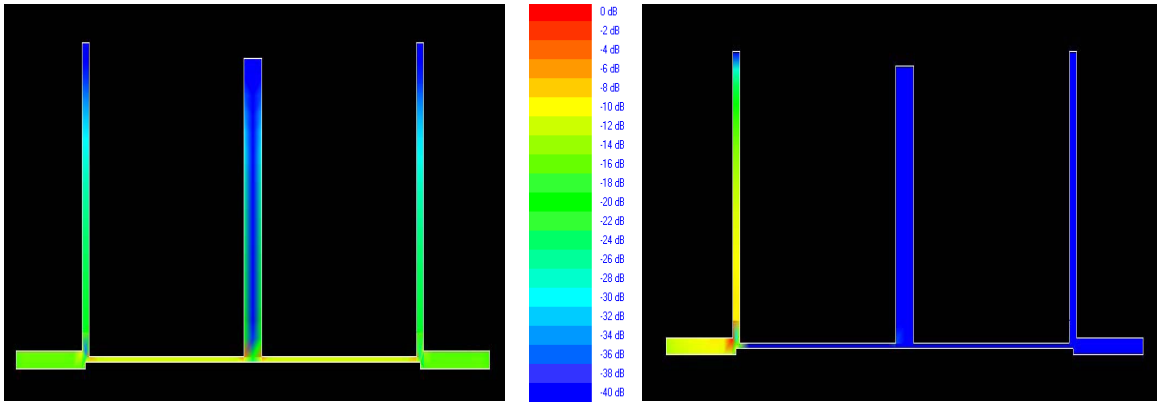

(a) (b)

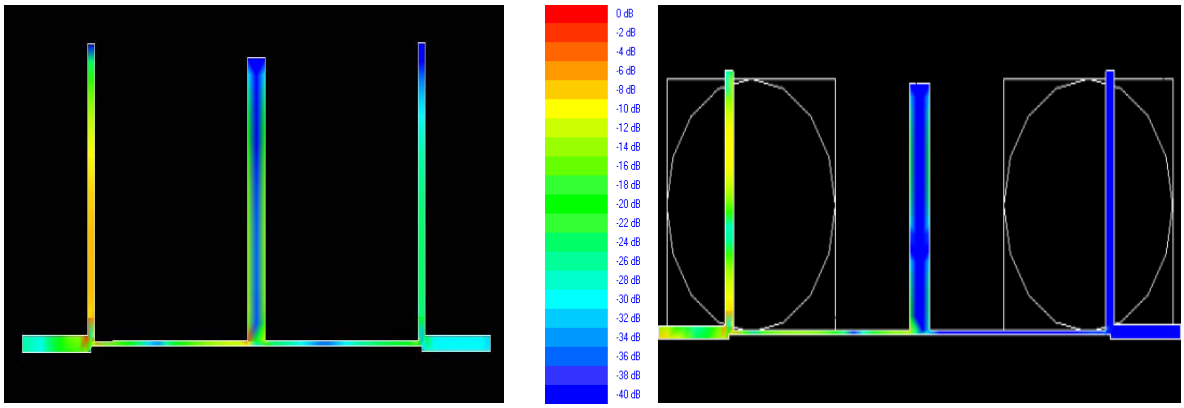

(c) (d)

Fig. 8. Distribution of the magnitude of the current density on (a) f_c = 0.4GHz, (b) f_c = 0.75GHz, (c) f_c = 0.9GHz, and (d) f_c = 2.25GHz.

Figs. 6 and 7, respectively.

The results show good agreement with the numerical analysis, as there is suppression of the stop band at frequency, f = 2.25 GHz which has an insertion loss of nearly 22 dB, in contrast to -60dB for the conventional band reject filter. All the filters physically implemented on FR-4 'Glass/Epoxy', using conventional fabrication process. Since the Zeland IE3D software is based on the moments method, and the current distribution on filter elements is one of the primary quantities concerned, we use this program to analyze current distributions.

The current distribution function of proposed filter is shown in Figs. 8 (a-d). From the current distribution plots it is observed that the current concentration is nearly uniform for the low frequencies, and shows high attenuation at the center frequency 0.75GHz, whereas at a high frequency the distribution is completely non-uniform with more current concentration at the input port.

IV. CONCLUSION

It is observed from the simulation results that with the implementation of photonic band gap property in conventional microstrip filters, there is significant improvement in the frequency response. Spurious bands are undesirable for RF applications, and with the use of photonic band stop characteristics to forbid specific frequency bands, the proposed design may be very useful for wireless and mobile applications.

ACKNOWLEDGEMENT

The authors thankfully acknowledge the financial support provided by M.P. Council of Science & Technology, Bhopal, India.

REFERENCES

[1] K. L. Finch and N. G. Alexopoulos, "Shunt posts in microstrip transmission lines", *IEEE Trans. Microwave Theory Tech.*, vol. MMT.-38, pp. 1585-1594, 1990.

[2] J.-S. G. Hong and M.J. Lancaster, *Microstrip Filters for RF/Microwave Applications*, John Wiley & Sons Inc, 2001.

[3] D. M. Pozar, *Microwave Engineering*, John Wiley, 2000.

[4] IE3D Software Release – 8, Developed by M/s Zeland Software Inc.

[5] J. D. Joannopoulos et al., *Photonic Crystals: Molding the flow of light*, Princeton University Press, 2000.

[6] A. D'Ozario, et al., "Tapered Photonic Band Gap Microstrip Low Pass Filter: Design and Realisation", *IEEE Proc. Microwave Antenna Propag.*, vol. 150, no. 6, pp. 459-462, 2003.

[7] V. Radisic, et al., "Novel 2-D Photonic Band Gap structure for microstrip lines", *IEEE Microwave guided wave Letter*, vol. 8, no. 2, pp. 69-71, 1998.

[8] T. Lopetegi et al., "Novel band gap microstrip structures using network topology", *Microwave Opt. Letter*, vol. 25, no. 1, pp.411-412, 1999.

R. N. Baral was born in 1976, received his Bachelors degree in 1998 from Institution of Electronics and Telecommunication Engineers. He got his Masters degree in 2002 from MITS, Gwalior. Currently he is pursuing his PhD degree from RGPV, Bhopal, India, on "Design and Analysis of Microstrip Filters". To date, he has eighteen papers at the national and international level. He is a life member of Institute of Electronics and Telecommunication Engineers (I.E.T.E.), New Delhi, India.

P. K. Singhal was born in 1965. He received the B.E. and Ph.D. degrees in electronics engineering from Jiwaji University, Gwalior, India, in 1987 and 1997, respectively, and the M. Tech. degree in microwave electronics from the University of Delhi, Delhi, India in 1989. Curently, he is working as a Professor in the Department of Electronics Engineering, Madhav Institute of Technology and Science, Gwalior, India. He has about 90 publications to his credit at the national and international level. His research interests include electromagnetics, communication systems, microwave circuits, and antennas. Dr. Singhal is a lifetime member of the India Society for Technical Education (ISTE), the Computer Society of India (CSI), the Institution of Engineers (India), and the Institute of Electronics and Telecommunications Engineers (IETE).

Capacity Investigations of MIMO Systems in Correlated Rician Fading Channel Using Statistical Clustered Modelling

Mohab A. Mangoud

Department of Electrical and Electronics Engineering
University of Bahrain, P.O.Box 32038, Isa Town, Kingdom of Bahrain
mangoud@eng.uob.bh

***Abstract*—** In this paper the capacity of MIMO systems is investigated for different realistic propagation scenarios in Rician fading channel. A nonparametric stochastic model is presented and is used to develop the spatial fading correlation. Uplink statistical MIMO channel is assumed with Laplacian angular energy distributed over multi-clusters situations. Radio waves that are gathered in several clusters distributed over the space domain are assumed to exhibit different power profiles. Capacity investigations for both uniform linear array (ULA) and uniform circular array (UCA) for single cluster and multi-clustered assumptions are presented. The optimum selections of number of elements and spacing between elements are discussed for different values of Angle of Arrival (AoA) and Azimuth Spread (AS). Also, the impact of *K* factor of the Rician distribution for single and multi-clusters environments is studied under different propagation scenarios.

***Index Terms*—** MIMO Systems, Statistical Channel Model, Capacity Investigations, Spatial Correlation, Power Azimuth Spectrum (PAS), Uniform Linear Array (ULA), Uniform Circular Array (UCA), Rician Fading.

I. INTRODUCTION

The spatial fading correlation of the channel has an adverse effect on the capacity of Multiple Input Multiple Output (MIMO) systems [1]. Accurately computing the spatial correlations is essential for predicting system performance. However, it is always a challenging task to evaluate the realistic correlation matrices with high accuracy due to the interdependence between the propagation environment and the antenna geometry and clustering of scatterers in the propagation environment. In [2]–[7], stochastic none physical MIMO models with different assumptions about the scattering in the propagation environment and antenna geometries are considered. In these statistical clustered vector channel models, the groups of scatterers are modeled as clusters located around the antenna arrays. In [2] the parametric stochastic MIMO channel model is presented to estimate the performance of MIMO systems in terms of theoretical capacity. Cross-correlation functions of the received signal at two antenna elements with three different PAS (uniform, truncated Gaussian and truncated Laplacian). Exact expressions of the spatial correlation coefficients were derived for the different spatial distributions of AOD/AOA only for uniform linear arrays (ULAs). The model is applied for two case studies employing ULA array type, one for single cluster case and the other for bi-cluster assumption. For the antenna geometry selection, ULA is the most common geometry in cellular systems. However, UCA shows potential as an alternative geometry with its enhanced properties. Analysis of fading correlation was carried out for UCA in [3]–[5]. In the previous works the authors consider a single cluster model in Rayleigh channel. It is also known that the presence of LOS component along with the correlation between channel links may affect the capacity of the MIMO system [8]. In [8] analytical multivariable statistics is presented to obtain the upper bound for the pairwise error probability of the system under space time correlation Rician fast fading channel. However, the effect of Rician *K* factor on the capacity curves of correlated fading using simulation models need to be more investigated.

Thus, according to the previous discussion, the objective of this paper is to study the impact of having multi-clusters propagation scenarios and compares it with single cluster case for MIMO systems utilizing Hybrid ULA/UCA

configuration at both ends of Rician fading channel. This paper addresses the accuracy when modelling the spatially correlated MIMO channel using clustered channel model (that is developed from the models presented in [2]-[7]). The paper is organized as follows. In Section II, the nonparametric clustered MIMO model and special correlation matrix calculations are provided. In section III, the numerical results are presented for practical uplink MIMO system simulations with a detailed discussion for the numerical results. Some remarks will be carried out to highlight the effect of the choice of modelling assumptions on the capacity curves and the model applicability for practical systems. Finally, conclusions are derived in Section IV.

II. SPATIAL FADING CORRELATION AND CLUSTERED CHANNEL MODELS

Figure 1 shows a MIMO uplink scenario that is modeled in our investigations with transmitter at the mobile unite (MU) and receiver at the base station (BS). The channel is modeled as multi-clusters scattering environment which means that the signal will arrive at the BS from multiple Angles of Arrival (AoA) each with Azimuth spread (AS) that is a measure of the angle displacement due to the non-LOS propagation.

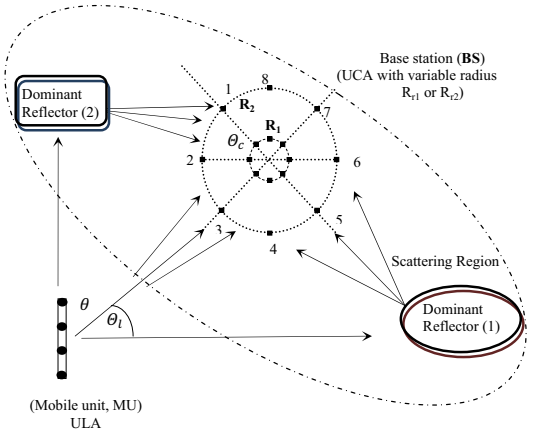

Fig. 1. Geometry of the MIMO system model of $M_t \times M_r$ elements ULA /UCA with signal arriving from multi-clusters in scattering channel**.**

As shown, (M_t) and (M_r) elements for transmit and receive arrays respectively are considered. The system is deploying ULA at MU, and a UCA or ULA at BS. The receive antenna UCA radius is assumed to be varied within the lower and upper bounds $\{R_1{:}R_2\}$. Different number of elements M_r will be considered and uniformly spaced on either ULA/UCA configurations. Consider a signal arriving at the receive array from angle of arrival θ note that $\theta_l = \frac{\pi}{2} - \Theta$. Thus, if a signal of interest can be described by the summation of signal arriving from angles with distribution $p_\Theta(\theta)$, then we know that the spatial correlation between two points a distance d apart can be determined as:

$$\rho(d) = \int_{-\pi}^{\pi} \left(e^{\frac{j2\pi d}{\lambda} \sin(\frac{\pi}{2} - \Theta)} \right) p_\Theta(\Theta) d\Theta \qquad (1)$$

For UCA this relation will be as follows

$$\rho(d) = \int_{-\pi}^{\pi} \left(e^{\frac{j2\pi R}{\lambda} \cos(\Theta - \phi)} \right) p_\Theta(\Theta) d\Theta \qquad (2)$$

where $p_\Theta(\theta)$ is considered here is any one of the distributions for multi-clustered Power Azimuth Spectrum (PAS), uniform, Gaussian and Laplacian [2], taking into account the unbalanced power in different clusters. In this paper, Laplacian distribution is considered where it is the best fit to measurement results in urban and rural areas. A multiclustered Laplacian PAS can be written as:

$$p_\Theta(\Theta) = \sum_{k=1}^{N_c} K_k e^{-a|\theta - \theta_{ok}|} \qquad (3)$$

where $(-\pi + \theta_{ok} \le \theta \le \theta_{ok} + \pi)$, θ_{ok} is the cluster k mean direction of arrival (AOA), N_c is the number of clusters. $K_k = \frac{a}{1 - e^{-a\pi}}$, is the normalization factor for each cluster to make $p_\Theta(\Theta)$ a density function and a is a decay factor which is related to the angle spread (AS). For ULA, the real and imaginary parts of the receiving spatial correlation between m[th] and n[th] elements using the integral in eq. (1) are given in [2] for the three PAS distributions. Also, in [4] it is shown that receiving correlation coefficients for UCA can be expressed by solving the integral in eq. (2) and by applying truncated Laplacian distributed as

$$\boldsymbol{Re\{R_{sr}(m,n)\} = J_o(Z_c) + 4K \sum_{k=1}^{\infty} \frac{a^2(1 - e^{-a\pi})}{a^2 + 4k^2} J_{2k}(Z_c) \cos[2k(\theta + \alpha)]} \qquad (4)$$

$$Im\{\boldsymbol{R_{sr}}(\boldsymbol{m},\boldsymbol{n})\} = \\ \boldsymbol{4K}\sum_{\boldsymbol{k=0}}^{\boldsymbol{\infty}}\frac{\boldsymbol{a(1-e^{-a\pi})}}{\boldsymbol{a^2+(2k+1)^2}}\boldsymbol{J_{2k+1}}(\boldsymbol{Z_c})\,. \\ \sin\left[(\boldsymbol{2k+1})(\boldsymbol{\theta+\alpha})\right] \quad (5)$$

where Z_c is related to antenna spacing and α is the relative angle between the m^{th} and n^{th} . For the ULA transmitting side, it is assumed that the mean angle of departure θ_t is uniformly distributed over [0, 2π] that is given in [3] and it can be expressed as:

$$\boldsymbol{R_{st}}(\boldsymbol{p},\boldsymbol{q}) = \boldsymbol{J_o}\left(\boldsymbol{2\pi}\frac{\boldsymbol{(q-p)D_t}}{\boldsymbol{\lambda}}\right). \quad (6)$$

where D_t is the distance between elements p and q. The uplink spatial fading correlation $\boldsymbol{R_s}(mp,nq)$ is the spatial correlation between the link from transmit antenna (p) to receive antenna (m) and the link from transmit antenna (q) to receive antenna (n). Defining $R_{st}(p,q)$ and R_{sr} (m,n) as the spatial correlation due to the transmitter and receiver antennas respectively. Since the two links are statistically independent then the link spatial correlation can be divided into transmit part and receive part as

$$R_s(mp,nq) = R_{sr}(m,n) \times R_{st}(p,q). \quad (7)$$

The correlated Rician Fading MIMO channel Matrix, (T) with dimensions ($M_t \times M_r$) at one instance of time can be modelled as a fixed (constant, LOS) matrix and a Rayleigh (variable, NLOS) matrix.

$$T = \sqrt{\frac{K}{1+K}}\overline{H_{ric}} + \sqrt{\frac{K}{1+K}}R_r^{1/2}H_wR_t^{1/2}\,. \quad (8)$$

where H_w are zero mean and unit variance complex Gaussian random variables that presents the coefficients of the variable NLOS matrix. K is the Rician K-factor and R_r and R_t are the $M_r \times M_r$ and $M_t \times M_t$ correlation matrices that include all possible coefficients of spatial correlations between the channel links seen at transmit and receive elements respectively. Assuming equal power transmission across the array elements at the transmitter, the capacity of MIMO system can be computed from:

$$C = log_2\left[det\left(I_{Mr} + \frac{SNR}{Mt}TT^H\right)\right]. \quad (9)$$

where T is the complex matrix given from (8), SNR is the average signal to noise ratio, and I_{Mr} is the identity matrix with dimensions $M_r \times M_r$.

III. NUMERICAL RESULTS

In this section, the numerical analysis of spatial fading correlation and capacity investigations are presented for practical uplink application that is shown in Fig. 1. The impact of receiving antenna elements separation (in case of ULA) or circle radius (in case of UCA) on spatial correlations for single and two-clustered at different AoA and AS is illustrated in Figs. 2–5. Fig. 2 shows the spatial correlation $R_s(21,11)$ for 4 elements ULA receiver when the arriving signal is concentrated in single cluster, when the mean AoA, Θ= 0, 45 and 90 for two values of the variance of angular distributions, AS=2 and 20. As expected Rs decreases as D_r increases and as AS increases. The same is also observed for UCA in Fig. 3 where $R_s(21,11)$ is plotted versus the radius of 4 elements UCA. Comparing Figs. 2 and 3, it is seen that ULA experiences the lowest Rs at Θ=90 (broadside case, i.e the signal is arriving normal to array line) while the highest values is observed at the endfire case. However, for the UCA lower bound correlation curve is found to be at Θ=45, while the higher bound curves are observed at Θ= 0 and 90 having the same values. Figs. 4 and 5 show the $R_s(21,11)$ for 4 elements ULA and UCA receivers verse elements spacing and array circle radius respectively for 2 clusters case. Note that $R_s(21,11)$ and $R_s(31,41)$ are equal, since spacing and orientation between elements 1 and 2 are the same as 3 and 4. Here, AoA distribution is generated by two dominant reflectors, where signals impinge the antenna from two clusters that are assumed to be {[0, 0], [-45, 45], [-90, 90]}. R_s is computed by applying bi-modal PAS function for the laplacian distribution using eq. (3) considering N_c=2. As seen in Figs. 4 and 5 the correlation function has an oscillation term that depends on the difference between the AoA's of the two modes. As seen, the oscillation is slow for D_r versus ULA and for R versus UCA if the angles are close such as [-45, 45] case and the oscillation is faster when the two AoA's separation is large as the case of [-90, 90]. Comparing the envelope of the correlation

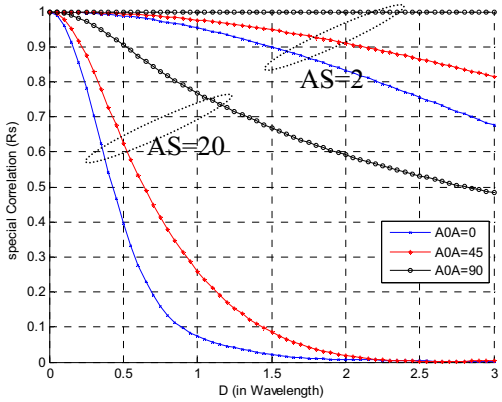

Fig. 2. Spatial correlation versus distance between elements for ULA configuration for laplacian distribution with 1 clusters have AS=20, AoA={0 45 90}.

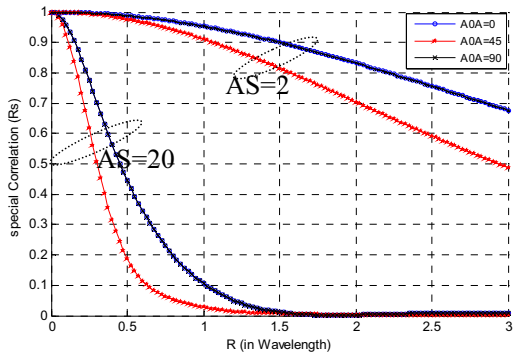

Fig. 3. Spatial correlation versus distance between elements for UCA configuration for laplacian distribution with 1 clusters have AS=2 & 20, AoA={0 45 90}.

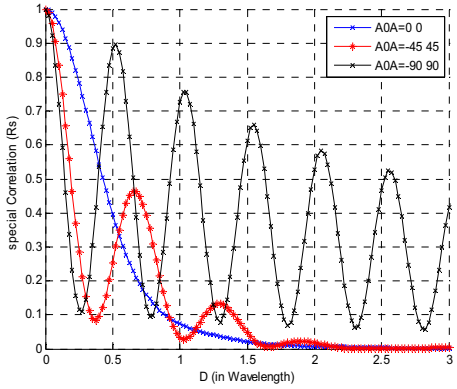

Fig. 4. Spatial correlation versus distance between elements for ULA configuration for laplacian distribution with 2 clusters have AS=20, AoA={[0 0],[-45 45],[-90 90]}.

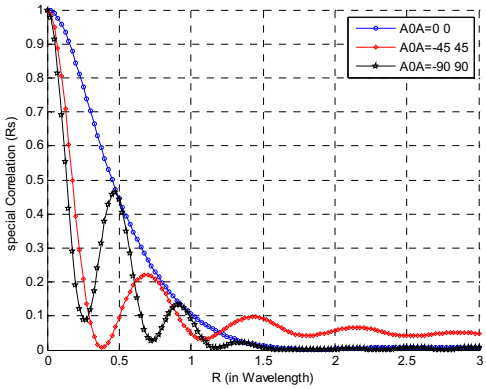

Fig. 5. Spatial correlation versus Radius of the array circle for elements(3,4) /(1,2) for UCA configuration for laplacian distribution with 2 clusters have AS=20, AoA={[0 0],[-45 45],[-90 90]}.

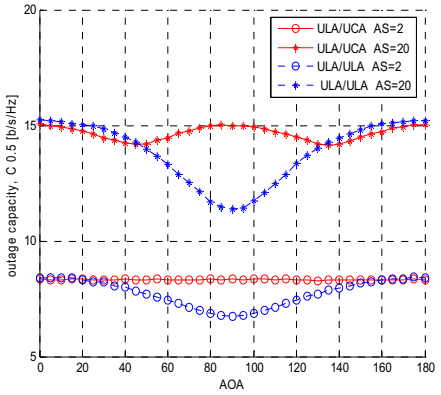

Fig. 6. Ergodic Capacity versus AoA, one cluster case, 4x4 MIMO ULA and UCA system, SNR=15 dB.

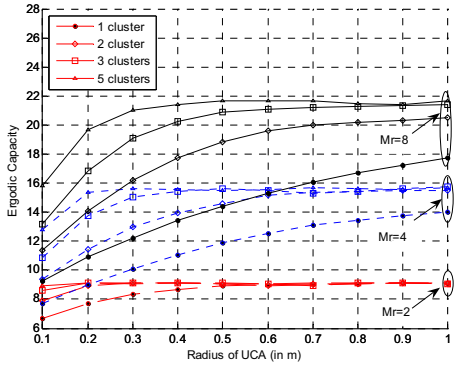

Fig. 7. Ergodic capacity versus Radius (in wavelength) of UCA for 4x M_r MIMO system, where M_r =2, 4 and 8, As=10, SNR=15 dB.

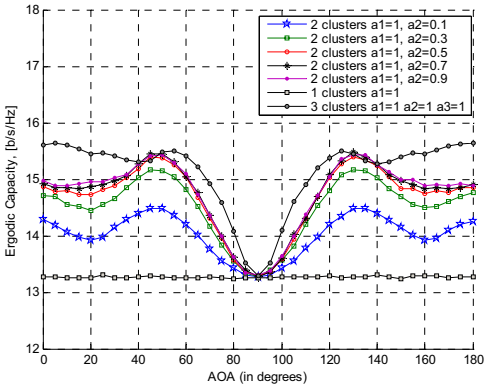

Fig. 8. Ergodic Capacity versus AoA, for 4x4 MIMO system UCA with AS=10 and SNR =15 dB. 1, 2 and 3 clusters, 1 cluster AoA=90, 2 clusters AoA={90, ϕ}, 3 clusters={0+ϕ, 90, 180-ϕ}.

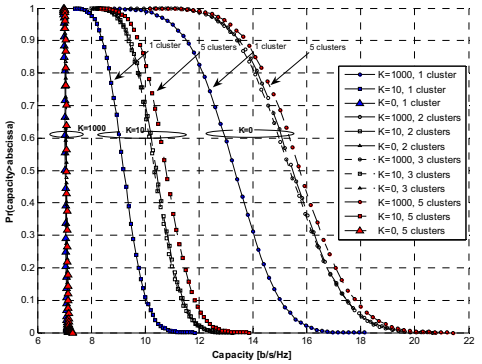

Fig. 9. Complementary CDF of the capacities of single and multi-clusters 4x4 MIMO cases, at different *K*-factor [0,10,1000] and SNR= 15dB, AS=10.

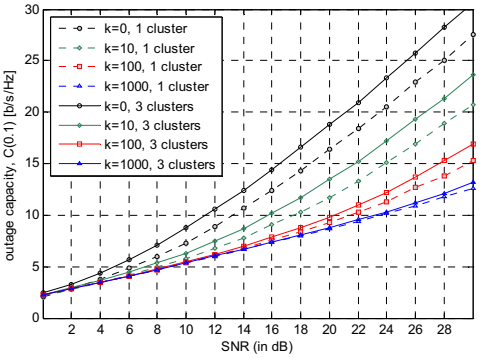

Fig. 10. Capacity vs. SNR for single and 3-clusters 4x4 MIMO cases, at different K-factor [0,10,1000], AS=10.

function for both configurations with two clusters in Figs. 4 and 5 it can be seen that the envelope correlation R_s has lower values for UCA when compared to the ULA values. Next, Figs. 6–8 present capacity investigations for both ULA and UCA in single and multi-clustered for various number of elements, spacing between elements, AoA's and AS. Fig. 6 shows the ergodic capacity of the UCA and the ULA at the receiver as function of Θ_l and Θ_c (AoA). These results are performed for 4×4 MIMO system and for 10,000 channel realizations.

For a fair comparison between the two geometries, aperture size should be made the same (i.e. diameter of UCA = length of ULA). Thus, for ULA spacing D_r =0.5λ, the UCA radius is assumed to be R=0.75λ. Note that the elements are distributed evenly over both arrays. In this figure, capacity is investigated for AS = 2 (low) and AS=20 (high) while SNR is fixed at 15 dB for the two cases. As shown, the UCA outperforms the ULA in particular for small angle spread at endfire (Θ_l=90°). However, the ULA has nearly the same performance as UCA for certain angles-of-arrival (e.g., near broadside of the ULA $\Theta_l = 0^o$ and 180^o). It is also noted that the UCA has its lowest capacity at Θ_c=45° and 135° since in these two case two elements are directly behind and parallel to the other two elements (strongly correlated); this can be observed more at high AS.

Fig. 7 illustrates variations of ergodic capacity (at SNR=15 dB) versus variations of UCA radius in the range from {R_1=0.1λ} to {R_2=λ}. As shown in Fig. 1, this is performed for 4×M_r MIMO system, where M_r is assumed to be {2, 4 and 8} for different number of clusters {1, 2, 3 and 5} with mean AOA's {[90], [45, 90], [45, 90, 135], and [0, 45, 90, 135, 180]} respectively. All clusters are assumed to have AS=10. As can be seen in Fig. 6, capacity increases as radius of the UCA increases where the elements experience lower correlation. Also, higher capacity is observed when more clusters are included in the model. This effect increases as the number of elements increases, and this is clear when comparing curves for 2, 4 and 8 elements. It is also seen that for the 5 cluster model the capacity reaches its maximum and becomes stable at radius R_c=0.2λ, 0.3λ and 0.5λ for 2, 4 and 8 elements respectively. Thus, these curves can be used to achieve the optimum compactness for practical antennas. It is also noted that when R_c < 0.6λ the system with M_r=4 elements has higher capacity values when including multi-clusters (2, 3 and 5) more than

the M_r=8 system that is modeled assuming one cluster. These results show the impact of multi-cluster modeling on the design of compact antenna arrays with optimum system capacity.

Other multi-clusters scenarios are presented in Fig. 8 to investigate capacity for signals arriving at multi-clusters with different AOA's and different amplitudes. Assuming the signals impinge at a relative mean AoA at Θ_c={90°} for the single cluster case, Θ_c ={90, ϕ} and with PAS amplitudes equal {a1, a2} for the two cluster case and Θ_c={0+ϕ, 90, 180-ϕ} with PAS amplitudes equal {a1, a2, a3} respectively for three cluster case, ϕ is varied in the range [0°:180°]. The capacities for the three cases are plotted versus ϕ at AS=10 and SNR=15 dB. As can be seen, in general, the capacity increases for 2 and 3 clusters cases compared to 1 cluster case. The capacity of the 2nd clusters case increases as ϕ gets further from 90° (the mean AOA of the 1st cluster). It is noted that the 2 and 3 clusters capacity curves have oscillations across the AOA values (due to the oscillations of the spatial correlation function). Also, envelopes for 2 cluster cases curves increases as the relative amplitude of the PAS of the 2nd cluster (a2) increases from 0.1 to 0.9. It is found that the 3 clusters case with equal PAS amplitudes, is an upper bound of the 1 and 2 clusters cases with highest capacity when mean AOAs at {0, 90, 180}. Capacity of MIMO systems employing UCA at the receiver in Rician fading channels is analyzed with multi-clustered approach and presented in Figs. 9 and 10. Fig. 9 plots complementary cumulative distribution function (c.c.d.f.) of the capacities of 4×4 MIMO cases for different Rician distribution K-factor {0, 10, 1000}. For each K factor value the capacity is computed for 1, 2, 3 and 5 clusters assuming the corresponding mean AOA's are {[90], [45, 90], [45, 90, 135], and [0, 45, 90, 135, 180]} respectively. The simulation parameters are AS=10, SNR = 15 dB and 10,000 channel implementations. As shown, increasing the K factor reduces the capacity of the system. This is because the increase in K emphasizes the deterministic part of the channel in eq. (8) and increases the impact of LOS component existence that is not preferable for MIMO systems. It is also observed that for multi-cluster propagations capacity increases as number of clusters increase especially for K=0 (Rayleigh fading) and low K factor values with the slopes of c.c.d.f. curves increases as K factor increases. Also, it can be seen that the impact of multi-cluster propagations on capacity is reduced as K factor increases as the difference between c.c.d.f. curves decreases and it becomes overlapped for K=1000 (Gaussian propagation case). Similar observations are obtained from Fig. 10 that present 0.1 outage capacity ($C_{0.1}$) against SNR. As expected, capacities increase linearly with SNR. Highest capacity curve is obtained K=0 and number of clusters =3 and lowest capacity curve is the one for K=1000 with single cluster. The effect of K can be considered as an equivalent loss or gain in the SNR for a given fixed capacity. For example, assume single cluster MIMO system is required to have $C_{0.1}$=15 b/s/Hz with K=1000 then SNR=16 is required. However, the same outage capacity can be achieved for K=10 channel with SNR=28. This means that 14 dB SNR losses get the same MIMO system capacity at different fading channels K=10 and 1000.

IV. CONCLUSION

Simulating realistic correlated MIMO channel that is essential to predict the performance of real MIMO systems was the objective of this paper. Thus, the spatial fading correlation and the channel capacity of a $M_t \times M_r$ MIMO system using multi-clustered statistical clustered channel model are investigated. Results are presented for various hybrid ULA/UCA antenna configurations at different channel assumptions. Uniformly spaced linear and circular arrays are compared showing that UCA outperforms ULA on average for the same aperture size. It is discussed that the system with less number of elements could have a higher capacity values when including multi-clusters than systems with higher number of elements that is modeled assuming one cluster. It is concluded that multi-cluster based approach should be considered when performing capacity investigations as it gives more accurate results than the single cluster case. This could lead to more optimum designs in the search for compact antennas. Results show that the central AOA's of the multi-clusters can have a significant impact on the capacity performance. Also, it is shown that Rician fading reduces the capacity gains in comparison to the fully scattering Rayleigh fading where the *K* factor effect on the capacity can be considered as SNR loss or gain. Multi-cluster propagations capacity increases as number of clusters increases for low *K* (Rician) and *K*=0 (Rayleigh) channels. Finally, the paper

shows the impact of multi-cluster propagations on capacity is reduced as *K* factor increases.

REFERENCES

[1] A. J. Paulraj, D. Gore, R. U. Nabar and H. Bolcskei, "An overview of MIMO communications–A key to gigabit wireless", *Proceedings of the IEEE,* vol. 92, no. 2, pp. 198-218, Feb. 2004.

[2] L. Schumacher, K. I. Pedersen and P. E. Mogensen, "From antenna spacings to theoretical capacities - guidelines for simulating MIMO systems", *The 13th IEEE International Symposium on Personal, Indoor and Mobile Radio Communications*, vol. 2, pp. 587-592, 2002.

[3] U.A. Waheed and D.V. Kishore, "Uplink spatial fading correlation of MIMO channel", *58th IEEE Vehicular Technology Conference,* VTC 2003, vol. 1., pp. 94-98, 2003.

[4] J. Tsai and B. D. Woerner, "The fading correlation of a circular Antenna Array in Mobile Radio enviroment", *IEEE Global Telecommunications Conference,* vol. 5, pp. 3232-3236, 2001.

[5] L. Xin and N. Zai-ping, "Spatial fading correlation of circular antenna arrays with Laplacian PAS in MIMO channels" *IEEE Antennas and Propagation Society International Symposium*, vol. 4, pp. 3697-3700, 2004.

[6] A. Forenza, D. J. Love, and R. W. Heath, "Simplified Spatial Correlation Models for Clustered MIMO Channels With Different Array Configurations" *IEEE Transactions on Vehicular Technology,* vol. 56, no. 4 part 2, pp: 1924-1934, July 2007.

[7] J. P. Kermoal, L. Schumacher, K. I. Pedersen, P. E. Mogensen, and F. Frederiksen, "A stochastic MIMO radio channel model with experimental validation", *IEEE Journal of Selected Areas in Communications,* vol. 20, no. 6, pp. 1211-1226, Aug. 2002.

[8] P. J. Smith and L. M. Grath, "Exact capacity distribution for dual MIMO systems in Ricean fading", *IEEE Communications Letters*, vol. 8, no. 1, pp. 18-20, Jan. 2004.

Dr. Mohab A. Mangoud received his B.S. and M.S. in Electrical Engineering from the Alexandria University, Egypt in 1993 and 1996, respectively. He received his Ph.D degree from University of Bradford, UK in 2001. Later in 2001, He was Senior RF Engineer for EADS -Astrium (formally Matra Marconi Space Lmt.) Hertfordshire, UK, with a space and commercial communications satellites group. From 2002 till 2007, he was Assistant Professor with Electronics and communications Engineering Department, Arab Academy for Science and Technology (AAST) Alexandria, Egypt. In 2006, Dr. Mangoud was Adjunct Professor with The Bradley Department of Electrical & Computer Engineering, Virginia Polytechnic Institute and State University (Virginia Tech.), Blacksburg, Virginia, USA. He is currently Associate Professor of Wireless Communications, Department of Electrical and Electronics Engineering, University of Bahrain, Bahrain. Dr. Mangoud has been a member of the IEEE since 1998. He was a treasurer of Alexandria/Egypt IEEE Subsection in 2003. His current research interests include: space-time MIMO wireless communication systems, optimization techniques for antenna design applications and numerical electromagnetic methods.

Parallelization of MLFMA with Composite Load Partition Criteria and Asynchronous Communication

Huapeng Zhao [1,2], Jun Hu [1], and Zaiping Nie [1]

[1] Department of Microwave Engineering
University of Electronic Science and Technology of China, Chengdu 610054, China

[2] School of Electrical and Electronic Engineering
Nanyang Technological University, 50 Nanyang Avenue, Singapore, 639798
huapengzhao@uestc.edu.cn

***Abstract*—** This paper describes an efficient parallelization of the multi-level fast multi-pole algorithm (MLFMA) for fast solution of very large scale electromagnetic scattering problems. Computation in the MLFMA can be divided into several stages. To accomplish load balance at any time, load partition criteria are adjusted according to different features of every phase. Meanwhile, an asynchronous communication method is designed to overlap the communication with computation and thus the communication cost in parallelization is reduced. Numerical results show that good parallel efficiency is obtained in the presented parallelization of MLFMA. With our parallel MLFMA, a scattering problem with nearly 5, 300, 000 unknowns is solved in about six hours using 8 CPUs on SGI O350 server.

***Index Terms*—**Large scale scattering problem, Parallel multi-level fast multi-pole algorithm.

I. INTRODUCTION

The multi-level fast multi-pole algorithm (MLFMA) [1] obtains computational and storing complexity of $O(N \log(N))$, where N is the number of unknowns. The low complexity of MLFMA makes it possible to solve large scale scattering problems on a single PC. The challenges in integral equation methods are to further improve the efficiency and solve very large scale problems quickly. Therefore, optimizing techniques for MLFMA were designed, and variants of MLFMA were developed as well. These improved the performance of MLFMA greatly and were well documented in [2]–[6]. However, before the application of parallel technique, the solution of very large scale problems was still a challenge due to its requirement for huge computing resource. Offering strong computing ability and huge storing space, parallel technique is widely used for efficient solution of large scale electromagnetic problems [7]–[11]. With a parallel MLFMA (PMLFMA), Chew et al. [7] solved problems with ten millions unknowns, and they reported performance analysis of their parallelization in [8].

As several different computing stages are involved in MLFMA, it's hard to obtain a high parallel efficiency without careful design of load partition. This paper presents a composite load partition method, where load distributing criteria are adjusted according to the features of every computation stage. In that way, the computing and storing load balance is ensured at any time. To reduce the communication cost, an asynchronous communication method is designed so that the communication is overlapped with computation and time spent on communication is reduced. Numerical results show that the proposed parallel method can achieve good parallel efficiency and has strong ability to solve very large scale problems quickly and accurately. With our PMLFMA, a scattering problem with nearly 5, 300, 000 unknowns was solved on SGI O350 supercomputer.

The rest of this paper is organized as follows. A brief review of MLFMA is given in Section II. After that, load partition criteria

and communication management in our parallelization method are described in Section III. Numerical results are given in Section IV and finally conclusions are made in Section V.

II. BRIEF REVIEW OF MLFMA

Consider the electric field integral equation (EFIE) for conducting objects:

$$\hat{t}(\mathbf{r}) \cdot \int_S \overline{\mathbf{G}}(\mathbf{r},\mathbf{r}') \cdot \mathbf{J}(\mathbf{r}') dS' = \frac{4\pi i}{k\eta} \hat{t}(\mathbf{r}) \cdot \mathbf{E}^{inc}(\mathbf{r}), \tag{1}$$

where S is the surface of the object, and $\mathbf{r}$ and $\mathbf{r}'$ are the observing and source points on S, respectively. $\overline{\mathbf{G}}$ is the dyadic Green's function and $\mathbf{J}$ represents the current density. $\hat{t}(\mathbf{r})$ is the unit vector tangential to S at $\mathbf{r}$ and η is the free space characteristic impedance. $\mathbf{E}^{inc}$ is the incident electric field. Adopting proper expansion basis and invoking some kind of matching process [12], equation (1) can be discretized into a matrix equation

$$\sum_{l=1}^{N} A_{jl} a_l = b_j, \quad j = 1,2,3...,N, \tag{2}$$

where A_{jl} is the interaction impedance between the jth and the lth bases, a_l is the lth unknown expansion coefficient for the current density, and b_j is computed from $\mathbf{E}^{inc}$. In our PMLFMA, the curvilinear RWG basis [13] and Galerkin's matching process are used. Applying vector addition theorem, the dyadic Green's function in equation (1) can be expanded as

$$\overline{\mathbf{G}}(\mathbf{r}_j,\mathbf{r}_l) = \frac{ik}{4\pi} \int d^2\hat{\mathbf{k}} (\bar{\mathbf{I}} - \hat{\mathbf{k}}\hat{\mathbf{k}}) e^{i\hat{\mathbf{k}}\cdot(\mathbf{r}_{jm} - \mathbf{r}_{lm'})} \cdot \alpha_{mm'}(\mathbf{r}_{mm'} \cdot \hat{\mathbf{k}}), \quad |\mathbf{r}_{mm'}| > |\mathbf{r}_{jm} - \mathbf{r}_{lm'}|, \tag{3}$$

where $\mathbf{r}_j$ and $\mathbf{r}_l$ are position vectors of the observing point and source point, $\mathbf{r}_m$ and $\mathbf{r}_{m'}$ are position vectors of the field group and source group centers, respectively. $\mathbf{r}_{jm}$ is the vector connecting $\mathbf{r}_j$ and $\mathbf{r}_m$, and the same definition applies for $\mathbf{r}_{jm}$, $\mathbf{r}_{lm'}$, and $\mathbf{r}_{mm'}$. $\alpha_{mm'}$ is termed as the translator, whose definition and expression can be found in [1]. In fast multi-pole method (FMM), the left hand side of equation (2) is expressed as the sum of two terms, which are

$$\sum_{l=1}^{N} A_{jl} a_l = \sum_{m' \in NG} \sum_{l \in G_{m'}} A_{jl} a_l + \frac{ik}{4\pi} \int d^2\hat{\mathbf{k}} \mathbf{V}_{fmj}(\hat{\mathbf{k}}) \cdot \sum_{m' \in FG} \alpha_{mm'}(\hat{\mathbf{k}} \cdot \mathbf{r}_{mm'}) \sum_{l \in G_{m'}} \mathbf{V}^*_{sm'l}(\hat{\mathbf{k}}) a_l, \quad j \in G_m, \tag{4}$$

where $\mathbf{V}_{sm'l}(\hat{\mathbf{k}})$ and $\mathbf{V}_{fmj}(\hat{\mathbf{k}})$ are named as the aggregation and disaggregation, respectively, whose expressions can be found in [1]. *NG* and *FG* represent the near region groups and far region groups, respectively, and G_m is the mth group. For convenience, equation (4) is written in matrix form as

$$\overline{\mathbf{A}} \cdot \mathbf{a} = \overline{\mathbf{A}}_{near} \cdot \mathbf{a} + \overline{\mathbf{U}} \cdot \overline{\mathbf{T}} \cdot \overline{\mathbf{V}} \cdot \mathbf{a}, \tag{5}$$

where $\overline{\mathbf{A}}_{near}$, $\overline{\mathbf{U}}$, $\overline{\mathbf{T}}$ and $\overline{\mathbf{V}}$ represent the near group interaction matrix, aggregation matrix, translation matrix and disaggregation matrix, respectively, and $\mathbf{a}$ is the vector consisting of the unknown current expansion coefficients. The MLFMA is generalization of FMM in a multi-level structure, where equation (5) can be rewritten as

$$\overline{\mathbf{A}} \cdot \mathbf{a} = \overline{\mathbf{A}}_{near} \cdot \mathbf{a} + \overline{\mathbf{U}}_{NL} \cdot \overline{\mathbf{T}}_{NL} \cdot \overline{\mathbf{V}}_{NL} \cdot \mathbf{a} + \sum_{l=2}^{NL-1} \overline{\mathbf{U}}_l \cdot \overline{\mathbf{T}}_l \cdot \overline{\mathbf{V}}_l \cdot \mathbf{a}, \tag{6}$$

where $\overline{\mathbf{V}}_l$, $\overline{\mathbf{T}}_l$, and $\overline{\mathbf{U}}_l$ are the aggregation matrix, translation matrix and disaggregation matrix in the lth level, respectively. *NL* is the total number of levels used in MLFMA. $\overline{\mathbf{V}}_l$ and $\overline{\mathbf{U}}_l$ are computed by interpolation for $l <$ *NL*. $\overline{\mathbf{T}}_l$ can be obtained either by real-time computation or from the pre-filled matrix [5]. Given a problem with N unknowns, MLFMA obtains the computing and storing complexity of $O(N \log N)$.

III. PARALLEL MLFMA

To solve scattering problems using MLFMA, the following steps are involved: (1). Filling of $\overline{\mathbf{A}}_{near}$; (2). Computation of $\overline{\mathbf{U}}_{NL}$ and $\overline{\mathbf{V}}_{NL}$; (3). Implementation of matrix vector multiplication using equation (6), including upward pass, translation stage, downward pass and direct matrix vector multiplication. For convenience, terms defined in [8] have been

followed in our paper and more details about these terms can be found in [8]. To achieve good load balance at any time, the load partition criteria should be adjusted according to features of the above computing stages. Section III-A describes the load partition criteria at every computation stage. For some stages, load partition will introduce indispensable communication, which is managed with an asynchronous communication method described in section III-B.

A. Load Partition Criteria

This section mainly discusses the problem of load balance. The total number of processes is assumed to be p.

a) Filling of $\overline{\mathbf{A}}_{near}$: As long as numbers of interaction elements are equal on all processes, the computation and storage load will be balanced at this stage. The matrix $\overline{\mathbf{A}}_{near}$ is constituted by the self group and near group interaction elements, which are computed group by group and list by list, respectively. Assume the total number of interaction elements is Z_{count}, the number of self group interaction elements assigned on process l is Z_{self}^{l} and the number of non-self group interaction elements to be allotted is Z_{nself}^{l}. Since the non-empty groups are distributed uniformly among the p processes, Z_{self}^{l} s on all processes are fixed. However, Z_{self}^{l} s on p process are different from each other, because numbers of basis functions enclosed by different groups are different. To ensure total numbers of interaction elements are equal on all processes, the near group lists are distributed from process 1 to $p-1$ abiding by the criteria that $Z_{self}^{l}+Z_{nself}^{l}$ approximately equals Z_{count}/p $(1\le l\le p-1)$. Then the rest near group lists are assigned to process p and $Z_{self}^{p}+Z_{nself}^{p}$ will approximately equal Z_{count}/p automatically.

b) Computation of $\overline{\mathbf{U}}_{NL}$ and $\overline{\mathbf{V}}_{NL}$: $\overline{\mathbf{U}}_{NL}$ and $\overline{\mathbf{V}}_{NL}$ are the receiving and radio patterns of the basis functions. A simple and effective partition method is to distribute the basis functions equally among p processes. However, this may make the basis functions belonging to the same group be distributed on different processes, which will introduce a mass of communications in the aggregation and disaggregation phase. Therefore, according to [14], the basis functions are first ordered by their Morton Key values and then distributed equally to the p processes, so that the communication cost is minimized.

c) Upward and Downward phase: A simple parallelizing method for these two stages is to construct an independent tree structure on every process according to distribution of basis functions. This method introduces no communication, but load on the p processes may be unequal, because numbers of boxes on all processes may be different. Another disadvantage of this partition method is that the inner and outer waves of one group may be repeatedly stored on two or more processes, which obviously wastes the memory.

Since computation is conducted group by group in every level during these two stages, groups in all levels should be distributed equally among the p processes, and then the load on all processes will be equal. Since a parent group and its child groups may be distributed on different processes, this partition method will introduce indispensable communication, which will be approached with the asynchronous communication method described in Section III-B.

d) Translation Phase: The computing unit at this phase is the far group list. The load balance is easily implemented by distributing all the far group lists equally among the p processes. However, two boxes belonging to a far list may be stored on different processes. Communication is therefore needed to accomplish the translation phase, which will be discussed in Section III-B.

e) Direct Matrix Vector Multiplication: As long as the numbers of near group interaction elements on all the processes are equal, the computing load in this stage is balanced. Therefore, load balance for this

stage is realized at the stage of filling $\overline{\mathbf{A}}_{near}$.

B. Communication Management

As discussed in Section III-A, communication is required in upward, downward and translation phases. The boxes and far lists which need communication are defined as non-local boxes and lists, while those need no communication are defined as local boxes and lists. To reduce the communication cost, an asynchronous communication method is designed. Asynchronous communication is non-block communication. The term non-block means the communication doesn't block the computation. Assuming in one communication, process *m* needs the information on process *n*, communication in our PMLFMA is conducted as follows: process *m* sends a request to process *n* and then continues the computation requiring no nonlocal information. Once process *n* detects the request from process *m*, it sends the requested information by starting an asynchronous communication and then continues its own computation. The above communication method can be demonstrated using Fig. 1, which shows that the communication is overlapped with computation. This flow chart is applicable to all the stages discussed in section III-A, just by substituting the corresponding computation module into the flow chart. Specific flow chart for every phase is hence omitted here for simplicity. For the detection, send and request actions in Fig. 1, one can implement them with corresponding message passing interface functions.

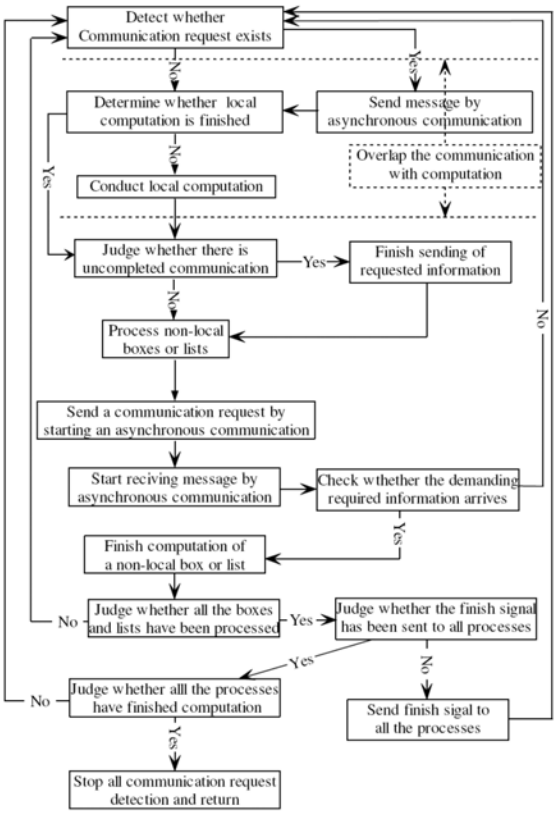

Fig. 1. Flow chart of the asynchronous communication method.

IV. NUMERICAL RESULTS

In all the simulations of this section, the group size of the finest level is set to be 0.3λ. To investigate the parallel efficiency of the proposed parallel scheme, two simulations are conducted on SGI O350 server. The parallel efficiency η is computed as

$$\eta = T_1 / T_p / p \times 100\%, \qquad (7)$$

where p is the number of processes, T_1 is the solving time using one process and T_p is the solving time using p processes.

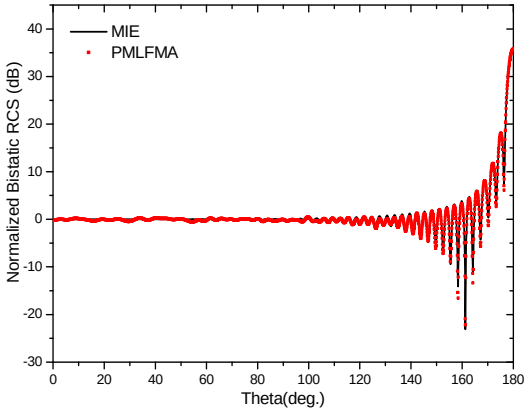

Fig. 2. Normalized bistatic RCS of a 20λ diameter conducting sphere.

First, the bistatic radar cross section (RCS) of a 20λ diameter conducting sphere is solved. The number of unknowns is about 0.2 million. A six-level MLFMA is used. The numerical result and parallel efficiency are shown in Fig. 2 and Fig. 3, respectively. In Fig. 3, it is seen that the parallel efficiency with eight processes is more than 80%. It is also shown that the parallel efficiency decreases as the number of processes increases. This is

because more communication is introduced as the number of processes increases. However, the proposed parallel scheme can still obtain a parallel efficiency of 70% when the number of processes increases to 10.

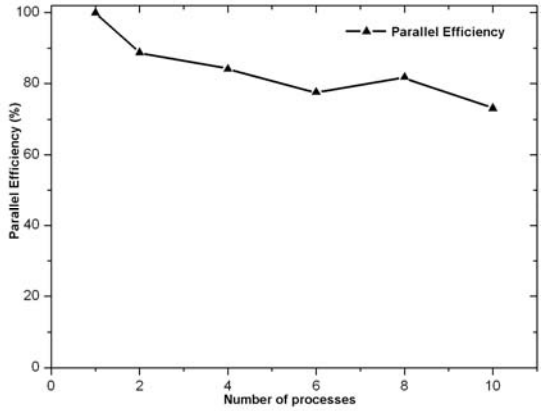

Fig. 3. Parallel efficiency for solving bistatic RCS of a 20λ diameter conducting sphere.

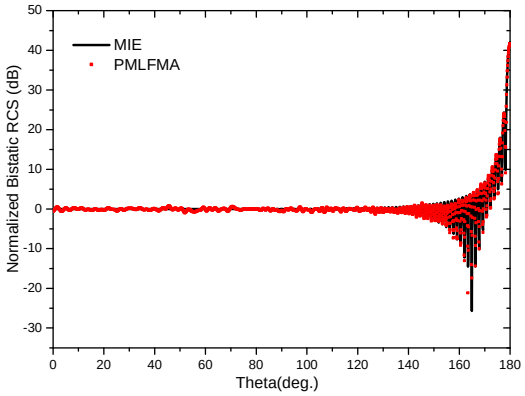

Fig. 4. Normalized bistatic RCS of a 40λ diameter conducting sphere.

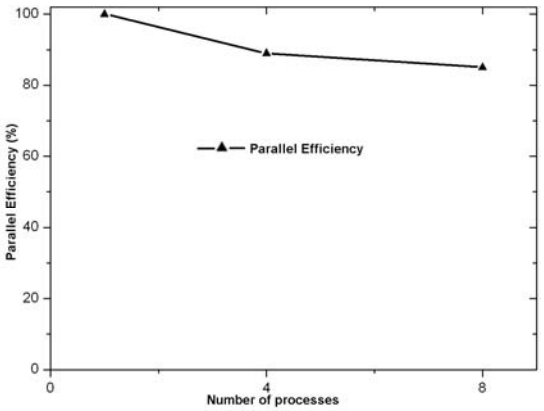

Fig. 5. Parallel efficiency for solving bistatic RCS of 40λ diameter conducting sphere.

Second, the problem scale is enlarged. The object is a 40λ diameter conducting sphere. The number of unknowns is about 1.8 million, and a six-level MLFMA is used. Fig. 4 and Fig. 5 show the numerical result and parallel efficiency, respectively. Compared with Fig. 3, Fig. 5 shows a higher parallel efficiency, which means that the parallel efficiency increases as the problem scale increases. Therefore, the proposed parallel scheme is scalable.

The reported parallel efficiency is not as high as that of Chew's group [8] for the following two reasons. First and most important, the translation phase is not well managed in our parallelization. In the translation phase, Chew's group achieved load balance by partitioning the far-field patterns equally among all processors for coarse levels, communication is therefore totally avoided in the translation phase for coarse levels. However, in our parallelization, mass communication is introduced in the translation phase to ensure load balance, especially for the coarse levels. Nevertheless, with the designed asynchronous communication method, our parallelization still obtains good parallel efficiency, which justifies the

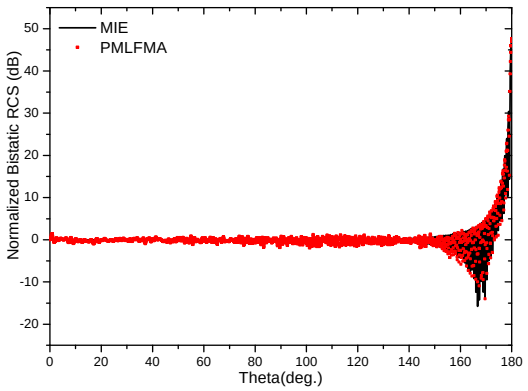

Fig. 6. Normalized bistatic RCS of a 100λ diameter conducting sphere.

effectiveness of our communication method. The second reason might be differences between platforms. In the SGI Origin 2000 supercomputer adopted in [8], each processor has a clock speed of 250 MHz. In our supercomputer, the clock speed of each processor is of 1 GHz. If communication cost is given, parallel efficiency will be higher in systems with lower clock speed.

Finally, using the proposed PMLFMA, the

bistatic RCS of a 100λ diameter conducting sphere is solved with 5,287,752 unknowns on SGI O350 supercomputer. For this simulation, a nine-level MLFMA is used. It takes 8 CPUs 22147 seconds to solve this problem. This simulation demonstrates the ability of our PMLFMA in solving very large scale problems.

V. CONCLUSIONS

This paper presented an efficient parallel scheme for MLFMA. Composite load partition criteria have been designed to achieve load balance at any time and an asynchronous communication method has been developed to reduce the communication cost. Numerical results show the good parallel efficiency achieved by the proposed parallel scheme. With our PMLFMA, a scattering problem with about 5.3 million unknowns has been solved, demonstrating its ability in solving very large scale problems. Our future work is to improve the load partition for the translation phase in coarse levels so that higher parallel efficiency can be achieved.

ACKNOWLEDGEMENT

This work is supported partly by NSFC (No. 60601008), research funding (No. 9140A0301 0708DZ0235, 9140A07030109DZ02), and the Programme of Introducing Talents of Discipline to Universities under Grant b07046.

REFERENCES

[1] J. Song and W. Chew, "Multilevel fast-multipole algorithm for solving combined field integral equations of electromagnetic scattering," *Microwave and Optical Tech. Lett.,* vol. 10, no. 1, pp. 14-19, Sept. 1995.

[2] W. Chew, T. Cui and J. Song, "A FAFFA-MLFMA algorithm for electromagnetic scattering," IEEE *Transactionas on Antennas and Propagation,* vol. 50, no. 11, pp. 1641-1649, Nov. 2002.

[3] T. Cui, W. Chew and G. Chen et al., "Efficient MLFMA, RPFMA, and FAFFA algorithms for EM scattering by very large structures," *IEEE Transactions on Antennas and Propagation,* vol. 52, no. 3, pp. 759-770, Mar. 2004.

[4] J. Hu and Z. Nie et al., "Fast solution of scattering from conducting structures by local MLFMA based on improved electric field integral equation," *IEEE Transactions on Electromagnetic Compatibility,* vol. 50, no. 4, pp. 940-945, Nov. 2008.

[5] S. Velamparambil and W. Chew, "A fast polynomial representation for the translation operators of an MLFMA," *Microwave and Optical Tech. Lett.*, vol. 28, no. 5, pp. 298-303, Mar. 2001.

[6] H. Zhao, J. Hu and Z. Nie, "Block storing method for efficient storage of near group impedance in MLFMA," *Electronics Letters*, vol. 44, no. 20, pp. 1171-1173, Sept. 2008.

[7] S. Velamparambil, W. Chew and J. Song, "10 million unknowns: is it that big?" *IEEE Antennas and Propag. Mag.* vol. 45, no. 2, pp. 43-58, Apr. 2003.

[8] S. Velamparambil and W. Chew, "Analysis and performance of a distributed memory multilevel fast multipole algorithm," *IEEE Transactions on Antennas and Propagation* vol. 53, no. 8, pp. 2719-2727, Aug. 2005.

[9] I. Gonzalez, E. Garcia, F. S. de Adana and M. F. Catedra, "MONURBS: A parallelized fast multipole multilevel code for analyzing complex bodies modeled by NURBS surfaces," *Applied Computational Electromagnetics Society Journal*, vol. 23, no. 2, pp. 134-142, June 2008.

[10] T. Iwashita, M. Shimasaki and J. Lu, "Parallel ICCG solvers for a finite element eddy-current analysis on heterogeneous parallel computation environment," *Applied Computational Electromagnetics Society Journal*, vol. 22, no. 2, pp. 195-200, July 2007.

[11] W. R. Dearholt and S. P. Castillo, "Electromagnetic scattering problems utilizing a direct, parallel solver," *Applied Computational Electromagnetics Society Journal,* vol. 22, no. 3, pp. 395-413, Nov. 2007.

[12] R. F. Harrington, *Field computation by Moment Methods*, Robert E. Krieger, FL, 1968.

[13] J. Hu, Z. Nie and X. Gong, "Solving electromagnetic scattering and radiation by FMM with curvilinear RWG basis," *Chinese Journal of Electronics*, vol. 12, no. 3, pp. 457-460, July 2003.

[14] J. Dull, K. Gallivan, J. Song and W.

Chew, "Parallel fast multipole capacitance solver," IEEE Antennas and Propagation Symp., Atlanta, June 1998.

Huapeng Zhao was born in Hebei province, China, in 1983. He received the B.E. and M. Eng. degrees in electronic engineering from the University of Electronic Science and Technology of China, Chengdu, China, in July 2004 and March 2007, respectively. He is now working towards his Ph.D. degree in the School of Electrical and Electronic Engineering, Nanyang Technological University, Singapore. His research interests include numerical methods and electromagnetic measurements.

Jun Hu received the B.S., M.S., and Ph.D. degrees in electromagnetic field and microwave technique from the Department of Microwave Engineering, University of Electronic Science and Technology of China (UESTC), Chengdu, China, in 1995, 1998, and 2000, respectively.

During 2001, he was a Research Assistant in the Center of Wireless Communication, City University of Hong Kong. He is currently a Full Professor in the School of Electronic Engineering, UESTC. He is the author or coauthor of more than 100 technical papers. His current research interests include computational electromagnetics, electromagnetic scattering and radiation, and electromagnetic compatibility.

Zaiping Nie received the B.S. degree in radar engineering and M.S. degree in electromagnetic field and microwave technique from Chengdu Radio Engineering Institute, now University of Electronic Science and Technology of China (UESTC), Chengdu, China, in 1968 and 1981, respectively.

From 1987 to 1989, he was a visiting scholar in the Electromagnetic Laboratory, University of Illinois, Urban Champagne. He is currently a Full Professor in the School of Electronic Engineering, UESTC. He is the author or coauthor of more than 300 technical papers. His current research interests include antenna theory and technique, field and wave in inhomogeneous media, computational electromagnetics, electromagnetic scattering, and inverse scattering.

2010 INSTITUTIONAL MEMBERS

DTIC-OCP LIBRARY
8725 John J. Kingman Rd, Ste 0944
Fort Belvoir, VA 22060-6218

AUSTRALIAN DEFENCE LIBRARY
Northcott Drive
Canberra, A.C.T. 2600 Australia

BEIJING BOOK CO, INC
701 E Linden Avenue
Linden, NJ 07036-2495

BUCKNELL UNIVERSITY
69 Coleman Hall Road
Lewisburg, PA 17837

ROBERT J. BURKHOLDER
OHIO STATE UNIVERSITY
1320 Kinnear Road
Columbus, OH 43212

DARTMOUTH COLLEGE
6025 Baker/Berry Library
Hanover, NH 03755-3560

DSTO EDINBURGH
AU/33851-AP, PO Box 830470
Birmingham, AL 35283

SIMEON J. EARL – BAE SYSTEMS
W432A, Warton Aerodome
Preston, Lancs., UK PR4 1AX

ELLEDIEMME
Libri Dal Mondo
PO Box 69/Poste S. Silvestro
Rome, Italy 00187

ENGINEERING INFORMATION, INC
PO Box 543
Amsterdam, Netherlands 1000 Am

ETSE TELECOMUNICACION
Biblioteca, Campus Lagoas
Vigo, 36200 Spain

OLA FORSLUND
SAAB MICROWAVE SYSTEMS
Nettovagen 6
Jarfalla, Sweden SE-17588

GEORGIA TECH LIBRARY
225 North Avenue, NW
Atlanta, GA 30332-0001

HRL LABS, RESEARCH LIBRARY
3011 Malibu Canyon
Malibu, CA 90265

IEE INSPEC
Michael Faraday House
6 Hills Way
Stevenage, Herts UK SG1 2AY

IND CANTABRIA
PO Box 830470
Birmingham, AL 35283

INSTITUTE FOR SCIENTIFIC INFO.
Publication Processing Dept.
3501 Market St.
Philadelphia, PA 19104-3302

KUWAIT UNIVERSITY
Postfach/po box 432
Basel, Switzerland 4900

LIBRARY – DRDC OTTAWA
3701 Carling Avenue
Ottawa, Ontario, Canada K1A OZ4

LIBRARY of CONGRESS
Reg. Of Copyrights
Attn: 407 Deposits
Washington DC, 20559

LINDA HALL LIBRARY
5109 Cherry Street
Kansas City, MO 64110-2498

RAY MCKENZIE – TELESTRA
13/242 Exhibition Street
Melbourne, Vic, Australia 3000

MISSISSIPPI STATE UNIV LIBRARY
PO Box 9570
Mississippi State, MS 39762

MISSOURI S&T
400 W 14th Street
Rolla, MO 56409

MIT LINCOLN LABORATORY
Periodicals Library
244 Wood Street
Lexington, MA 02420

OSAMA MOHAMMED
FLORIDA INTERNATIONAL UNIV
10555 W Flagler Street
Miami, FL 33174

NAVAL POSTGRADUATE SCHOOL
Attn:J. Rozdal/411 Dyer Rd./ Rm 111
Monterey, CA 93943-5101

NDL KAGAKU
C/0 KWE-ACCESS
PO Box 300613 (JFK A/P)
Jamaica, NY 11430-0613

OVIEDO LIBRARY
PO BOX 830679
Birmingham, AL 35283

PENN STATE UNIVERSITY
126 Paterno Library
University Park, PA 16802-1808

DAVID J. PINION
1122 E PIKE STREET #1217
SEATTLE, WA 98122

KATHERINE SIAKAVARA-
ARISTOTLE UNIV OF
THESSALONIKI
Gymnasiou 8
Thessaloniki, Greece 55236

SWETS INFORMATION SERVICES
160 Ninth Avenue, Suite A
Runnemede, NJ 08078

TIB & UNIV. BIB. HANNOVER
DE/5100/G1/0001
Welfengarten 1B
Hannover, Germany 30167

UNIV OF CENTRAL FLORIDA
4000 Central Florida Boulevard
Orlando, FL 32816-8005

UNIVERSITY OF COLORADO
1720 Pleasant Street, 184 UCB
Boulder, CO 80309-0184

UNIVERSITY OF KANSAS –
WATSON
1425 Jayhawk Blvd 210S
Lawrence, KS 66045-7594

UNIVERSITY OF MISSISSIPPI
JD Williams Library
University, MS 38677-1848

UNIVERSITY LIBRARY/HKUST
CLEAR WATER BAY ROAD
KOWLOON, HONG KONG

UNIV POLIT CARTAGENA
Serv Btca Univ,
Paseo Alfonso XIII, 48
Cartagena, Spain 30203

THOMAS WEILAND
TU DARMSTADT
Schlossgartenstrasse 8
Darmstadt, Hessen, Germany 64289

STEVEN WEISS
US ARMY RESEARCH LAB
2800 Powder Mill Road
Adelphi, MD 20783

YOSHIHIDE YAMADA
NATIONAL DEFENSE ACADEMY
1-10-20 Hashirimizu
Yokosuka, Kanagawa,
Japan 239-8686

ACES COPYRIGHT FORM

This form is intended for original, previously unpublished manuscripts submitted to ACES periodicals and conference publications. The signed form, appropriately completed, MUST ACCOMPANY any paper in order to be published by ACES. PLEASE READ REVERSE SIDE OF THIS FORM FOR FURTHER DETAILS.

TITLE OF PAPER:

AUTHORS(S)

PUBLICATION TITLE/DATE:

RETURN FORM TO:

Dr. Atef Z. Elsherbeni
University of Mississippi
Dept. of Electrical Engineering
Anderson Hall Box 13
University, MS 38677 USA

PART A - COPYRIGHT TRANSFER FORM

(NOTE: Company or other forms may not be substituted for this form. U.S. Government employees whose work is not subject to copyright may so certify by signing Part B below. Authors whose work is subject to Crown Copyright may sign Part C overleaf).

The undersigned, desiring to publish the above paper in a publication of ACES, hereby transfer their copyrights in the above paper to The Applied Computational Electromagnetics Society (ACES). The undersigned hereby represents and warrants that the paper is original and that he/she is the author of the paper or otherwise has the power and authority to make and execute this assignment.

Returned Rights: In return for these rights, ACES hereby grants to the above authors, and the employers for whom the work was performed, royalty-free permission to:

1. Retain all proprietary rights other than copyright, such as patent rights.
2. Reuse all or portions of the above paper in other works.
3. Reproduce, or have reproduced, the above paper for the author's personal use or for internal company use provided that (a) the source and ACES copyright are indicated, (b) the copies are not used in a way that implies ACES endorsement of a product or service of an employer, and (c) the copies per se are not offered for sale.
4. Make limited distribution of all or portions of the above paper prior to publication.
5. In the case of work performed under U.S. Government contract, ACES grants the U.S. Government royalty-free permission to reproduce all or portions of the above paper, and to authorize others to do so, for U.S. Government purposes only.

ACES Obligations: In exercising its rights under copyright, ACES will make all reasonable efforts to act in the interests of the authors and employers as well as in its own interest. In particular, ACES REQUIRES that:

1. The consent of the first-named author be sought as a condition in granting re-publication permission to others.
2. The consent of the undersigned employer be obtained as a condition in granting permission to others to reuse all or portions of the paper for promotion or marketing purposes.

In the event the above paper is not accepted and published by ACES or is withdrawn by the author(s) before acceptance by ACES, this agreement becomes null and void.

AUTHORIZED SIGNATURE — TITLE (IF NOT AUTHOR)

EMPLOYER FOR WHOM WORK WAS PERFORMED — DATE FORM SIGNED

Part B - U.S. GOVERNMENT EMPLOYEE CERTIFICATION

(NOTE: if your work was performed under Government contract but you are not a Government employee, sign transfer form above and see item 5 under Returned Rights).

This certifies that all authors of the above paper are employees of the U.S. Government and performed this work as part of their employment and that the paper is therefor not subject to U.S. copyright protection.

AUTHORIZED SIGNATURE — TITLE (IF NOT AUTHOR)

NAME OF GOVERNMENT ORGANIZATION — DATE FORM SIGNED

PART C - CROWN COPYRIGHT

(NOTE: ACES recognizes and will honor Crown Copyright as it does U.S. Copyright. It is understood that, in asserting Crown Copyright, ACES in no way diminishes its rights as publisher. Sign only if *ALL* authors are subject to Crown Copyright).

This certifies that all authors of the above Paper are subject to Crown Copyright. (Appropriate documentation and instructions regarding form of Crown Copyright notice may be attached).

AUTHORIZED SIGNATURE TITLE OF SIGNEE

NAME OF GOVERNMENT BRANCH DATE FORM SIGNED

Information to Authors

ACES POLICY

ACES distributes its technical publications throughout the world, and it may be necessary to translate and abstract its publications, and articles contained therein, for inclusion in various compendiums and similar publications, etc. When an article is submitted for publication by ACES, acceptance of the article implies that ACES has the rights to do all of the things it normally does with such an article.

In connection with its publishing activities, it is the policy of ACES to own the copyrights in its technical publications, and to the contributions contained therein, in order to protect the interests of ACES, its authors and their employers, and at the same time to facilitate the appropriate re-use of this material by others.

The new United States copyright law requires that the transfer of copyrights in each contribution from the author to ACES be confirmed in writing. It is therefore necessary that you execute either Part A-Copyright Transfer Form or Part B-U.S. Government Employee Certification or Part C-Crown Copyright on this sheet and return it to the Managing Editor (or person who supplied this sheet) as promptly as possible.

CLEARANCE OF PAPERS

ACES must of necessity assume that materials presented at its meetings or submitted to its publications is properly available for general dissemination to the audiences these activities are organized to serve. It is the responsibility of the authors, not ACES, to determine whether disclosure of their material requires the prior consent of other parties and if so, to obtain it. Furthermore, ACES must assume that, if an author uses within his/her article previously published and/or copyrighted material that permission has been obtained for such use and that any required credit lines, copyright notices, etc. are duly noted.

AUTHOR/COMPANY RIGHTS

If you are employed and you prepared your paper as a part of your job, the rights to your paper initially rest with your employer. In that case, when you sign the copyright form, we assume you are authorized to do so by your employer and that your employer has consented to all of the terms and conditions of this form. If not, it should be signed by someone so authorized.

NOTE RE RETURNED RIGHTS: Just as ACES now requires a signed copyright transfer form in order to do "business as usual", it is the intent of this form to return rights to the author and employer so that they too may do "business as usual". If further clarification is required, please contact: The Managing Editor, R. W. Adler, Naval Postgraduate School, Code EC/AB, Monterey, CA, 93943, USA (408)656-2352.

Please note that, although authors are permitted to re-use all or portions of their ACES copyrighted material in other works, this does not include granting third party requests for reprinting, republishing, or other types of re-use.

JOINT AUTHORSHIP

For jointly authored papers, only one signature is required, but we assume all authors have been advised and have consented to the terms of this form.

U.S. GOVERNMENT EMPLOYEES

Authors who are U.S. Government employees are not required to sign the Copyright Transfer Form (Part A), but any co-authors outside the Government are.

Part B of the form is to be used instead of Part A only if all authors are U.S. Government employees and prepared the paper as part of their job.

NOTE RE GOVERNMENT CONTRACT WORK: Authors whose work was performed under a U.S. Government contract but who are not Government employees are required so sign Part A-Copyright Transfer Form. However, item 5 of the form returns reproduction rights to the U. S. Government when required, even though ACES copyright policy is in effect with respect to the reuse of material by the general public.

APPLIED COMPUTATIONAL ELECTROMAGNETICS SOCIETY JOURNAL
http://aces.ee.olemiss.edu

INFORMATION FOR AUTHORS

PUBLICATION CRITERIA

Each paper is required to manifest some relation to applied computational electromagnetics. **Papers may address general issues in applied computational electromagnetics, or they may focus on specific applications, techniques, codes, or computational issues.** While the following list is not exhaustive, each paper will generally relate to at least one of these areas:

1. **Code validation.** This is done using internal checks or experimental, analytical or other computational data. Measured data of potential utility to code validation efforts will also be considered for publication.

2. **Code performance analysis.** This usually involves identification of numerical accuracy or other limitations, solution convergence, numerical and physical modeling error, and parameter tradeoffs. However, it is also permissible to address issues such as ease-of-use, set-up time, run time, special outputs, or other special features.

3. **Computational studies of basic physics.** This involves using a code, algorithm, or computational technique to simulate reality in such a way that better, or new physical insight or understanding, is achieved.

4. **New computational techniques** or new applications for existing computational techniques or codes.

5. **"Tricks of the trade"** in selecting and applying codes and techniques.

6. **New codes, algorithms, code enhancement, and code fixes.** This category is self-explanatory, but includes significant changes to existing codes, such as applicability extensions, algorithm optimization, problem correction, limitation removal, or other performance improvement. **Note: Code (or algorithm) capability descriptions are not acceptable, unless they contain sufficient technical material to justify consideration.**

7. **Code input/output issues.** This normally involves innovations in input (such as input geometry standardization, automatic mesh generation, or computer-aided design) or in output (whether it be tabular, graphical, statistical, Fourier-transformed, or otherwise signal-processed). Material dealing with input/output database management, output interpretation, or other input/output issues will also be considered for publication.

8. **Computer hardware issues.** This is the category for analysis of hardware capabilities and limitations of various types of electromagnetics computational requirements. Vector and parallel computational techniques and implementation are of particular interest.

Applications of interest include, but are not limited to, antennas (and their electromagnetic environments), networks, static fields, radar cross section, inverse scattering, shielding, radiation hazards, biological effects, biomedical applications, electromagnetic pulse (EMP), electromagnetic interference (EMI), electromagnetic compatibility (EMC), power transmission, charge transport, dielectric, magnetic and nonlinear materials, microwave components, MEMS, RFID, and MMIC technologies, remote sensing and geometrical and physical optics, radar and communications systems, sensors, fiber optics, plasmas, particle accelerators, generators and motors, electromagnetic wave propagation, non-destructive evaluation, eddy currents, and inverse scattering.

Techniques of interest include but not limited to frequency-domain and time-domain techniques, integral equation and differential equation techniques, diffraction theories, physical and geometrical optics, method of moments, finite differences and finite element techniques, transmission line method, modal expansions, perturbation methods, and hybrid methods.

Where possible and appropriate, authors are required to provide statements of quantitative accuracy for measured and/or computed data. This issue is discussed in "Accuracy & Publication: Requiring, quantitative accuracy statements to accompany data," by E. K. Miller, *ACES Newsletter,* Vol. 9, No. 3, pp. 23-29, 1994, ISBN 1056-9170.

SUBMITTAL PROCEDURE

All submissions should be uploaded to ACES server through ACES web site (http://aces.ee.olemiss.edu) by using the upload button, journal section. Only pdf files are accepted for submission. The file size should not be larger than 5MB, otherwise permission from the Editor-in-Chief should be obtained first. Automated acknowledgment of the electronic submission, after the upload process is successfully completed, will be sent to the corresponding author only. It is the responsibility of the corresponding author to keep the remaining authors, if applicable, informed. Email submission is not accepted and will not be processed.

PAPER FORMAT (INITIAL SUBMISSION)

The preferred format for initial submission manuscripts is 12 point Times Roman font, single line spacing and single column format, with 1 inch for top, bottom, left, and right margins. Manuscripts should be prepared for standard 8.5x11 inch paper.

EDITORIAL REVIEW

In order to ensure an appropriate level of quality control, papers are peer reviewed. They are reviewed both for

technical correctness and for adherence to the listed guidelines regarding information content and format.

PAPER FORMAT (FINAL SUBMISSION)

Only camera-ready electronic files are accepted for publication. The term **"camera-ready" means that the material is neat, legible, reproducible, and in accordance with the final version format listed below.**

The following requirements are in effect for the final version of an ACES Journal paper:

1. The paper title should not be placed on a separate page. The title, author(s), abstract, and (space permitting) beginning of the paper itself should all be on the first page. The title, author(s), and author affiliations should be centered (center-justified) on the first page. The title should be of font size 16 and bolded, the author names should be of font size 12 and bolded, and the author affiliation should be of font size 12 (regular font, neither italic nor bolded).

2. An abstract is required. The abstract should be a brief summary of the work described in the paper. It should state the computer codes, computational techniques, and applications discussed in the paper (as applicable) and should otherwise be usable by technical abstracting and indexing services. The word "Abstract" has to be placed at the left margin of the paper, and should be bolded and italic. It also should be followed by a hyphen (—) with the main text of the abstract starting on the same line.

3. All section titles have to be centered and all the title letters should be written in caps. The section titles need to be numbered using roman numbering (I. II. ….)

4. Either British English or American English spellings may be used, provided that each word is spelled consistently throughout the paper.

5. Internal consistency of references format should be maintained. As a guideline for authors, we recommend that references be given using numerical numbering in the body of the paper (with numerical listing of all references at the end of the paper). The first letter of the authors' first name should be listed followed by a period, which in turn, followed by the authors' complete last name. Use a coma (,) to separate between the authors' names. Titles of papers or articles should be in quotation marks (" "), followed by the title of journal, which should be in italic font. The journal volume (vol.), issue number (no.), page numbering (pp.), month and year of publication should come after the journal title in the sequence listed here.

6. Internal consistency shall also be maintained for other elements of style, such as equation numbering. As a guideline for authors who have no other preference, we suggest that equation numbers be placed in parentheses at the right column margin.

7. The intent and meaning of all text must be clear. For authors who are not masters of the English language, the ACES Editorial Staff will provide assistance with grammar (subject to clarity of intent and meaning). However, this may delay the scheduled publication date.

8. Unused space should be minimized. Sections and subsections should not normally begin on a new page.

ACES reserves the right to edit any uploaded material, however, this is not generally done. It is the author(s) responsibility to provide acceptable camera-ready pdf files. Incompatible or incomplete pdf files will not be processed for publication, and authors will be requested to re-upload a revised acceptable version.

COPYRIGHTS AND RELEASES

Each primary author must sign a copyright form and obtain a release from his/her organization vesting the copyright with ACES. Copyright forms are available at ACES, web site (http://aces.ee.olemiss.edu). To shorten the review process time, the executed copyright form should be forwarded to the Editor-in-Chief immediately after the completion of the upload (electronic submission) process. Both the author and his/her organization are allowed to use the copyrighted material freely for their own private purposes.

Permission is granted to quote short passages and reproduce figures and tables from and ACES Journal issue provided the source is cited. Copies of ACES Journal articles may be made in accordance with usage permitted by Sections 107 or 108 of the U.S. Copyright Law. This consent does not extend to other kinds of copying, such as for general distribution, for advertising or promotional purposes, for creating new collective works, or for resale. The reproduction of multiple copies and the use of articles or extracts for commercial purposes require the consent of the author and specific permission from ACES. Institutional members are allowed to copy any ACES Journal issue for their internal distribution only.

PUBLICATION CHARGES

All authors are allowed for 8 printed pages per paper without charge. Mandatory page charges of $75 a page apply to all pages in excess of 8 printed pages. Authors are entitled to one, free of charge, copy of the journal issue in which their paper was published. Additional reprints are available for a nominal fee by submitting a request to the managing editor or ACES Secretary.

Authors are subject to fill out a one page over-page charge form and submit it online along with the copyright form before publication of their manuscript.

ACES Journal is abstracted in INSPEC, in Engineering Index, DTIC, Science Citation Index Expanded, the Research Alert, and to Current Contents/Engineering, Computing & Technology.